

Broadening the Canonical Picture of EUV-Driven Photoevaporation of Accretion Disks

RIOUEI NAKATANI,^{1,2} NEAL J. TURNER,¹ AND SHINSUKE TAKASAO³

¹*NASA Jet Propulsion Laboratory, California Institute of Technology, 4800 Oak Grove Dr, Pasadena, CA 91109, USA*

²*RIKEN Cluster for Pioneering Research, 2-1 Hirosawa, Wako, Saitama 351-0198, Japan*

³*Department of Earth and Space Science, Graduate School of Science, Osaka University, Toyonaka, Osaka 560-0043, Japan*

ABSTRACT

Photoevaporation driven by hydrogen-ionizing radiation, also known as extreme-ultraviolet (EUV), profoundly shapes the lives of diverse astrophysical objects. Focusing here mainly on the dispersal of protoplanetary disks, we construct an analytical model accounting for the finite timescales of photoheating and photoionization. The model offers improved estimates for the ionization, temperature, and velocity structures versus distance from the central source, for a given EUV emission rate and spectral hardness. Compared to the classical picture of fully-ionized and isothermal winds with temperatures $\approx 10^4$ K and speeds $\approx 10 \text{ km s}^{-1}$, our model unveils broader hydrodynamical and thermochemical states of photoevaporative winds. In contrast to the classical picture, T Tauri stars with EUV luminosities around $10^{30} \text{ erg s}^{-1}$ have non-isothermal ionized winds at lower temperatures than the classical value if the spectrum is soft, with an average deposited energy per photoionization less than about 3.7 eV. Conversely, if the spectrum is hard, the winds tend to be atomic and isothermal at most radii in the disk. For lower EUV intensities, even with soft spectra, atomic winds can emerge beyond $\sim 10 \text{ au}$ through advection. We demonstrate that the analytical model's predictions are in general agreement with detailed radiation-hydrodynamics calculations. The model furthermore illustrates how the energy efficiency of photoevaporation varies with the intensity and spectral hardness of the EUV illumination, as well as addressing discrepancies in the literature around the effectiveness of X-ray photoevaporation. These findings highlight the importance of considering the finite timescales of photoheating and photoionization, both in modeling and in interpreting observational data.

1. INTRODUCTION

Hydrogen-ionizing radiation, also called extreme-ultraviolet (EUV; $13.6 \lesssim h\nu \lesssim 100 \text{ eV}$), is widely recognized for its crucial role in various astrophysical contexts, including planetary atmospheres (e.g., Murray-Clay et al. 2009; Owen & Alvarez 2016), protoplanetary disks (e.g., Hollenbach et al. 1994), molecular clouds (e.g., Kahn 1954; Bertoldi 1989; Bertoldi & McKee 1990; Nakatani & Yoshida 2019), and galactic minihalos (e.g., Shapiro et al. 2004; Iliev et al. 2005; Nakatani et al. 2020). EUV radiation induces not only photoionization of hydrogen-dominated gas but also associated heating, driving photoevaporative winds that can disperse structures within a finite time. Essentially, this means that ionizing radiation has exerted a significant influence on the evolution and formation processes of planets, stars, and galaxies since the dawn of the cosmic reionization epoch.

Classically, it is commonly assumed that EUV-heated gas is fully ionized and exhibits temperatures of $\approx 10^4$ K, regu-

lated by a balance between heating and cooling processes, resulting in supersonic photoevaporative winds. However, this scenario is valid only when the timescales of heating and ionization are much shorter than the dynamical timescales, and thus it could vary widely depending on factors such as the magnitude of gravity exerted by the object involved, its configuration, and EUV radiation environments, e.g., EUV flux and spectrum. Consequently, a diverse range of modes is possible for EUV-driven photoevaporation. Given that EUV photoevaporation occurs in diverse environments, there is a pressing need for a systematic and comprehensive understanding of this process. However, such an understanding is not yet fully developed.

In the context of protoplanetary disk dispersal, which constitutes the primary focus of this study, EUV-driven photoevaporation is considered as one of the mechanisms responsible for the final-stage dispersal of the gas disks (Alexander et al. 2014; Pascucci et al. 2023), consequently determining the time limit available for (gas giant) planet formation. Therefore, a comprehensive understanding of EUV photoevaporation is of great importance for advancing the planet formation theory.

The current canonical picture of EUV-driven photoevaporation in protoplanetary disks can be outlined as follows: EUV energy is injected into the H I layer of the disk just ahead of the ionization front, where the EUV optical depth τ_{EUV} is approximately unity (Figure 1). Subsequently, the gas undergoes immediate photoionization to form ionized thermal winds emanating from the disk surface. These winds typically attain around $\approx 10^4$ K, a value determined by the thermal balance between photoionization heating and various radiative cooling within the H II region, including metal forbidden lines, Ly α emissions, and radiative recombination. The resulting sound speed corresponds to $\approx 10 \text{ km s}^{-1}$, providing a typical speed of the transonic flows.

This conceptual framework was initially proposed in the context of disk photoevaporation around massive stars (Hollenbach et al. 1993, 1994) and has been applied to the EUV photoevaporation of protoplanetary disks in general, including around young low-mass stars (e.g., Shu et al. 1993). However, the validity of this generalization is not straightforward, given that the typical EUV emission rate Φ_{EUV} of young low-mass stars ($\lesssim 10^{42} \text{ s}^{-1}$; e.g., Alexander et al. 2005; Pascucci et al. 2014) is likely several orders of magnitude less than that of massive stars ($\Phi_{\text{EUV}} \approx 10^{48} - 10^{49} \text{ s}^{-1}$; e.g., Maeder & Meynet 1987; Hollenbach et al. 1994). Qualitatively, the lower Φ_{EUV} implies a longer time required for heating and ionizing the gas. Consequently, the canonical picture, which implicitly assumes an infinitely short photoheating and photoionization timescale, is expected to be applicable only in cases where Φ_{EUV} is sufficiently high (see also discussions in Appendix A of Hollenbach et al. (1994)).

Moreover, the EUV spectrum of massive stars notably includes a significant contribution from photospheric emission with an effective temperature of $\approx 30000 - 50000 \text{ K}$. This spectral attribute is softer in comparison to the EUV spectrum of young low-mass stars, where metal line emissions from $\sim 10^5 \text{ K}$ plasma are predominant (Shoda & Takasao 2021). Since the absorption cross-section of the gas for EUV is generally lower for higher photon energies, the difference in spectrum hardness can profoundly influence even the qualitative chemo-dynamical aspects of EUV-driven photoevaporation.

These considerations regarding application limits raise pertinent questions: Under what parameter space (EUV emission rate, spectral hardness, and distance from the source) does the canonical picture hold true? And what chemical and hydrodynamical states might an EUV-driven wind exhibit in the other parameter spaces? How might these insights be relevant to photoevaporation induced by alternative photoheating processes, such as far-ultraviolet (FUV) grain photoelectric heating and X-ray photoionization heating? To tackle these questions, we discuss how the picture of EUV photoevaporation evolves contingent upon the stel-

lar mass M_* , EUV emission rate Φ_{EUV} , and EUV spectrum while incorporating the finite timescales of photoheating and photoionization. We develop an analytical model based on phenomenology that adequately treats these timescales as well as the dynamical timescale of winds and recombination timescale. Our phenomenological model draws inspiration from the analytical model for the Compton-heated winds of active galactic nuclei presented in Begelman et al. (1983) (hereafter BMS83).

This paper is organized as follows. We begin by outlining the basic setup and introducing fundamental quantities for our model in §2. Following this, in §3, we provide a qualitative overview of the key findings from our model, reserving detailed quantitative derivations for §4. These sections delve into discussing the typical temperature, wind speed, and ionized state EUV-driven winds would have across various regions of the parameter space. In §5, we compare model predictions with hydrodynamics simulations incorporating self-consistent radiative transfer and nonequilibrium thermochemistry to assess the predictability. To demonstrate the practical utility of the model in understanding the physical properties of photoevaporating disks, we explore the radial extension of the H II region in §6 and analyze the energy efficiency of EUV heating in driving winds in §7. In §8, we extend the application of our model to photoevaporation driven by far-ultraviolet (FUV) and X-ray radiation. Based on this application, we address a possible cause for a long-standing issue in the field — the divergent conclusions regarding the effectiveness of X-ray photoevaporation. Additionally, caveats and model limitations are presented in this section. Finally, we provide a summary of our major findings and outline potential avenues for future prospects in §9.

2. FUNDAMENTAL QUANTITIES

The purpose of this study is to construct an updated picture of EUV-driven thermal winds. To that end, this section focuses on introducing the fundamental setup of the model and the key quantities for the energetics and thermochemical structures of the system, such as the gravitational timescale and the rates of photoheating and photoionization. A list of the symbols used in our model is available in Appendix A.

The basic setup of our model is schematically depicted in Figure 1: a geometrically thin disk predominantly composed of hydrogen is irradiated by the central EUV source. Hydrogen exists in atomic form in the upper layers of the disk due to the photodissociation of molecular hydrogen, which is the dominant species in the deeper layers. The energy of EUV photons is deposited to the gas at the atomic layer by heating associated with photoionization, $\text{H} + \text{EUV} \longrightarrow \text{H}^+ + \text{e}^-$, and the gas can escape from the gravitational binding of the central object if it has reached a sufficiently high temperature. This escaping gas gives rise to steady thermal winds emanat-

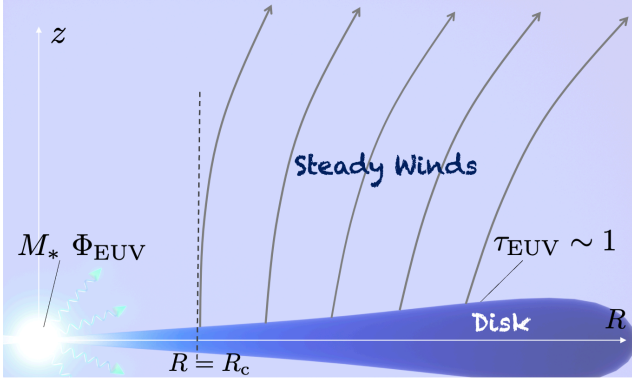


Figure 1. Schematic picture of a disk under EUV-driven photoevaporation. The radiation source with a mass of M_* and an EUV emission rate of Φ_{EUV} is illuminating the disk. The EUV photon hits the disk surface, where the optical depth to EUV is approximately unity, and photoionizes atomic hydrogen there, depositing excessive energy remaining after photoionization to the gas. As a result, photoevaporative winds arise from the disk surface. Vigorous winds are possible only beyond the critical radius R_c owing to weak gravity at a distance. In a classical picture, the winds are ionized and have an equilibrium temperature of $\approx 10^4$ K. The corresponding isothermal sound speed is $c_s \approx 10 \text{ km s}^{-1}$, which sets a typical flow speed of the winds due to the thermally-driven nature of photoevaporation.

ing from the so-called base, corresponding to the optically thick surface of the disk where $\tau_{\text{EUV}} \sim 1$.

2.1. Critical Radius

The winds can have a temperature of $\approx 10^4$ K (thermal equilibrium temperature) at most because cooling due to forbidden lines and Ly α emission quickly becomes effective as the temperature approaches the equilibrium value. The corresponding sound speed is $c_{\text{eq}} \approx 10 \text{ km s}^{-1}$, and this sets the order of a maximum achievable speed for EUV-driven winds.

We can define a threshold radius below which EUV-heated gas cannot escape from the gravitational binding even when it achieves the maximum flow speed c_{eq} . Hollenbach et al. (1994) introduce such a threshold radius (termed “gravitational radius”) as

$$R_g \equiv \frac{GM_*}{c_{\text{eq}}^2}.$$

through dimensional analysis comparing the thermal energy and gravitational potential energy. The gravitational radius exactly corresponds to the Compton radius R_{IC} in BMS83. BMS83 predicted that the actual threshold radius separating the wind-excited and wind-inhibited regimes might be present at the cylindrical distance from the source of $R \approx 0.1\text{--}1R_{\text{IC}}$ instead of $R = R_{\text{IC}}$. This is directly examined by hydrodynamics simulations in Woods et al. (1996), and they found the actual threshold radius to be $\approx 0.2R_{\text{IC}}$.

Liffman (2003) suggests that the threshold radius of $0.2R_{\text{IC}}$ corresponds to the radius at which the sum of photoheated

gas’s enthalpy and mechanical energy equals zero. Although the physical origin of the threshold radius is still worth exploring, in this study, we follow Liffman (2003) to define the “critical radius” as

$$R_c \equiv \frac{R_g}{2c_p}, \quad (1)$$

where c_p is a normalized specific heat at constant pressure

$$c_p \equiv \frac{\gamma}{\gamma - 1}$$

with γ being the specific heat ratio of the gas. Eq.(1) is a modified version of R_g , including correcting factors from enthalpy and centrifugal force due to gas’s angular momentum.

We define the gravitational velocity v_g as

$$v_g \equiv \sqrt{\frac{GM_*}{2c_p R}} = c_{\text{eq}} x^{-1/2}, \quad (2)$$

so that $c_{\text{eq}} = v_g$ at $R = R_c$. Here, x is a normalized distance

$$x \equiv \frac{R}{R_c}.$$

The corresponding gravitational timescale is

$$t_g \equiv \frac{R}{v_g} = \sqrt{\frac{2c_p R^3}{GM_*}}, \quad (3)$$

The normalized radius x corresponds to the normalized radius “ ζ ” in BMS83 except for the factor of $1/2c_p$ and the equilibrium temperature. We adopt denoting “ x ” for the normalized distance to highlight these differences and to avoid confusion with the ionization parameter, which is often denoted by ξ .

In this paper, we focus on the region where vigorous winds possibly form, and thus we only consider the region with $x \geq 1$, which is a necessary condition for EUV-heated gas to escape freely without being inhibited by gravity. We leave modeling the inner $x < 1$ region for future studies, since its nearly hydrostatic structure requires a different approach from the one presented in this study, as discussed in §8.4.

2.2. EUV Heating Rate

We calculate the frequency-dependent (specific) photon number flux from the point radiation source with radial ray tracing,

$$F_\nu(r, N_{\text{HI}}) = \frac{\Phi_\nu}{4\pi r^2} e^{-\sigma_\nu N_{\text{HI}}},$$

where ν is EUV frequency, Φ_ν is the specific EUV emission rate of the radiation source, r is the spherical distance from the source, σ_ν is the absorption cross-section of atomic hydrogen for EUV, and N_{HI} is the radial column density of atomic hydrogen along an EUV ray defined as

$$N_{\text{HI}} \equiv \int dr y_{\text{HI}} n_{\text{H}}$$

with y_{HI} and n_{H} being atomic hydrogen abundance and hydrogen nucleus number density, respectively. The atomic hydrogen number density is computed by $n_{\text{HI}} = y_{\text{HI}} n_{\text{H}}$. Energetic EUV photons can also be absorbed by He I and He II in general, but we ignore their contributions. This simplification has a minimal impact on the results of our order-of-magnitude phenomenological discussions in this study. We will delve into the effect of this simplification in more detail in §8.4.

The expression of F_{ν} implicitly assumes the direct EUV component dominating over the diffuse component. This assumption is based on the findings of Tanaka et al. (2013), where the authors performed full 2D radiative transfer calculations and observed that the direct EUV dominates over the diffuse EUV. This is in contrast to the classical findings of Hollenbach et al. (1994), where they employed the 1+1D radiative transfer and concluded that the inner ionized atmosphere completely cuts off the direct EUV within the gravitational radius. This discrepancy likely results from the difference in the treatment of the diffuse component transfer. Similarly to Tanaka et al. (2013), the direct EUV has been observed to reach the outer radii in more recent self-consistent radiation hydrodynamics simulations (Nakatani et al. 2018a,b; Komaki et al. 2021; Nakatani & Takasao 2022), even when the critical radius is well resolved. A nearly hydrostatic, ionized atmosphere is formed at inner radii, agreeing with the prediction of the previous hydrostatic models, but it does not terminate the radial EUV rays within the gravitational radius. These updated results justify our assumption on F_{ν} above.

As for photoheating, the excess energy of EUV photons over the ionization potential energy ($h\nu_1 \approx 13.6\text{eV}$) is responsible for EUV heating, and thus the specific heating rate is

$$\begin{aligned} \Gamma_{\text{EUV}} &\equiv \frac{y_{\text{HI}}}{m} \int_{\nu_1}^{\nu_{\text{max}}} \sigma_{\nu} (h\nu - h\nu_1) \frac{\Phi_{\nu}}{4\pi r^2} e^{-\sigma_{\nu} N_{\text{HI}}} d\nu \\ &= \frac{y_{\text{HI}}}{m} F_0 \delta \langle \sigma \rangle \langle \Delta E \rangle_i \end{aligned} \quad (4)$$

where m is the total gas mass per hydrogen nucleus, which can include the mass of other minor elemental species, like Helium, and is related to the gas density ρ through $m \equiv \rho/n_{\text{H}}$; ν_{max} is the upper limit of the EUV frequency, typically set to $\sim 100\text{eV}$; and F_0 is the unattenuated total EUV number flux at the spherical distance r ,

$$F_0 \equiv \int_{\nu_1}^{\nu_{\text{max}}} d\nu F_{\nu}(r, 0) = \frac{\Phi_{\text{EUV}}}{4\pi r^2}.$$

Here, Φ_{EUV} is the EUV emission rate of the radiation source. The dimensionless quantity δ is the ratio of the attenuated flux to the unattenuated flux F_0 at N_{HI} ,

$$\delta(N_{\text{HI}}) \equiv \frac{\int d\nu F_{\nu}(r, N_{\text{HI}})}{F_0} = \frac{\int d\nu \Phi_{\nu} \exp(-\sigma_{\nu} N_{\text{HI}})}{\Phi_{\text{EUV}}}.$$

This parameter describes the fraction of the EUV photons remaining at N_{HI} without being attenuated. The average cross-section of the remained EUV, $\langle \sigma \rangle$, is defined by

$$\langle \sigma \rangle(N_{\text{HI}}) \equiv \frac{\int d\nu \sigma_{\nu} F_{\nu}(r, N_{\text{HI}})}{\int d\nu F_{\nu}(r, N_{\text{HI}})},$$

and $\langle \Delta E \rangle_i$ is an average deposited energy per ionization at N_{HI}

$$\langle \Delta E \rangle_i(N_{\text{HI}}) \equiv \frac{\int d\nu \sigma_{\nu} (h\nu - h\nu_1) F_{\nu}(r, N_{\text{HI}})}{\int d\nu \sigma_{\nu} F_{\nu}(r, N_{\text{HI}})}.$$

All of δ , $\langle \sigma \rangle$, and $\langle \Delta E \rangle_i$ are dependent only on N_{HI} and a priori calculable, once Φ_{ν} is given. The former two are monotonically decreasing functions because the remaining EUV photons decrease as they go through the gas, and the average energy of the remaining photons increases to have a smaller cross-section on average. On the other hand, $\langle \Delta E \rangle_i$ is a monotonically increasing function since the average energy of remaining EUVs increases as they go through the gas. The product $\delta \langle \sigma \rangle \langle \Delta E \rangle_i$ is a monotonically decreasing function with respect to N_{HI} , which simply indicates that the less attenuated, the more energy is available for heating.

For convenience, we rewrite the product $\delta \langle \sigma \rangle \langle \Delta E \rangle_i$ in the dimensionless form of

$$\begin{aligned} \chi_e &\equiv \delta \left(\frac{\langle \sigma \rangle}{\bar{\sigma}_0} \right) \left(\frac{\langle \Delta E \rangle_i}{\bar{E}_0} \right) \\ &= \int d\nu \frac{\Phi_{\nu}}{\Phi_{\text{EUV}}} \frac{\sigma_{\nu}}{\bar{\sigma}_0} \frac{h\nu - h\nu_1}{\bar{E}_0} e^{-\sigma_{\nu} N_{\text{HI}}}. \end{aligned}$$

where

$$\begin{aligned} \bar{\sigma}_0 &\equiv \langle \sigma \rangle|_{N_{\text{HI}}=0} = \Phi_{\text{EUV}}^{-1} \int d\nu \sigma_{\nu} \Phi_{\nu} \\ \bar{E}_0 &\equiv \langle \Delta E \rangle_i|_{N_{\text{HI}}=0} \\ &= \left(\int d\nu \sigma_{\nu} \Phi_{\nu} \right)^{-1} \int d\nu \sigma_{\nu} \Phi_{\nu} (h\nu - h\nu_1) \end{aligned}$$

With these notations, Eq.(4) can be expressed in a simpler form

$$\Gamma_{\text{EUV}} = \frac{y_{\text{HI}}}{m} \frac{\Phi_{\text{EUV}}}{4\pi r^2} \bar{\sigma}_0 \bar{E}_0 \chi_e. \quad (5)$$

The attenuation factor χ_e depends only on N_{H} and is a monotonically decreasing function ranging in $0 < \chi_e \leq 1$; the upper and lower limits are achieved when $N_{\text{HI}} = 0$ and $N_{\text{HI}} \rightarrow \infty$, respectively.

In this paper, we perform our analysis under the idealization that a large portion of the wind region is optically thin ($\chi_e \sim 1$), following the approach of BMS83. While this idealization has its limitations and somewhat restricts the applicability of our model, it allows us to streamline our analysis. Importantly, despite this limitation, constructing a model based on this simplification is a crucial initial step towards developing a more comprehensive model available

for a broader range of spectra. Furthermore, the insights obtained from our simplified model lay the groundwork for addressing more general cases and prove valuable in systematically interpreting the outcomes of such broader contexts. The idealization would serve as a reasonable zeroth-order approximation in cases where spectra have minimal dispersion in photon energy, so that most photons are intensively absorbed at a certain column density. For instance, this includes relatively soft spectra, where most photons have energies close to the Lyman limit, or harder spectra with delta-function-like shapes. (See §8.4 for the potential impacts of this adopted approximation.)

2.3. Photoionization and Recombination Timescales

The EUV-driven winds undergo photoionization, $\text{H} + \text{EUV} \longrightarrow \text{H}^+ + \text{e}^-$, and radiative recombination, $\text{H}^+ + \text{e}^- \longrightarrow \text{H} + \text{photon}$, after launched. The photoionization rate coefficient is the number of photons absorbed per unit time per hydrogen atom

$$k_{\text{ioni}} \equiv \int d\nu \sigma_\nu \frac{\Phi_\nu}{4\pi r^2} e^{-\sigma_\nu N_{\text{H}}} = \frac{\Phi_{\text{EUV}}}{4\pi r^2} \bar{\sigma}_0 \chi_i, \quad (6)$$

where $\chi_i \equiv \delta\langle\sigma\rangle/\bar{\sigma}_0$ is another N_{H} -dependent, a priori calculable EUV attenuation factor, and $0 < \chi_i \leq 1$. Again, similarly to χ_e , we use the assumption of $\chi_i \sim 1$ in this study, as mentioned below Eq.(5).

The photoionization timescale is the inverse of the photochemical reaction rate coefficient

$$t_{\text{ioni}} \equiv k_{\text{ioni}}^{-1} = \left(\frac{\Phi_{\text{EUV}}}{4\pi r^2} \bar{\sigma}_0 \right)^{-1}. \quad (7)$$

This quantity sets the average timescale on which a single hydrogen atom takes to be photoionized.

Next, we introduce the recombination timescale

$$t_{\text{rec}} \equiv (n_{\text{H}} \alpha)^{-1}$$

with α being the case B recombination coefficient. We give α in the form of

$$\alpha = \alpha_{\text{eq}} \left(\frac{c_s}{c_{\text{eq}}} \right)^{-2\beta}, \quad (8)$$

where α_{eq} is the case B recombination coefficient at $T \approx 10^4 \text{ K}$ and, typically, $\alpha_{\text{eq}} \sim 2 \times 10^{-13} \text{ cm}^3 \text{ s}^{-1}$; β is the power-law exponent for temperature and typically $0.5 \lesssim \beta \lesssim 0.75$ (cf. the UMIST database, McElroy et al. 2013).

In contrast to t_{ioni} , the recombination timescale is dependent on the gas density (and temperature) of the winds. Hollenbach et al. (1994) and Tanaka et al. (2013) characterize n_{H} at the base of EUV-driven winds by Strömgren condition, i.e., ionization-recombination equilibrium along line of

sights from the radiation source, as

$$\begin{aligned} n_{\text{base}} &= C \sqrt{\frac{3\Phi_{\text{EUV}}}{4\pi r^3 \alpha}} \\ &\approx 7.6 \times 10^5 \text{ cm}^{-3} \left(\frac{\Phi_{\text{EUV}}}{10^{40} \text{ s}^{-1}} \right)^{1/2} \left(\frac{r}{1 \text{ au}} \right)^{-3/2} \\ &\quad \times \left(\frac{\alpha}{2 \times 10^{-13} \text{ cm}^3 \text{ s}^{-1}} \right)^{-1/2} \left(\frac{C}{0.4} \right) \end{aligned} \quad (9)$$

Here, C is an artificial dimensionless factor to match the numerical results, originating from the geometry of the ionized region (typically, $0.1 \lesssim C \lesssim 0.4$; Hollenbach et al. 1994; Font et al. 2004; Tanaka et al. 2013).

Substituting this density into t_{rec} , the recombination timescale is expressed as

$$t_{\text{rec}} = \left(\frac{3C^2 \Phi_{\text{EUV}} \alpha_{\text{eq}}}{4\pi r^3} \right)^{-1/2} \left(\frac{c_s}{c_{\text{eq}}} \right)^\beta. \quad (10)$$

Strictly, this equation specifically provides the recombination timescale near the launch point in the case where recombination dominates the opacity for EUV in the wind region. Typically, as the evaporating gas flows away from the disk, its density decreases due to expansion, leading to a longer recombination timescale and consequently a higher ionization degree. Moreover, the base density could vary depending on the EUV spectral hardness in practice. Eqs.(9) and (10) do not account for such variations and are probably applicable only under conditions where recombination dominates the opacity over absorption by advected atomic hydrogen. This condition typically holds for softer spectra. Regardless of these uncertainties, in this study, we uniformly use Eq.(10) as a rough estimate for the recombination timescale to the height of $\sim R$ and for any spectra. We discuss the potential impacts of this simplification in §8.4.

The ratio of the ionization timescale to the recombination timescale is a key metric for characterizing the ionization degree of the gas. By using Eqs.(7) and (10), this can be expressed as

$$\frac{t_{\text{ioni}}}{t_{\text{rec}}} = q^{1/2} \left(\frac{t_{\text{ioni}}}{R/c_{\text{eq}}} \right)^{1/2} \left(\frac{c_s}{c_{\text{eq}}} \right)^{-\beta} \left(= \frac{3C^2 \chi_i^{-1}}{n_{\text{base}} \bar{\sigma}_0 R} \right). \quad (11)$$

with q being a dimensionless constant

$$q \equiv \frac{3C^2 \alpha_{\text{eq}}}{c_{\text{eq}} \bar{\sigma}_0}. \quad (12)$$

This constant is uniquely set once an EUV spectrum is given; a harder spectrum results in a smaller average cross-section $\bar{\sigma}_0$, leading to a larger q . We will explain this spectral hardness parameter is one of the parameters used for the classification of EUV photoevaporation in §3.4.

To interpret the physical meaning of the q parameter in a more direct manner, it is convenient to evaluate the ratio of t_{ioni} to t_{rec} with $c_s = c_{\text{eq}}$:

$$\frac{t_{\text{ioni}}}{t_{\text{rec,eq}}} = q^{1/2} \left(\frac{t_{\text{ioni}}}{R/c_{\text{eq}}} \right)^{1/2},$$

where $t_{\text{rec,eq}} \equiv t_{\text{rec}}(c_s = c_{\text{eq}})$. The above equation gives

$$q = \left(\frac{R/c_{\text{eq}}}{t_{\text{rec,eq}}} \right) \left(\frac{t_{\text{ioni}}}{t_{\text{rec,eq}}} \right) = \left(\alpha_{\text{eq}} n_{\text{base}} \frac{R}{c_{\text{eq}}} \right) (k_{\text{ioni}} t_{\text{rec,eq}})^{-1}.$$

Hence, q is the number of recombination while the gas traveling to the height of R , with respect to the number of photoionization during one recombination event. Thus, q assesses the efficiency of reproducing atomic hydrogen through recombination against photoionization.

An increase in spectral hardness leads to a decrease in $\bar{\sigma}_0$, thereby relatively weakening photoionization compared to recombination by extending the photoionization timescale. This effectively enhances the relative importance of atomic hydrogen reproduction, meaning a large q .

3. CLASSIFICATION OF PHOTOEVAPORATING DISKS

In this section, we summarize a qualitative overview of the major findings derived from our phenomenological model. Our model is designed to characterize the typical temperature, namely the isothermal sound speed c_s , typical flow speed, and the ionization state of winds launched at a distance R under the influence of a radiation source emitting EUV with a rate of Φ_{EUV} . Since photoevaporative winds are thermally driven, the sound speed can also dictate the typical flow velocity. We identify three distinct classes in EUV photoevaporation, each contingent upon the hardness of the EUV spectrum.

Here, we provide the general pictures for each class, outlining the key parameters employed in their classification. We begin by discussing the possible ionization states of winds, which form the foundational basis of our model (§3.1). Subsequently, we delve into the heating timescale, which stands as the most important quantity to define the hydrodynamical states of winds (§3.2). Expanding on this foundation, the typical temperature and velocity of winds are estimated (§3.3), followed by the introduction of the EUV photoevaporation classes (§3.4). Finally, we illustrate the distinctive characteristics of the three classes (one each in §3.5–3.7). For detailed derivations of the quantities, parameter spaces, and classes reviewed in this section, the readers are referred to §4.

As mentioned in Sections 2.2 and 2.3 and similarly to the approach of BMS83, this study focuses specifically on the cases where a significant portion of the wind region is optically thin (i.e., $\chi_e \sim 1$ and $\chi_i \sim 1$ in Eqs.(5) and (6)). While

this simplifying approach does place limitations on the applicability, the constructed model provides a foundation and valuable insights for addressing more general cases. We discuss the potential impacts of this simplification in §8.4. Throughout this section, we adopt a specific value of $\beta = 0.75$ for the power-law index of the recombination rate coefficient (Eq.(8)) for simplicity.

3.1. Wind Types: Ionized VS Atomic

To discuss the ionization state of winds, we introduce the coordinate s along a streamline of steady winds, with $s = 0$ denoting the launch point (Figure 2). Initial energy injection takes place in the H I layer near the launch point. If photoionization proceeds sufficiently rapidly, the launched gas can undergo complete photoionization, transitioning into the ionized wind before reaching a height of $s \sim R$ above the disk. In essence, for an ionized wind to form, the photoionization timescale must be shorter than both the recombination timescale and wind crossing timescale.

This consideration leads us to categorize EUV-driven thermal winds into two types:

(I) *Winds characterized by atomic composition*, i.e., chemically neutral, within $s \leq R$ (left panel in Figure 2). This can arise when either the photoionization timescale is longer than the recombination timescale or the crossing timescale of the launched gas

$$t_{\text{ioni}} > \min \left(t_{\text{rec}}, \frac{R}{\mathcal{M}c_s} \right), \quad (13)$$

where \mathcal{M} is a representative Mach number in the wind within $s \leq R$. Qualitatively, this wind type is expected when Φ_{EUV} is relatively low yet capable of gradually depositing energy into the gas to drive winds or when the spectrum is relatively hard, so y_{HI} in the ionization-recombination equilibrium is nearly unity.

(II) *Winds transitioning into an ionized state at a certain height*, $s = s_1 (< R)$, and being atomic below that (right panel in Figure 2). This scenario aligns with the canonical picture of EUV photoevaporation. It occurs when Φ_{EUV} is sufficiently high, causing the ionization timescale (t_{ioni}) to be shorter than both the recombination and crossing timescales.

$$t_{\text{ioni}} < \min \left(t_{\text{rec}}, \frac{R}{\mathcal{M}c_s} \right). \quad (14)$$

Henceforth, we refer to the first and second types as Type I and Type II, respectively. While the picture of Type II is more conventional for EUV photoevaporation, the numbering convention is chosen to facilitate immediate association with the chemical states of the winds. Specifically, Type I corresponds to H I winds, and Type II corresponds to H II winds.

3.2. Characteristic Sound Speed and Heating Timescale

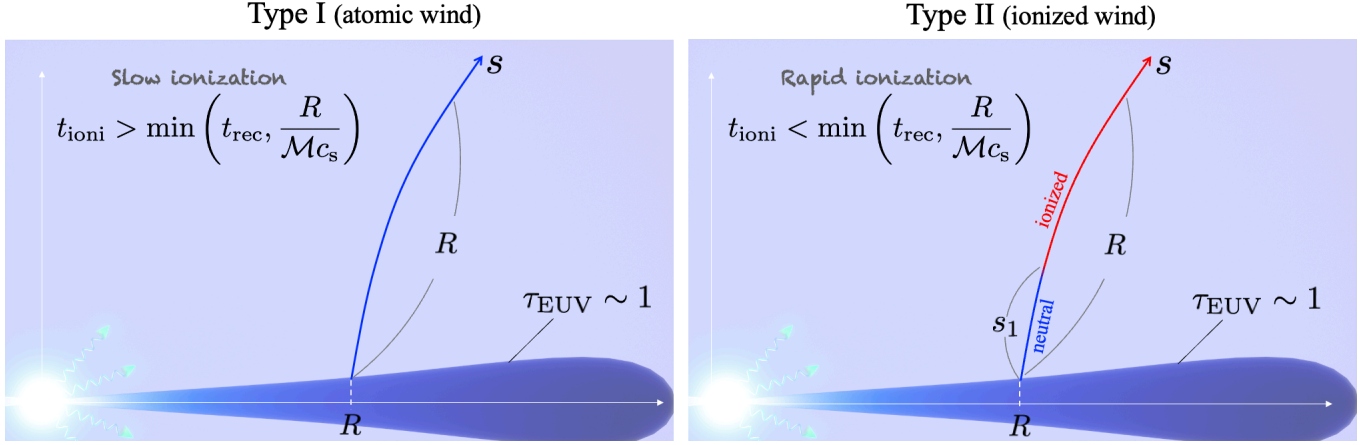


Figure 2. Two possible configurations of EUV-driven winds. (left) The wind is essentially atomic while traveling to the height of $\sim R$. This would occur when Φ_{EUV} is small so that the ionization timescale is longer than either the wind crossing timescale or recombination timescale within the wind. We term this type of atomic wind as Type I. The variable s here is coordinates along streamlines. (right) In contrast to Type I, the photoionization timescale is shorter than the recombination timescale and wind crossing timescale. In this case, the energy-injected gas can be ionized at some point s_1 between the launching point and the height $\sim R$. Hydrogen atoms within the launched gas can survive for a photoionization timescale t_{ioni} on average, and thus the transition height can be given as $s_1 \sim \mathcal{M}c_s t_{\text{ioni}}$. We refer to this ionized flow as Type II. Note that the neutral region ($s \lesssim s_1$) can be geometrically very thin, but here, we draw it vertically extended for visualization purposes.

The magnitude of photoheating determines the typical temperature and speed of winds. Photoheating can be gauged by the attainable sound speed as a result of heating. In general, the wind's sound speed does not necessarily reach the equilibrium value c_{eq} when the heating rate is small due to a finite photoheating rate.

Following BMS83, we evaluate the attainable sound speed by the characteristic sound speed c_{ch} defined as

$$c_p c_{\text{ch}}^2 = \bar{\Gamma}_{\text{EUV}} \frac{R}{c_{\text{ch}}} \quad (15)$$

where $\bar{\Gamma}_{\text{EUV}}$ is a time-average specific heating rate

$$\bar{\Gamma}_{\text{EUV}} \equiv \left(\frac{R}{c_{\text{ch}}} \right)^{-1} \int \Gamma_{\text{EUV}} \frac{ds}{c_{\text{ch}}}.$$

The integral is taken from the base to the height $s = R$, treating c_{ch} as a constant while taking into account the variability of y_{HI} in Γ_{EUV} (cf. Eq.(4)); thus, the form of c_{ch} differs by the wind types as we will see below. The RHS of Eq.(15) indicates the total specific energy deposited until the gas reaches the height of R .¹

The characteristic sound speed corresponds to the isothermal sound speed that the launched gas would attain if all the specific energy integrated during its ascent to the height $\sim R$ were converted into the specific enthalpy. It is important to

note that the characteristic sound speed serves as a metric of the heating magnitude and does not necessarily reflect the actual sound speed of the gas c_s , as cooling and gravity play roles in determining the hydrodynamics of winds. We will elaborate on this aspect later in §3.3.

In BMS83, c_p does not appear on the left-hand side (LHS) of Eq.(15). This coefficient would not be uniquely determined, and one could potentially use another constant as long as it is $\mathcal{O}(c_p)$; this introduces some arbitrariness into the model. Nevertheless, such an arbitrariness does not significantly alter the results and conclusions presented in this paper.

Correspondingly to Eq.(15), the heating timescale is defined as

$$t_h \equiv \frac{c_p c_{\text{ch}}^2}{\bar{\Gamma}_{\text{EUV}}} = \frac{R}{c_{\text{ch}}}.$$

If the heating timescale is longer than the crossing timescale of an isothermal wind, R/c_{eq} , the wind does not have long enough time to be heated to the equilibrium temperature by reaching $\sim R$, within which the bulk of energy deposition occurs. Moreover, if t_h is further longer than the gravitational timescale, the wind is significantly inhibited by gravity.

Since the specific heating rate Γ_{EUV} (Eq.(4)) depends on the H I abundance y_{HI} , the expression for c_{ch} varies depending on whether the wind encompasses an ionized region or not. For atomic winds (Type I; left panel in Figure 2), the hydrogen abundance can be approximated to $y_{\text{HI}} \approx 1$ in Γ_{EUV} of Eq.(15), and c_{ch} reduces to

$$c_{\text{ch}} = c_{\text{ch}}^{\text{I}} \equiv \left(\frac{\Gamma_{\text{EUV}} R}{c_p} \right)^{1/3} = c_{\text{eq}} \left(\frac{\varphi}{x} \right)^{1/3}, \quad (16)$$

¹ Defining c_{ch} using the volume-integrated photoheating rate divided by the area of a flow bundle on the right-hand side of Eq.(15) can give a more accurate estimation of wind's sound speed. Nevertheless, using the path integral instead, as in Eq.(15), suffices for the order-of-magnitude estimate in the present study.

where φ is the dimensionless EUV emission rate, which is Φ_{EUV} normalized by the critical EUV emission rate,

$$\Phi_c \equiv \frac{4\pi m c_{\text{eq}} G M_*}{2\bar{\sigma}_0 \bar{E}_0}, \quad (17)$$

Again, x is the distance from the source in units of the critical radius R_c (Eq.(1)):

$$x \equiv \frac{R}{R_c}.$$

In this study, we focus on the region with $x > 1$, where strong winds can be anticipated. We defer investigation of the inner region with $x < 1$ for future studies (see §8.4).

Note that the critical EUV emission rate is defined in such a way that it depends solely on spatially invariant constants determined by the properties of the radiation source and the disk gas. It is physically interpreted as the EUV emission rate when the power required to evaporate the gas against the effective gravity at the equilibrium sound speed, $m c_{\text{eq}} G M_* / 2R^2$, equilibrates with the heating rate yielded by the local flux, $\bar{E}_0 \bar{\sigma}_0 \Phi_c / 4\pi R^2$ (see also §7).

It is noteworthy that the specific internal energy $\sim (c_{\text{ch}}^{\text{I}})^2$ is not proportional to Γ_{EUV} but exhibits a slightly slower increase, scaling as $\Gamma_{\text{EUV}}^{2/3}$. This originates from the drawback of increasing the gas temperature: while higher Φ_{EUV} can increase the internal energy, the resulting short crossing time (R/c_{ch}) leads to a shorter integration time of Γ_{EUV} and, thereby, a reduced total deposited energy during the gas traveling to the height of $\sim R$, where the bulk of photoheating and photoionization takes place. This also implies that the fraction of the deposited energy going into the kinetic energy of the gas (and being drained by cooling) increases with Φ_{EUV} (§7).

For Type II winds (right panel of Figure 2), the total energy gain is the sum of the initially injected energy until the launched atomic hydrogen gets ionized, plus the additional energy resulting from the reionizations of recombined hydrogen within the H II region. The initial deposited energy is estimated as the product of t_{ioni} and Γ_{EUV} with $y_{\text{HI}} \approx 1$, which is equivalent to \bar{E}_0 . To quantify this, we can introduce a spectral hardness parameter by normalizing the initially injected energy with the enthalpy of the gas at the equilibrium temperature:

$$\begin{aligned} \varepsilon &\equiv \frac{\bar{E}_0}{m c_p c_{\text{eq}}^2} \\ &\approx 1 \left(\frac{\bar{E}_0}{3.7 \text{ eV}} \right) \left(\frac{m}{1.4 m_{\text{H}}} \right)^{-1} \left(\frac{c_p}{5/2} \right)^{-1} \left(\frac{c_{\text{eq}}}{10 \text{ km s}^{-1}} \right)^{-2}. \end{aligned} \quad (18)$$

When $\varepsilon > 1$, it signifies a hard spectrum, indicating that the gas could potentially be heated to a temperature higher

than the equilibrium temperature by a single photoionization event.

The additionally supplied energy through reionizations is obtained by calculating the integration (Eq.(15)) from $s = s_1$ to $s = R$ with approximating y_{HI} in Γ_{EUV} to the ionization-recombination equilibrium abundance $y_{\text{HI}} \sim t_{\text{ioni}}/t_{\text{rec}}$ (Eq.(11)). Hence, the expression for c_{ch} for Type II winds are derived by solving this implicit equation with respect to $c_{\text{ch}}^{\text{II}}$:

$$\left(\frac{c_{\text{ch}}^{\text{II}}}{c_{\text{eq}}} \right)^2 = \varepsilon + \left(\frac{\varphi \varepsilon q}{x} \right)^{1/2} \left(\frac{c_{\text{ch}}^{\text{II}}}{c_{\text{eq}}} \right)^{-1.75} \left(1 - \varphi^{-1} \varepsilon x \frac{c_{\text{ch}}^{\text{II}}}{c_{\text{eq}}} \right),$$

The first and second terms of the RHS correspond to the initially injected energy and additional energy through reionizations, respectively. We refer the readers to §4.4 (Eq.(43)) for the derivation of this equation.

The root of the above implicit equation can be described by simple expressions in some special cases. When t_{rec} is sufficiently longer than R/c_s so that energy addition due to reionizations can be ignored, $c_{\text{ch}}^{\text{II}}$ is approximated to

$$c_{\text{ch}}^{\text{II}} \approx c_1 \equiv \varepsilon^{1/2} c_{\text{eq}},$$

by dropping the second term on the RHS of the above equation. On the other hand, when recombination is sufficiently rapid, $t_{\text{rec}} \ll R/c_s$, the reionization term dominates, and $c_{\text{ch}}^{\text{II}}$ is approximated to

$$c_{\text{ch}}^{\text{II}} \approx c_2 \equiv c_{\text{eq}} \left(\frac{\varphi_{\text{II}}}{x} \right)^{1/7.5}, \quad (19)$$

where φ_{II} is the EUV emission rate normalized by the secondary critical EUV emission rate for recombination-dominated Type II winds,

$$\Phi_{\text{c,rec}}^{\text{II}} \equiv \frac{\Phi_c}{\varepsilon q}.$$

Again, both c_{ch}^{I} and $c_{\text{ch}}^{\text{II}}$ represent different forms of c_{ch} and thus serve as indicators of the heating timescale, not necessarily providing the actual sound speed of the wind, c_s , which is presented in the following section.

3.3. Typical Flow Velocities

When photoheating operates on a timescale shorter than gravitational deceleration, such that $t_{\text{h}} < t_{\text{g}}$, winds can be rapidly heated to have c_s exceeding the escape velocity v_{g} without feeling the gravity, implying that the wind does not experience a large pressure drop. In such instances, the typical flow velocity of the freely photoevaporating winds can approximate the isothermal sound speed, i.e., $\mathcal{M} \sim 1$.

In a case of strong photoheating where $c_{\text{ch}} > c_{\text{eq}}$, the gas undergoes immediate heating to a high temperature where

cooling is activated. This regulates the gas temperature to maintain $c_s \approx c_{eq}$. For $x > 1$, this renders vigorous isothermal winds at the equilibrium temperature with a typical velocity of c_{eq} . The temperature equilibration occurs within a quite short distance, $s \approx c_{eq}t_h = R(c_{eq}/c_{ch})$.

In cases where $v_g < c_{ch} < c_{eq}$, gravitational deceleration is negligible, but heating is not rapid enough to heat the gas to the equilibrium temperature within $s \lesssim R$. Here, neither cooling nor gravity significantly influences the wind, resulting in forming free winds with $c_s \approx c_{ch}$ and $\mathcal{M} \sim 1$.

Conversely, when the heating timescale is longer than the gravitational timescale, or equivalently $c_{ch} < v_g$, gravity can inhibit winds significantly. This takes place typically at small distances with either low EUV emission rates or hard spectra. Regardless of the emphasized gravitational effect, photoheated gas will not be completely hydrostatic, as the gas does not have an alternative option other than forming winds to process the continuously deposited energy due to its too low temperature to activate cooling. In these escaping winds, a steady state is achieved such that the sound speed at a height of $\sim R$ is maintained at $\sim v_g$. The typical flow speed of such gravity-inhibited winds can be estimated using the self-consistent condition (cf. Eq.(15)):

$$c_p v_g^2 \approx \int \Gamma_{EUV} \frac{ds}{\mathcal{M} v_g}.$$

This reflects that when the heating timescale is long, the flow speed is self-regulated so that the gas can take a long time to reach $\sim R$ to obtain $\sim c_p v_g^2$ worth of energy with a low heating rate. Essentially, the above definition results in an estimated Mach number of

$$\mathcal{M}_g \equiv \mathcal{M} \approx \left(\frac{t_g}{t_h} \right)^3, \quad (20)$$

indicating that winds are subsonic at $\sim R$. The location of the sonic point is considerably farther from the base, $\sim (t_g/t_h)^{-6} R$ (Begelman et al. 1983).

The specific form of the Mach number (Eq.(20)) for gravity-inhibited Type I winds is derived as

$$\mathcal{M} \sim \mathcal{M}_g^I \equiv \varphi x^{1/2},$$

and that for gravity-inhibited Type II winds is

$$\mathcal{M} \sim \mathcal{M}_g^{II} \equiv \left(\frac{\varphi q x^\beta}{\varepsilon} \right)^{1/2} \left[x^{-1} \varepsilon^{-1} - 1 + \left(\frac{\varepsilon q x^{\beta+1}}{\varphi} \right)^{1/2} \right]^{-1}.$$

In either wind type, the Mach number increases with the EUV emission rate and reaches unity at $t_h = t_g$.

The hydrodynamical characteristics of the isothermal wind, free wind, and gravity-inhibited wind regimes can be

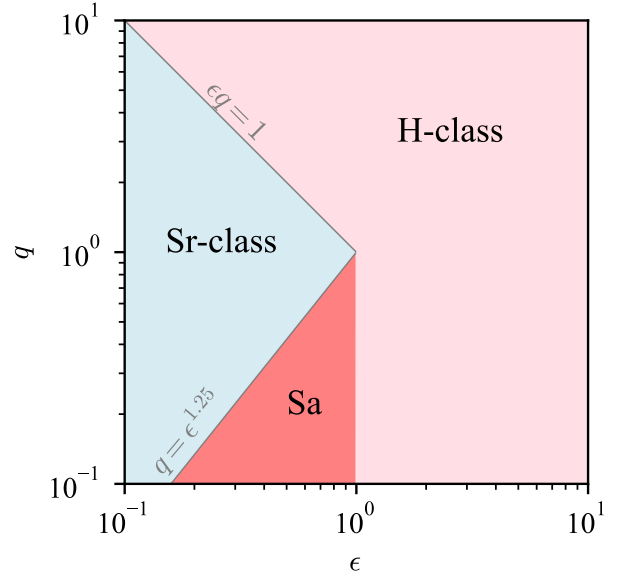


Figure 3. Illustration of the spectrum-hardness diagram for the EUV photoevaporation classes (cf. Table 2). When the spectrum parameter ε (Eq.(18)) and ratio of recombination to photoionization q (Eq.(12)) for a given EUV spectrum is positioned in $\varepsilon > 1$ or $\varepsilon q > 1$, it is categorized into the hard-spectrum class (H-class). The other cases are classified into the soft-spectrum classes. For $q < \varepsilon^{1.25}$, recombination is slow, and advection is more effective in maintaining atomic hydrogen within the launched gas. We call this class Sa-class. The opposite class $q > \varepsilon^{1.25}$, where recombination is rapid, is termed as Sr-class. Here, $\beta = 0.75$ is used.

summarized as Table 1. In BMS83, the corresponding parameter spaces are labeled as Regions A, B, and C, respectively. We follow this notation, but in our model, each regime bifurcates depending on the wind's chemical state, as we will see in the following sections (see also Table 3). The three regimes cover different areas on the x - φ phase diagram, depending on the EUV photoevaporation class.

3.4. EUV Photoevaporation Classes

Varying spectral hardness results in differing relative magnitudes of photoheating and photoionization. For instance, a soft spectrum yields a relatively low amount of energy deposited into the gas per photoionization. In such cases, while winds are readily photoionized, efficiently heating them proves challenging. Hence, differences in spectral hardness suggest distinct combinations of the thermal and ionization states for winds at given Φ_{EUV} and R .

By evaluating Eqs.(13) and (14), we find the distinct classes of EUV photoevaporation that are uniquely determined by the two spectrum-hardness parameters, ε and q

| Regime | Description | Condition | Typical Sound Speed: c_s | Typical Mach Number: \mathcal{M} |
|--------|------------------------|---------------------------------------|----------------------------|------------------------------------|
| A | Isothermal wind | $c_{\text{ch}} > c_{\text{eq}}$ | $\sim c_{\text{eq}}$ | ~ 1 |
| B | Free wind | $v_g < c_{\text{ch}} < c_{\text{eq}}$ | $\sim c_{\text{ch}}$ | ~ 1 |
| C | Gravity-inhibited wind | $c_{\text{ch}} < v_g$ | $\sim v_g$ | $\sim (t_g/t_h)^3$ |

Table 1. Summary of wind regimes.

(Eqs.(18) and (12)),

$$\varepsilon \equiv \frac{\bar{E}_0}{mc_p c_{\text{eq}}^2} \approx 1 \left(\frac{\bar{E}_0}{3.7 \text{ eV}} \right) \left(\frac{m}{1.4 m_{\text{H}}} \right)^{-1} \left(\frac{c_p}{5/2} \right)^{-1} \left(\frac{c_{\text{eq}}}{10 \text{ km s}^{-1}} \right)^{-2}$$

$$q \equiv \frac{3C^2 \alpha_{\text{eq}}}{c_{\text{eq}} \bar{\sigma}_0} \approx 0.1 \left(\frac{C}{0.4} \right)^2 \left(\frac{\alpha_{\text{eq}}}{2 \times 10^{-13} \text{ cm}^3 \text{ s}^{-1}} \right)$$

$$\times \left(\frac{c_{\text{eq}}}{10 \text{ km s}^{-1}} \right)^{-1} \left(\frac{\bar{\sigma}_0}{10^{-18} \text{ cm}^2} \right)^{-1}.$$

The class of EUV photoevaporation is identified by the lo-

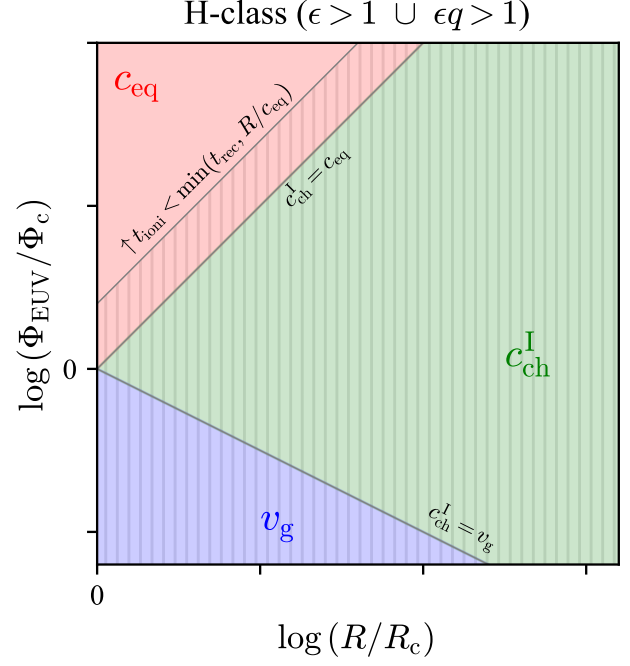
| Class name | Parameter space | Relevant source |
|------------|---|-----------------|
| H-class | $\{(\varepsilon, q) \mid \varepsilon > 1 \cup \varepsilon q > 1\}$ | T Tauri star |
| Sa-class | $\{(\varepsilon, q) \mid \varepsilon < 1, q < \varepsilon^{1.25}\}$ | MS IM star |
| Sr-class | $\{(\varepsilon, q) \mid \varepsilon q < 1, q > \varepsilon^{1.25}\}$ | None(?) |

Table 2. EUV photoevaporation classes and corresponding parameter spaces. $\beta = 0.75$ is used here. (See also Figure 3.) The right column shows potentially relevant radiation sources to each class, where “MS IM star” denotes main-sequence intermediate-mass star.

cation of the given spectrum’s ε and q on the ε – q phase diagram (Figure 3). The corresponding parameter spaces are summarized in Table 2. The hard spectrum class is referred to as “H-class,” while the soft spectrum classes are denoted as “Sa-class” or “Sr-class.” The lower-case letters of the soft spectrum classes stand for “advection” and “recombination,” respectively. We will delve into the characteristics of each class in Sections 3.5–3.7.

For young low-mass stars, in particular, EUV spectra might be classified into the H-class since ε easily exceeds unity if there is a contribution of energetic EUV originating from the stellar magnetic activity. However, the possibility remains that the spectra of low-mass stars are classified into the soft-spectrum classes if those low-mass stars have dominating accretion-originated soft EUV. A blackbody with the effective temperatures of $\lesssim 5 \times 10^4$ K falls into the soft spectrum class.

A necessary condition to be in the soft-spectrum classes is that the average deposited energy \bar{E}_0 is less than $mc_p c_{\text{eq}}^2 \approx 3.7 \text{ eV}$. This indicates most EUV photons have energies close to the Lyman limit. Such extremely soft spectra would be possible for stars without convective zones, like main-sequence stars with intermediate masses, where EUV emission is mostly covered by moderately hot photospheres.

**Figure 4.** Phase diagram for the H-class. The horizontal axis is normalized radius $x = R/R_c$, and the vertical axis is normalized EUV emission rate $\varphi = \Phi_{\text{EUV}}/\Phi_c$. The red- and blue-shadings are the isothermal-wind (Regime A) and gravity-inhibited (Regime C) regimes, respectively. The parameter space of steadily-heated, free winds (Regime B, or equivalently Regime B-I) is colored in green. Different colors indicate the typical sound speed c_s (see also Table 1 for the chemical and hydrodynamical characteristics of each regime.) The gray vertical stripes represent the Type I regime, where photoevaporative winds are atomic. The remaining area is Type II. Regime A has both Type I and II regimes, while the others do not. This is a unique feature for the H-class.

3.5. H-Class

This scenario corresponds to cases where the EUV spectrum is relatively hard (see Table 2). In such instances, EUV can deposit a relatively large amount of energy into the gas per photoionization, enabling efficient heating of the gas. In other words, this class has a relatively short heating timescale for a photoionization timescale. Stars with active surface magnetic activities are anticipated to exhibit EUV spectra falling under this class.

The fast-ionization condition (Eq.(14)) is rewritten to

$$\varphi > \max(1, q) \times \varepsilon x. \quad (21)$$

In this parameter space, the wind becomes ionized (Type II). The remaining parameter space corresponds to Type I winds, depicted by the gray vertical lines in Figure 4.

Photoheating is notably intense when $c_{\text{ch}}^{\text{I}} > c_{\text{eq}}$, or equivalently $\varphi > x$, instantly raising the gas temperature to the equilibrium value. Consequently, the wind becomes isothermal with $c_s \approx c_{\text{eq}}$ in this parameter space. The corresponding area is visually highlighted by the red-shading in Figure 4 and is labeled as Regime A, following Region A of BMS83 (Table 3). Regime A occupies the upper left corner of the x - φ plane, reflecting the tendency for the heating timescale to be generally shorter at smaller R and with higher Φ_{EUV} , i.e., where EUV flux is intense. Ionized winds (Type II) can exist only in Regime A in this class. It is also possible that the winds manifest as an isothermal atomic flow for a lower Φ_{EUV} . With the short heating timescale in this regime, the effect of gravity is minimal, and winds can freely escape at a typical flow speed of $\sim c_{\text{eq}}$.

If Φ_{EUV} is small, or the distance R is large, the heating timescale gets long, and in the ultimate case, t_{h} becomes longer than the gravitational timescale. This condition is equivalent with $c_{\text{ch}}^{\text{I}} < v_{\text{g}}$, and in this case, the wind is significantly inhibited by gravity. The energy deposited by photoheating charges to the gas keeps the isothermal sound speed at $c_s \approx v_{\text{g}}$. This regime is represented by $\varphi < x^{-1/2}$, or equivalently $c_{\text{ch}}^{\text{I}} < v_{\text{g}}$, shown by the blue-shading in Figure 4 (Regime C). The fast-ionization condition is not met there, meaning that gravity-inhibited winds are atomic in this class. Correspondingly, the typical Mach number of gravity-inhibited winds in the H-class is $\sim \mathcal{M}_{\text{g}}^{\text{I}}$.

In the other regime, $x^{-1/2} < \varphi < x$, neither gravity nor cooling significantly affects the system. This regime corresponds to Region B of BMS83, but we label it as Regime B-I in this study to highlight the fact that the winds are atomic, and the sound speed is given by the Type I characteristic sound speed c_{ch}^{I} . Similarly to Regime A, the heating timescale is sufficiently short compared to the gravitational timescale, and thus winds can freely escape at $\mathcal{M} \sim 1$ without being influenced by gravity. However, the heating timescale is not short enough so that gas temperature can reach the equilibrium temperature while traveling to the height of $\sim R$, and hence $c_s \approx c_{\text{ch}}^{\text{I}}$.

3.6. Sa-class

This class is the case when the spectrum is soft, and recombination occurs relatively slowly in the wind. The deposited energy per photoionization is small, and one single photoionization is not sufficient to supply the energy worth of the gas's internal energy at the equilibrium temperature, as opposed to the H-class. A relatively high Φ_{EUV} is required to heat the gas at a certain level than is needed in the H-class. Due to the slow recombination, winds in this class do not necessarily

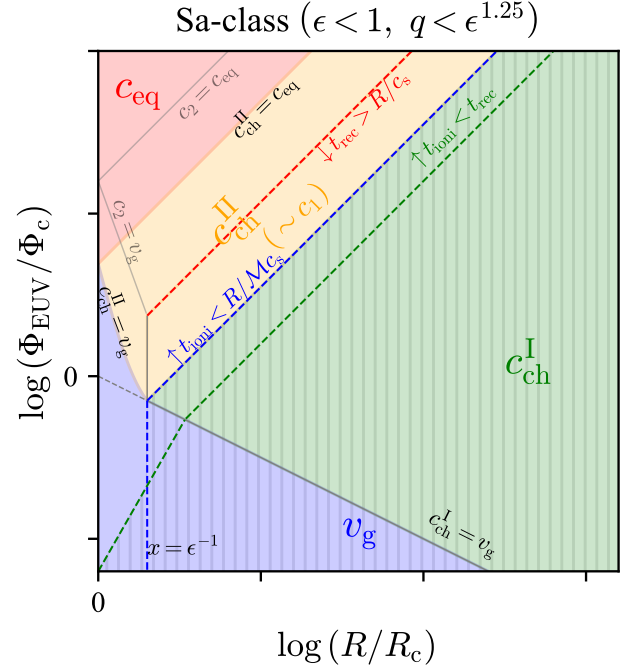


Figure 5. Phase diagram for the Sa-class, which is overall similar to Figure 4. However, Regime B is separated into two subcategories: Regime B-I (green) and Regime B-II (orange). Both are free wind regimes, but the former is for atomic winds (Type I), and the latter is for ionized winds (Type II). The blue-dashed line indicates where the ionization timescale is equal to the crossing timescale $t_{\text{ion}} = R/Mc_s$; the ionization timescale is shorter above this line. The green-dashed line is where the ionization and recombination timescales are equal; again, the ionization timescale is shorter above this line. The boundary where the recombination and wind crossing timescale is equal is represented by the red-dashed line, below which the recombination timescale is longer. This class is visually distinguished from the other classes by the parameter space having the presence of the orange area attaching to the blue-dashed line and the red-dashed line positioning in the Type II regime.

undergo secondary photoionization following the initial photoionization at the launching point until the escaping gas travels to the height of $\sim R$. Stars lacking surface magnetic activities, such as main-sequence intermediate-mass stars, would have EUV spectra classified into this class.

The fast-ionization condition is rewritten to

$$\begin{cases} \varphi > \varepsilon q x^{1+\beta} & \text{for } 1 \leq x < \varepsilon^{-1} \\ \varphi > \varepsilon^{3/2} x & \text{for } x > \varepsilon^{-1} \end{cases} \quad (22)$$

which is equivalent to $t_{\text{ion}} < R/c_s$ for $x < \varepsilon^{-1}$ (green dashed line) and $t_{\text{ion}} < R/c_s$ for $x > \varepsilon^{-1}$ (blue dashed line). In this parameter space, the wind becomes ionized (Type II), while the remaining parameter space (the area covered by gray vertical lines in Figure 5) represents the atomic-wind regime (Type I). For $x > \varepsilon^{-1}$, atoms in the winds are maintained primarily through advection from the upstream region rather

| Regime | Subregime | Dynamical state | Chemical state | c_s | \mathcal{M} | Color |
|--------|-----------|----------------------------|-------------------|----------------------------------|----------------------------------|----------------------------------|
| A | A-I | Isothermal Wind | Atomic (Type I) | $\sim c_{\text{eq}}$ | ~ 1 | red (w/ gray vertical stripes) |
| | A-II | | Ionized (Type II) | | | red (w/o gray vertical stripes) |
| B | B-I | Steadily Heated, Free Wind | Atomic (Type I) | $\sim c_{\text{ch}}^{\text{I}}$ | ~ 1 | green |
| | B-II | Free Wind | Ionized (Type II) | $\sim c_{\text{ch}}^{\text{II}}$ | | orange |
| C | C-I | Gravity-inhibited wind | Atomic (Type I) | $\sim v_g$ | $\sim \mathcal{M}_g^{\text{I}}$ | blue (w/ gray vertical stripes) |
| | C-II | | Ionized (Type II) | | $\sim \mathcal{M}_g^{\text{II}}$ | blue (w/o gray vertical stripes) |

Table 3. Qualitative characteristics of the chemical and hydrodynamical states for winds in each regime. Each of the fundamental three regimes (Regimes A, B, and C; see Table 1) has two subregimes according to the wind types. The listed “Color” in the last column is used in Figures 4, 5, 6, and 7 to represent the corresponding parameter space on the phase diagrams, differentiating the typical sound speeds of winds c_s . Note that Regime A-I is only possible in the H-class, while Regimes B-II and C-II are present only in the Sa- and Sr-classes.

than reproduced by recombination, and vice versa for $x < \varepsilon^{-1}$. The blue dashed line, where $t_{\text{ioni}} = R/c_s$, is vertical at $x = \varepsilon^{-1}$ in Figure 5. This implies that steady winds cannot develop without additional energy deposition through reionizations in $x < \varepsilon$, since the initially injected energy is never sufficient for heating the gas to yield an escaping speed.

Contrary to the H-class, isothermal winds of this class (Regime A; the red-shade in Figure 5) are always in an ionized state. The corresponding parameter space is where the heating timescale is sufficiently short, i.e., $c_{\text{ch}}^{\text{II}} > c_{\text{eq}}$, or equivalently

$$\varphi > f_{\text{eq}}(\varepsilon, q)x,$$

where

$$f_{\text{eq}}(\varepsilon, q) \equiv \frac{4\varepsilon q}{\left(\sqrt{(\varepsilon^{-1}-1)^2 + 4q} - (\varepsilon^{-1}-1)\right)^2}.$$

The factor f_{eq} is larger than unity for soft spectrum classes ($\varepsilon < 1$, $\varepsilon q < 1$), meaning that on the x - φ plane, the $c_{\text{ch}}^{\text{II}} = c_{\text{eq}}$ line is located above $c_{\text{ch}}^{\text{I}} = c_{\text{eq}}$ line, which separated Regimes A and B in the H-class. This results from more efficient heating in an atomic gas than in an ionized gas since the absorber per gas mass is higher. The reduced heating rate necessitates a higher Φ_{EUV} to heat the gas to the equilibrium value ($c_s = c_{\text{eq}}$), compared to what would be required if the gas were atomic ($\varphi > x$, or equivalently $c_{\text{ch}}^{\text{I}} > c_{\text{eq}}$).

In the limit of $(\varepsilon^{-1}-1)^2 \gg 4q$, which is often the case for Sa-class spectra (Table 3), f_{eq} is approximated to

$$f_{\text{eq}} \approx \frac{(1-\varepsilon)^2}{\varepsilon q} \quad \left(\text{for } (\varepsilon^{-1}-1)^2 \gg 4q\right).$$

A distinct characteristic of the soft-spectrum classes is that ionized winds can be inhibited by gravity. This occurs when the heating timescale is shorter than the gravitational timescale. For Type II winds, this condition is expressed by $c_{\text{ch}}^{\text{II}} < v_g$, which is rewritten to

$$\begin{aligned} \varphi &< \varphi_g(x; \varepsilon, q, \beta) \\ &\equiv \left(\frac{2\sqrt{q\varepsilon}x^{(\beta+1)/2}}{\sqrt{(x^{-1}\varepsilon^{-1}-1)^2 + 4qx^{(2\beta+1)/2}} - (x^{-1}\varepsilon^{-1}-1)} \right)^2, \end{aligned}$$

Hence, the parameter space for the gravity-inhibited, Type II winds is expressed by

$$\left\{ (x, \varphi) \mid x < \varepsilon^{-1}, \varphi > \varepsilon q x^{\beta+1}, \varphi < \varphi_g \right\}.$$

In this parameter space, typical sound speed and flow speed are $\sim v_g$ and $\sim \mathcal{M}_g^{\text{II}}$, respectively. This space has a shape that looks like extruding the blue-shaded area upward on the x - φ plane within $x < \varepsilon^{-1}$, compared to Regime C of the H-class. Again, this distinction highlights the lower heating efficiency in an ionized wind than in an atomic wind. Therefore, in order to deposit sufficient energy for the gas to form steadily escaping winds, shortening the recombination timescale by increasing flow density, i.e., increasing Φ_{EUV} , is needed. This facilitates the (re)production of atomic hydrogen, which is subsequently reionized in the wind, resulting in secondary energy deposition.

Another unique characteristic of the soft-spectrum classes is having the parameter space of free winds that are ionized (orange-shaded area in Figure 5). In this regime, the heating timescale is sufficiently shorter than the gravitational timescale while not being short enough to heat the gas to reach the equilibrium temperature. The photoionization timescale is also sufficiently short to make the photoheated gas ionized in this regime. As a result, the typical sound speed and Mach number of the ionized winds are given by $\sim c_{\text{ch}}^{\text{II}}$ and ~ 1 , meaning lower-temperature ionized winds in contrast to the canonical picture.

The soft-spectrum classes are distinguished by the rapidity of recombination within free-ionized winds. It differentiates the magnitude of the additionally deposited energy through reionizations with respect to the initially injected energy. The Sa-class has relatively slow recombination and thus always has a parameter space where the contribution of additional energy deposition is minimal. This is especially the case in the vicinity of the Type I and Type II boundary in Regime B (blue-dashed line in Figure 5). The sound speed and flow speed can be well approximated to $\sim c_1$ there. In the zeroth order, this approximation is valid as long as the recombination timescale is longer than the wind crossing timescale.

the stellar property, namely the spectral shape of EUV and the stellar mass, and the disk gas property, namely gas mass per hydrogen nucleus and the equilibrium sound speed.

Using the EUV emission rate normalized by the critical EUV emission rate

$$\varphi \equiv \frac{\Phi_{\text{EUV}}}{\Phi_c},$$

we denote the characteristic sound speed of Eq.(23) as

$$c_{\text{ch}}^{\text{I}} \equiv c_{\text{eq}} \left(\frac{\varphi}{x} \right)^{1/3}$$

to emphasize this being c_{ch} for Type I winds (cf. Eq.(16)). In this paper, we use c_{ch}^{I} as the characteristic sound speed of the Type I wind instead of the more strict expression Eq.(23) for simplicity. This means that we analyze under the idealization that a large portion of the wind region is optically thin ($\chi_e \sim 1$), following Begelman et al. (1983). While this idealization restricts our model's applicability, it simplifies our analysis. This idealization is a reasonable approximation for spectra with minimal photon energy dispersion, where most photons are intensively absorbed at a certain column density. Examples include relatively soft spectra dominated by photons near the Lyman limit or harder spectra with delta-function-like shapes. Regardless of these limitations, the adopted approach is an essential first step towards developing a more comprehensive model available for a wider range of spectra. Besides, the insights gained from our simplified model provide a foundation for tackling more general cases. In §8, We delve deeper into the potential impacts of this adopted approximation.

The Type I characteristic sound speed c_{ch}^{I} increases with Φ_{EUV} and eventually exceeds c_{eq} when $\Phi_{\text{EUV}} > \Phi_c x$. This means the photoheating is so strong that the gas temperature could potentially exceed the equilibrium value c_{eq} . However, as explained in §3.3, it does not happen for real; instead, cooling gets activated to force the actual sound speed c_s to stay at c_{eq} . In other words, coolants act as a resistance force for gas temperature so as not to exceed the terminal value c_{eq} .

On the contrary, when heating is weak, the characteristic sound speed can get lower than v_g , or equivalently $t_h > t_g$. This appears as if the gas would be bounded so that it forms a hydrostatic atmosphere; however, this is not the case. Even if the gas is indeed in hydrostatic equilibrium at first, the energy will be continuously charged to the gas to increase the temperature gradually, as the deposited energy cannot be processed by radiative cooling at this low temperature. At some point, c_s will eventually reach the escaping velocity v_g , forming slow winds. The system would achieve a steady state such that the sound speed is maintained of the order of $v_g (= \sqrt{GM/2c_p R})$ with a small flow velocity of

$$v \sim \left(\frac{t_g}{t_h} \right)^3 v_g = \left(\frac{c_{\text{ch}}^{\text{I}}}{v_g} \right)^3 v_g = \varphi x^{1/2} v_g,$$

which indicates

$$\mathcal{M}_g^{\text{I}} = \varphi x^{1/2} \quad (\text{for Type I})$$

(cf. Eq.(20)). This gravity-inhibited-wind regime occurs when $c_{\text{ch}}^{\text{I}} < v_g$, i.e., when the ratio of

$$\frac{c_{\text{ch}}^{\text{I}}}{v_g} = \left(\varphi x^{1/2} \right)^{1/3} \quad (24)$$

gets lower than unity.

4.2. Photoionization-Related Parameters

As explained in §3.1, the picture of the Type I wind is valid only when the photoionization timescale is longer than the recombination or crossing timescale of the wind (left panel of Figure 2). This condition is expressed by the slow photoionization condition, Eq.(13),

$$t_{\text{ioni}} > \min(t_{\text{rec}}, R/\mathcal{M}c_s).$$

The Type I characteristic sound speed c_{ch}^{I} (Eq.(16)) is available only in this parameter space, for which we will identify the expressions in the following sections. To that end, we introduce photoionization-relevant quantities in this section.

After the photo-energy is injected into a new H I layer close to the $\tau_{\text{EUV}} \sim 1$ surface, a launched hydrogen atom takes t_{ioni} to be photoionized in general. The flowing hydrogen atom can survive to a distance of

$$\begin{aligned} \Delta s_{\text{suV}} &\equiv \mathcal{M}c_s t_{\text{ioni}} \\ &\approx 1.9 \text{ au} \left(\frac{v}{10 \text{ km s}^{-1}} \right) \left(\frac{\Phi_{\text{EUV}}}{10^{40} \text{ s}^{-1}} \right) \\ &\quad \times \left(\frac{r}{10 \text{ au}} \right)^{-2} \left(\frac{\bar{\sigma}_0}{10^{-18} \text{ cm}^2} \right) \left(\frac{\mathcal{M}}{1} \right) \end{aligned}$$

at the shortest. We note that Δs_{suV} is a *potential* thickness of the photoheated H I layer and does not necessarily represent the actual thickness of it. When recombination is strong, i.e., $t_{\text{rec}} < R/\mathcal{M}c_s$, the recombination timescale determines the thickness of the photoheated H I layer, as implied by the slow photoionization condition, Eq.(13).

The condition, $\Delta s_{\text{suV}} > R$, is a sufficient condition for winds to be Type I. This is rewritten to

$$\frac{R}{\mathcal{M}c_s t_{\text{ioni}}} = \mathcal{M}^{-1} \left(\frac{c_s}{c_{\text{eq}}} \right)^{-1} \frac{\Phi_{\text{EUV}}}{\Phi_{c,i} x} \chi_i < 1, \quad (25)$$

and $\Phi_{c,i}$ is the photoionization critical EUV emission rate

$$\begin{aligned} \Phi_{c,i} &\equiv \frac{4\pi G M_*}{2c_p c_{\text{eq}} \bar{\sigma}_0} = \Phi_c \frac{\bar{E}_0}{c_p m c_{\text{eq}}^2} \\ &\approx 3.3 \times 10^{38} \text{ s}^{-1} \left(\frac{M_*}{1 M_\odot} \right) \left(\frac{c_p}{5/2} \right)^{-1} \\ &\quad \times \left(\frac{c_{\text{eq}}}{10 \text{ km s}^{-1}} \right)^{-1} \left(\frac{\bar{\sigma}_0}{1 \times 10^{-18} \text{ cm}^2} \right)^{-1}. \end{aligned}$$

Again, the critical EUV emission rate of photoionization depends only on the stellar parameters and disk gas properties. Similarly to χ_e , χ_i is expected to be of the order of unity in the photoheated layer. Therefore, we ignore χ_i in the following sections to remove complexity from our order-of-magnitude estimation (again, see §8.4 for the potential impact of this simplification).

Here, we retrieve one of the spectral hardness parameters, ε (Eq.(18)),

$$\varepsilon \equiv \frac{\Phi_{c,i}}{\Phi_c} = \frac{\bar{E}_0}{c_p m c_{eq}^2}$$

$$1 \approx \left(\frac{\bar{E}_0}{3.7 \text{ eV}} \right) \left(\frac{c_p}{5/2} \right)^{-1} \left(\frac{m}{1.4 m_H} \right)^{-1} \left(\frac{c_{eq}}{10 \text{ km s}^{-1}} \right)^{-2}.$$

This parameter characterizes the spectral hardness for the advection of atomic hydrogen. The inverse ε^{-1} is physically interpreted as the number of photoionization necessary to heat the gas to the equilibrium temperature, or equivalently to have an energy of $c_p m c_{eq}^2$. If $\varepsilon > 1$, the spectrum is heating-oriented; the gas can get the heat exceeding $c_p m c_{eq}^2$ with only single photoionization of atomic hydrogen. Conversely, for $\varepsilon < 1$, the spectrum is ionization-oriented; multiple photoionization is needed to heat the gas to $c_p m c_{eq}^2$. A relatively large amount of energy is consumed through photoionization rather than heating in this case. We stress that ε is determined by the spectral shape of EUV and is independent of the absolute value of the incident flux or Φ_{EUV} .

Using the dimensionless quantities, the recombination timescale Eq.(10) is rewritten to

$$t_{\text{rec}} = \frac{R_c}{c_{eq}} \left(\frac{q \varepsilon^{-1} \varphi}{x^3} \right)^{-1/2} \left(\frac{c_s}{c_{eq}} \right)^{\beta}. \quad (26)$$

Here, we find the other spectral hardness parameter, q (Eq.(12)),

$$q \equiv \frac{3C^2 \alpha_{eq}}{c_{eq} \bar{\sigma}_0}$$

$$\approx 0.096 \left(\frac{C}{0.4} \right)^2 \left(\frac{\alpha_{eq}}{2 \times 10^{-13}} \right)$$

$$\times \left(\frac{c_{eq}}{10 \text{ km s}^{-1}} \right)^{-1} \left(\frac{\bar{\sigma}_0}{10^{-18} \text{ cm}^2} \right)^{-1}$$

The q parameter also characterizes the spectral hardness for hydrogen recombination, similarly to ε . (See §2.3 for a physical interpretation.)

We can evaluate the right-hand side (RHS) of the slow ionization condition (Eq.(13)) by considering the ratio between t_{rec} and $R/\mathcal{M}c_s$,

$$\frac{R}{\mathcal{M}c_s t_{\text{rec}}} = \left(\frac{\varphi q}{\varepsilon x} \right)^{1/2} \left(\frac{c_s}{c_{eq}} \right)^{-(1+\beta)} \mathcal{M}^{-1}. \quad (27)$$

Also, we can compare the ratio between t_{ioni} and t_{rec} as

$$\frac{t_{\text{ioni}}}{t_{\text{rec}}} = \left(\frac{\varepsilon q x}{\varphi} \right)^{1/2} \left(\frac{c_s}{c_{eq}} \right)^{-\beta}, \quad (28)$$

For $t_{\text{ioni}} \ll t_{\text{rec}}$, this ratio gives an approximate H I abundance in the photoionization-recombination equilibrium

$$y_{\text{HI}} \approx \left(\frac{\varepsilon q x}{\varphi} \right)^{1/2} \left(\frac{c_s}{c_{eq}} \right)^{-\beta}, \quad (\text{for } t_{\text{ioni}} < t_{\text{rec}}). \quad (29)$$

4.3. Type I Regime

Now we will find the expressions for the parameter space that satisfies the Type I wind condition (Eq.(13)). Recalling that typical c_s and flow velocity follow the three pattern summarized in Table 1 (regardless of the wind types), the slow photoionization condition Eq.(13) is equivalent with the sum of these three conditions:

Condition I-1: $c_{\text{ch}}^I > c_{eq} \cap t_{\text{ioni}} > \min [t_{\text{rec}}(c_s = c_{eq}), R/c_{eq}]$.

Condition I-2: $c_{\text{ch}}^I < v_g \cap t_{\text{ioni}} > \min [t_{\text{rec}}(c_s = v_g), R/\mathcal{M}_g^I v_g]$.

Condition I-3: $v_g < c_{\text{ch}}^I < c_{eq} \cap t_{\text{ioni}} > \min [t_{\text{rec}}(c_s = c_{\text{ch}}^I), R/c_{\text{ch}}^I]$.

First, we consider Condition I-1. If $\varphi > \varepsilon q^{-1} x$ (cf. Eq.(27)), the recombination timescale is faster than the replenishment of atomic hydrogen through advection, and Condition I-1 reduces to

$$\{(x, \varphi) \mid \varphi > x, \varepsilon q x > \varphi, \varphi > \varepsilon q^{-1} x\}$$

using Eqs.(28) and (16). In the opposite case $\varphi < \varepsilon q^{-1} x$, the Condition I-1 reduces to

$$\{(x, \varphi) \mid \varphi > x, t_{\text{ioni}} > R/c_{eq}, \varphi < \varepsilon q^{-1} x\}$$

where

$$\frac{R}{t_{\text{ioni}} c_{eq}} = x^{-1} \frac{\Phi_{\text{EUV}}}{\Phi_{c,i}} = \varphi \varepsilon^{-1} x^{-1} \quad (30)$$

Hence, Condition I-1 is equivalent to the sum of

$$\{(x, \varphi) \mid \varphi > x, \varphi < \varepsilon q x, \varphi > \varepsilon q^{-1} x\} \quad (31)$$

and

$$\{(x, \varphi) \mid x > 1, x < \varepsilon, x < \varepsilon q^{-1}\}. \quad (32)$$

After some math, we learn that

$$\varepsilon > 1 \quad \text{or} \quad \varepsilon q > 1 \quad (33)$$

is necessary for (x, φ) to exist, and in this case, Condition I-1 reduces to

$$x < \varphi < \max(\varepsilon, \varepsilon q) \times x.$$

For $\{(\varepsilon, q) \mid \varepsilon < 1, \varepsilon q < 1\}$, the mathematical set of Condition I-1 becomes null, meaning that the Type I winds will never be a high temperature flow at c_{eq} . Qualitatively, the Type I winds with the equilibrium temperature (c_{eq}) form only when the spectrum is hard enough so that one photoionization deposits larger energy than $c_p m c_{\text{eq}}^2$ ($\varepsilon > 1$), or the gas can be heated to $c_s = c_{\text{eq}}$ at a lower Φ_{EUV} than is needed to get $t_{\text{ioni}}/t_{\text{rec}} < 1$. When the spectrum is soft, high-temperature flows (c_{eq}) cannot form unless the wind is Type II. We will see this point later in §4.4.

Next, we consider Condition I-2. The condition $c_{\text{ch}}^{\text{I}} < v_g$ reduces to $\varphi < x^{-1/2}$ (see Eq.(24)), and thus the emission rate relevant here is those having $\varphi < 1$, as we are interested in the region outside the critical radius, $x > 1$. In this case, it is physically trivial that when the spectrum satisfies the hard spectrum condition Eq.(33), $t_{\text{ioni}} > \min[t_{\text{rec}}(c_s = c_{\text{ch}}^{\text{I}}), R/\mathcal{M}_g^{\text{I}} v_g]$ is always met. This is also understood as follows: $c_{\text{eq}} > v_g$ always holds in the radius of interest, $x > 1$, by definition, and Eq.(28) indicates $t_{\text{ioni}} > t_{\text{rec}}$ for $\varepsilon q > 1$. Similarly, when $\varepsilon > 1$,

$$\frac{R}{t_{\text{ioni}} \mathcal{M}_g^{\text{I}} v_g} = \varepsilon^{-1} x^{-1} < 1 \quad (34)$$

and thus $t_{\text{ioni}} > R/v_g$, with x of interest. Hence, Condition I-2 simply reduces to $\varphi < x^{-1/2}$ for $\varepsilon > 1$ or $\varepsilon q > 1$.

The non-trivial case of Condition I-2 is when the spectrum satisfies $\varepsilon < 1$ and $\varepsilon q < 1$, i.e., when the spectrum is soft. Using Eqs.(2), (27), (28), and Eq.(34), Condition I-2 reduces to the sum of

$$\left\{ (x, \varphi) \mid \varphi < x^{-1/2}, \varphi < \varepsilon q x^{1+\beta}, \varphi < q \varepsilon^{-1} x^{-(1-\beta)} \right\}$$

and

$$\left\{ (x, \varphi) \mid \varphi < x^{-1/2}, x > \varepsilon^{-1}, \varphi > q \varepsilon^{-1} x^{-(1-\beta)} \right\}.$$

After tedious mathematics, this condition reduces to the following two cases depending on ε and q :

$$\begin{cases} \varphi < \varepsilon q x^{1+\beta} & \text{for } 1 \leq x < \varepsilon^{-1} \\ \varphi < x^{-1/2} & \text{for } x > \varepsilon^{-1} \end{cases}$$

for $\{(\varepsilon, q) \mid \varepsilon < 1, \varepsilon q < 1, q < \varepsilon^{(2\beta+1)/2}\}$, and

$$\begin{cases} \varphi < \varepsilon q x^{1+\beta} & \text{for } 1 < x < (\varepsilon q)^{-2/(3+2\beta)} \\ \varphi < x^{-1/2} & \text{for } x > (\varepsilon q)^{-2/(3+2\beta)} \end{cases}$$

for $\{(\varepsilon, q) \mid \varepsilon < 1, \varepsilon q < 1, \varepsilon^{(2\beta+1)/2} < q\}$.

Finally, we evaluate Condition I-3. Again, it is trivial that when the spectrum satisfies Eq.(33), the Type I condition is

always met for $c_{\text{ch}}^{\text{I}} < c_{\text{eq}}$. Therefore, here we discuss the non-trivial cases, $\{(\varepsilon, q) \mid \varepsilon < 1, \varepsilon q < 1\}$. To that end, we calculate Eqs.(28) and (27) with $c_s = c_{\text{ch}}^{\text{I}}$ in advance,

$$\frac{t_{\text{ioni}}}{t_{\text{rec}}} \bigg|_{c_s=c_{\text{ch}}^{\text{I}}} = \left(\frac{\Phi_{\text{EUV}}}{\Phi_c x (\varepsilon q)^{3/(3+2\beta)}} \right)^{-(3+2\beta)/6} \quad (35)$$

$$\frac{R}{t_{\text{rec}} c_{\text{ch}}^{\text{I}}} = \left(\frac{\Phi_{\text{EUV}} (\varepsilon q^{-1})^{3/(2\beta-1)}}{\Phi_c x} \right)^{-(2\beta-1)/6} \quad (36)$$

Using these relations and Eqs.(16) and (24), Condition I-3 reduces to the sum of

$$\left\{ (x, \varphi) \mid x^{-1/2} < \varphi < x, \varphi < (q\varepsilon)^{\frac{3}{3+2\beta}} x, \varphi < \left(\frac{q}{\varepsilon} \right)^{\frac{3}{2\beta-1}} x \right\}$$

and

$$\left\{ (x, \varphi) \mid x^{-1/2} < \varphi < x, \varphi < \varepsilon^{3/2} x, \varphi > \left(\frac{q}{\varepsilon} \right)^{\frac{3}{2\beta-1}} x \right\}.$$

Consequently, Condition I-3 reduces to the following two cases depending on ε and q :

$$\left\{ (x, \varphi) \mid \varphi > x^{-1/2}, \varphi < \varepsilon^{3/2} x \right\}$$

for $\{(\varepsilon, q) \mid \varepsilon < 1, \varepsilon q < 1, q < \varepsilon^{(2\beta+1)/2}\}$, and

$$\left\{ (x, \varphi) \mid \varphi > x^{-1/2}, \varphi < (\varepsilon q)^{3/(2\beta+3)} x \right\}$$

for $\{(\varepsilon, q) \mid \varepsilon < 1, \varepsilon q < 1, q > \varepsilon^{(2\beta+1)/2}\}$.

To summarize this section, winds become Type I when satisfying the Type I condition (Eq.(13)),

$$t_{\text{ioni}} > \min \left(t_{\text{rec}}, \frac{R}{\mathcal{M} c_s} \right).$$

This condition covers a certain area on the x - φ plane, depending on the spectral hardness parameters, ε and q , which are uniquely set once an EUV spectrum is given. Based on ε and q , we can classify the x - φ map into the following three different classes:

H-class—Hard spectrum class. This class is defined by $\{(\varepsilon, q) \mid \varepsilon > 1 \cup \varepsilon q > 1\}$. Hot ($c_s = c_{\text{eq}}$), atomic flow is possible only in this case. The Type I regime covers

$$\varphi < \max(1, q) \varepsilon x.$$

on the x - φ plane.

Sa-class—Soft spectrum with advection replenishment. This class is defined by $\{(\varepsilon, q) | \varepsilon < 1, \varepsilon q < 1, q < \varepsilon^{(2\beta+1)/2}\}$. The Type I regime corresponds to

$$\begin{cases} \varphi < \varepsilon q x^{1+\beta} & \text{for } 1 \leq x < \varepsilon^{-1} \\ \varphi < \varepsilon^{3/2} x & \text{for } x > \varepsilon^{-1} \end{cases} \quad (37)$$

Type I flow is possible only with temperatures below the equilibrium value, i.e., $c_s < c_{\text{eq}}$, and the atomic flow is maintained by advection in the steadily heated, free winds ($c_s \sim c_{\text{ch}}^{\text{I}}$).

Sr-class—Soft spectrum with recombination reproduction. This class is defined by $\{(\varepsilon, q) | \varepsilon < 1, \varepsilon q < 1, q > 1\}$. The Type I regime is

$$\begin{cases} \varphi < \varepsilon q x^{1+\beta} & \text{for } 1 \leq x < (\varepsilon q)^{-2/(3+2\beta)} \\ \varphi < (\varepsilon q)^{3/(3+2\beta)} x & \text{for } x > (\varepsilon q)^{-2/(3+2\beta)} \end{cases} \quad (38)$$

Atomic flow is maintained by recombination rather than replenishment through advection.

The top left, top right, and bottom left panels in Figure 7 show the parameter spaces (x, φ) for the H-class, Sa-class, and Sr-class, respectively. In each panel, the Type I regime (Eq.(13)) is represented by gray vertical lines. Generally, the Type I regimes can be subdivided into three regimes: the isothermal wind regime where $c_s \sim c_{\text{eq}}$ (red-shaded area); the steadily heated, free wind regime where $c_s \sim c_{\text{ch}}^{\text{I}}$ (green-shaded area); and the gravity-inhibited wind regime where $c_s \sim v_g$ (blue-shaded area). These three regimes correspond to Regions A, B, and C in BMS83, respectively (cf. Table 1). We follow these notations for the regime labels, but we designate the Type I steadily heated, free wind regime as Regime B-I to highlight its classification as a Type I regime (cf. Table 3).

Again, the class to which a given EUV spectrum is assigned is determined by the location of the spectrum's ε and q on the ε - q plane (the bottom right panel in Figure 7).

4.4. Characteristic Sound Speed: Type II

The remaining parameter space uncovered by the Type I regime is where photoionization is faster than recombination and the replenishment of the atoms through advection (Eq.(14)),

$$t_{\text{ioni}} < \min\left(t_{\text{rec}}, \frac{R}{\mathcal{M}c_s}\right)$$

so that the flow includes the ionized region within $s < R$ (Type II; right panel in Figure 2). In this case, the characteristic sound speed for the Type I winds, c_{ch}^{I} (Eq.(16)), is unavailable to characterize the heating timescale of Type II flows since it has been derived with the assumption of fully atomic winds within $s < R$. Thus, we need to redefine an alternative characteristic sound speed for Type II flows, which we address in this section.

For Type II winds, the total energy gain during the gas flowing to the height $\sim R$ is decomposed into two parts. The first component is the initially injected energy until a launched atomic hydrogen undergoes photoionization once. The launched atomic hydrogen can survive, on average, for a timescale of t_{ioni} and thus can travel a distance of $\sim \mathcal{M}c_s t_{\text{ioni}}$. The surviving distance corresponds to s_{II} , the length of the neutral part depicted in the right panel of Figure 2. It is worth noting that, by definition, the timescale of recombination and advection replenishment is guaranteed longer than the photoionization timescale in the Type II wind, and thus t_{ioni} sets the average timescale for which a newly launched atomic hydrogen can persist in the wind.

The second component is the additional supplied energy by reionizations of recombined hydrogen in the ionized region. Recombination can take place in the H II region if the timescale is sufficiently shorter than the wind crossing timescale. The recombined hydrogen will undergo reionization due to the short ionization timescale, depositing energy to the gas. The H I abundance remains small since $t_{\text{ioni}} < t_{\text{rec}}$.

Hence, to define the characteristic sound speed for Type II winds, $c_{\text{ch}}^{\text{II}}$, we separate the integration range of Eq.(15) for the initially injected energy and secondary deposited energy as

$$c_p c_{\text{ch}}^{\text{II}^2} = \int_0^{s_{\text{II}}} \frac{\bar{\sigma}_0 \bar{E}_0 \Phi_{\text{EUV}}}{4\pi m r^2} \frac{ds}{c_{\text{ch}}^{\text{II}}} + \int_{s_{\text{II}}}^{t_{\text{ioni}}} \frac{\bar{\sigma}_0 \bar{E}_0 \Phi_{\text{EUV}}}{4\pi m r^2} \frac{ds}{c_{\text{ch}}^{\text{II}}}, \quad (39)$$

where s_{II} is the surviving length of launched hydrogen, $s_{\text{II}} = c_{\text{ch}}^{\text{II}} t_{\text{ioni}}$. The first and second terms on the RHS represent the initially injected energy and additional energy supply through reionizations, respectively. Here, we have approximated the H I abundance to unity while the gas undergoes the first photoionization (the first term on the RHS) and to the value set by ionization-recombination equilibrium, $y_{\text{HI}} \sim t_{\text{ioni}}/t_{\text{rec}}$ (Eq.(29)), in the ionized region (the second term on the RHS).

The first term on the RHS of Eq.(39) is explicitly computed as

$$c_p c_1^2 \approx \frac{\bar{\sigma}_0 \bar{E}_0 \Phi_{\text{EUV}}}{4\pi m r^2} t_{\text{ioni}} = \frac{\bar{E}_0}{m} \quad (40)$$

where c_1 is the sound speed corresponding to the initially injected energy. The above equation is rewritten to

$$\frac{c_1}{c_{\text{eq}}} = \varepsilon^{1/2}.$$

This indicates that for $\varepsilon > 1$, heating due to the initially injected energy is sufficiently rapid that the launched gas can reach the equilibrium temperature within a short distance $s < \mathcal{M}c_s t_{\text{ioni}}$. On the other hand, for $c_1 < v_g$, or equivalently $\varepsilon x < 1$, gravity is so strong that the initially injected energy is not enough to form an escaping wind. This suggests that in this range, the additional energy supplied through reionizations is indispensable to form escaping winds.

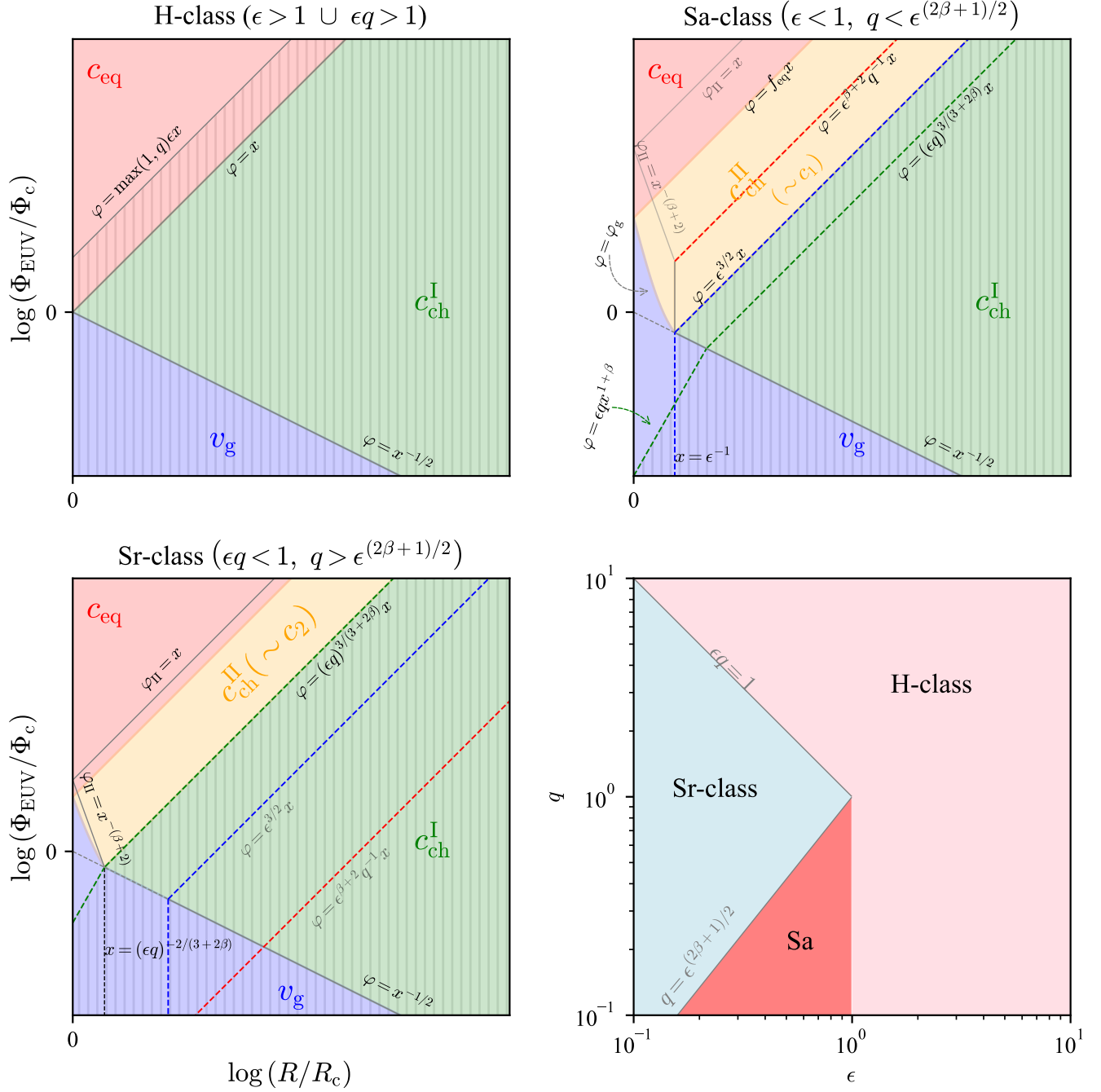


Figure 7. Same as Figures 3, 4, 5, and 6 but with β left unspecified. The expressions for the boundaries are also annotated. The top left, top right, and bottom left panels are those for the H-class, Sa-class, and Sr-class, respectively. The bottom right is the spectral-hardness diagram.

The second integration on the RHS of Eq.(39) can also simplify to

$$\int_{s_{II}}^R \frac{t_{ioni}}{t_{rec}} \frac{\bar{\sigma}_0 \bar{E}_0 \Phi_{EUV}}{4\pi m r^2} \frac{ds}{c_{ch}^{II}} \approx \frac{t_{ioni}}{t_{rec}} \frac{\bar{\sigma}_0 \bar{E}_0 \Phi_{EUV}}{4\pi m r^2} \frac{R - c_{ch}^{II} t_{ioni}}{c_{ch}^{II}}$$

and then the definition of the characteristic sound speed for Type II winds reduces to

$$c_p c_{ch}^{II 2} = c_p c_1^2 + \frac{\bar{\sigma}_0 \bar{E}_0 \Phi_{EUV}}{4\pi m r^2} \frac{t_{ioni}}{t_{rec}} \frac{R - c_{ch}^{II} t_{ioni}}{c_{ch}^{II}}. \quad (41)$$

This equation can be rewritten to

$$\begin{aligned} c_p c_{\text{ch}}^{\text{II}2} &= \frac{\bar{\sigma}_0 \bar{E}_0 \Phi_{\text{EUV}}}{4\pi m r^2} \left[t_{\text{ioni}} + \frac{t_{\text{ioni}}}{t_{\text{rec}}} \left(\frac{R}{c_{\text{ch}}^{\text{II}}} - t_{\text{ioni}} \right) \right] \\ &= \frac{\bar{\sigma}_0 \bar{E}_0 \Phi_{\text{EUV}}}{4\pi m r^2} \left[t_{\text{ioni}} \left(1 - \frac{t_{\text{ioni}}}{t_{\text{rec}}} \right) + \frac{t_{\text{ioni}}}{t_{\text{rec}}} \frac{R}{c_{\text{ch}}^{\text{II}}} \right]. \end{aligned}$$

One can observe from this form that the Type II characteristic sound speed $c_{\text{ch}}^{\text{II}}$ smoothly transitions to the Type I characteristic sound speed c_{ch}^{I} since the boundary between Type I and Type II regimes is expressed by either $t_{\text{ioni}} = t_{\text{rec}}$ or $t_{\text{ioni}} = R/c_{\text{ch}}$ for all classes. This continuity arises because c_{ch}^{I} can be interpreted as a special case of $c_{\text{ch}}^{\text{II}}$ when the surviving distance s_1 is larger than R . It also emphasizes that $c_{\text{ch}}^{\text{II}}$ is defined only in the parameter space where

$$t_{\text{ioni}} < t_{\text{rec}} \quad \cap \quad t_{\text{ioni}} < \frac{R}{c_{\text{ch}}^{\text{II}}} \quad (42)$$

is met. The Type II regime is always included in this parameter space, and thus $c_{\text{ch}}^{\text{II}}$ is always defined in the Type II regime (Eq.(14)).

Eq.(41) can also be rewritten in dimensionless form as

$$\left(\frac{c_{\text{ch}}^{\text{II}}}{c_{\text{eq}}} \right)^2 = \varepsilon + \left(\frac{\varphi \varepsilon q}{x} \right)^{1/2} \left(\frac{c_{\text{ch}}^{\text{II}}}{c_{\text{eq}}} \right)^{-(\beta+1)} \left(1 - \varphi^{-1} \varepsilon x \frac{c_{\text{ch}}^{\text{II}}}{c_{\text{eq}}} \right). \quad (43)$$

The last factor of the second RHS term represents the length of the ionized region. Eq.(43) is also equivalently rewritten to

$$\left(\frac{c_{\text{ch}}^{\text{II}}}{c_{\text{eq}}} \right)^2 = \varepsilon \left[1 - \left(\frac{x \varepsilon q}{\varphi} \right)^{1/2} \left(\frac{c_{\text{ch}}^{\text{II}}}{c_{\text{eq}}} \right)^{-\beta} \right] + \left(\frac{\varphi \varepsilon q}{x} \right)^{1/2} \left(\frac{c_{\text{ch}}^{\text{II}}}{c_{\text{eq}}} \right)^{-(\beta+1)}. \quad (44)$$

The relative strength of the second term to the first term in Eqs.(43) and (44) is determined by the ratio between the crossing timescale and recombination timescale,

$$\frac{R}{c_s t_{\text{rec}}} = \left(\frac{\varphi q}{\varepsilon x} \right)^{1/2} \left(\frac{c_s}{c_{\text{eq}}} \right)^{-(1+\beta)} \quad (45)$$

(cf. Eq.(27)). Again, the RHSs of Eqs.(43) and (44) are guaranteed positive in the parameter space represented by Eq.(42), which is rewritten to a dimensionless form as

$$\left\{ (x, \varphi) \left| \left(\frac{\varepsilon q x}{\varphi} \right)^{1/2} \left(\frac{c_s}{c_{\text{eq}}} \right)^{-\beta} < 1, \varphi > \varepsilon^{3/2} x \right. \right\} \quad (46)$$

This is consistently satisfied in the Type II regime.

The characteristic sound speed $c_{\text{ch}}^{\text{II}}$ resulting from Eq.(43) is a monotonically increasing function of φ at any distance

x and is a monotonically decreasing function of x at any φ . This is understood by taking the partial differences of both sides of Eq.(43) with respect to φ and x ,

$$\begin{aligned} \left(\frac{\partial u}{\partial \varphi} \right)_x &= \frac{u}{\varphi} \left[\frac{1}{2} + \left(\frac{\varphi}{\varepsilon x u} - 1 \right)^{-1} \right] \\ &\quad \times \left[\frac{2u^2}{u^2 - \varepsilon} + \beta + 1 + \left(\frac{\varphi}{\varepsilon x u} - 1 \right)^{-1} \right]^{-1} \quad (> 0) \\ \left(\frac{\partial u}{\partial x} \right)_\varphi &= -\frac{u}{x} \left[\frac{1}{2} + \left(\frac{\varphi}{\varepsilon x u} - 1 \right)^{-1} \right] \\ &\quad \times \left[\frac{2u^2}{u^2 - \varepsilon} + \beta + 1 + \left(\frac{\varphi}{\varepsilon x u} - 1 \right)^{-1} \right]^{-1} \quad (< 0), \end{aligned}$$

where $u \equiv c_{\text{ch}}^{\text{II}}/c_{\text{eq}}$. This simply reflects that the heating timescale of Type II winds gets shorter as Φ_{EUV} increases and longer at large distances.

The Type II characteristic sound speed is a metric for the heating timescale to be compared with c_{eq} and v_g . Therefore, it is convenient to derive the equations, $\varphi = \varphi(x)$, at which $c_{\text{ch}}^{\text{II}}$ equals to c_{eq} and v_g . Since $c_{\text{ch}}^{\text{II}}$ derived by Eq.(43) is a monotonically increasing function of φ at any distance, there is a unique φ at which $c_{\text{ch}}^{\text{II}} = c_{\text{eq}}$ at any x . Substituting $c_{\text{ch}}^{\text{II}} = c_{\text{eq}}$ into Eq.(43), such φ is derived as

$$\varphi = f_{\text{eq}}(\varepsilon, q)x,$$

where

$$f_{\text{eq}}(\varepsilon, q) \equiv \frac{4\varepsilon q}{\left(\sqrt{(\varepsilon^{-1} - 1)^2 + 4q} - (\varepsilon^{-1} - 1) \right)^2}$$

Hence, the rapid heating condition, $c_{\text{ch}}^{\text{II}} > c_{\text{eq}}$, reduces to $\varphi > f_{\text{eq}}x$. The factor f_{eq} is equal to unity when $\varepsilon = 1$ or $\varepsilon q = 1$, and the range of f_{eq} is tabulated in Table 4 for other (ε, q) . For the H-class, the Type II regime $\varphi > \max(1, q)\varepsilon x$

| Parameter space | Class | Range of f_{eq} |
|--|--------|--|
| $\{(\varepsilon, q) \mid \varepsilon q > 1, \varepsilon > 1\}$ | H | $1 < f_{\text{eq}} < \min(\varepsilon, \varepsilon q)$ |
| $\{(\varepsilon, q) \mid \varepsilon q > 1, \varepsilon < 1\}$ | H | $\varepsilon < f_{\text{eq}} < 1$ |
| $\{(\varepsilon, q) \mid \varepsilon q < 1, \varepsilon > 1\}$ | H | $\varepsilon q < f_{\text{eq}} < 1$ |
| $\{(\varepsilon, q) \mid \varepsilon q < 1, \varepsilon < 1\}$ | Sa, Sr | $f_{\text{eq}} > 1$ |

Table 4. Possible values of f_{eq} taken in the parameter spaces, and the corresponding spectrum classes.

always satisfies $\varphi > f_{\text{eq}}x$, indicating that Type II winds are always isothermal in the H-class. For the Sa- and Sr-classes, Type II winds are not necessarily isothermal and can even be gravity-inhibited. This is because the soft spectrum has a relatively small energy deposition per photoionization, and a large Φ_{EUV} is needed to increase photoionization to heat the

gas to $c_s = c_{\text{eq}}$. We will discuss these points in more detail in §4.5.

Similarly, there is a unique φ at which $c_{\text{ch}}^{\text{II}} = v_g$. Substituting $c_{\text{ch}}^{\text{II}} = v_g$ into Eq.(43) reduces to

$$\left(\frac{\varphi q x^\beta}{\varepsilon} \right)^{1/2} = x^{-1} \varepsilon^{-1} - 1 + \left(\frac{\varepsilon q x^{1+\beta}}{\varphi} \right)^{1/2}. \quad (47)$$

Note that the LHS is $R/v_g t_{\text{rec}}$ with $c_s = v_g$. Solving this equation with respect to φ gives the functional form of

$$\varphi = \varphi_g(x; \varepsilon, q, \beta) \\ \equiv \left(\frac{2\sqrt{q}\varepsilon x^{(\beta+1)/2}}{\sqrt{(x^{-1}\varepsilon^{-1} - 1)^2 + 4qx^{(2\beta+1)/2}} - (x^{-1}\varepsilon^{-1} - 1)} \right)^2, \quad (48)$$

at which $c_{\text{ch}}^{\text{II}}$ equals to v_g . This function has the intersections with $\varphi = x^{-1/2}$ at $x = \varepsilon^{-1}$ and $x = (\varepsilon q)^{-2/(3+2\beta)}$ and asymptotically approaches $\varphi = \varepsilon x^{1/2}$ for $x \gg \varepsilon^{-1}$. It also connects to $f_{\text{eq}}x$ at $x = 1$, which motivates us to define the secondary critical EUV emission rate as

$$\Phi_c^{\text{II}} \equiv f_{\text{eq}} \Phi_c \\ = \frac{4\varepsilon q}{\left(\sqrt{(\varepsilon^{-1} - 1)^2 + 4q} - (\varepsilon^{-1} - 1) \right)^2} \Phi_c, \quad (49)$$

Above this critical EUV emission rate, ionized winds can be isothermal at $x = 1$. However, since Type II winds in the H-class are guaranteed isothermal, the secondary critical EUV emission rate is physically meaningful only for the Sa and Sr classes.

The root of the implicit equation, Eq.(43), can be explicitly expressed by simple forms in some special cases. When the additional energy injection by reionization is negligible due to slow recombination, i.e.,

$$\left(\frac{c_{\text{ch}}^{\text{II}}}{c_{\text{eq}}} \right)^{\beta+1} \gg \left(\frac{\varphi q}{x\varepsilon} \right)^{1/2}, \quad (50)$$

(cf. Eq.(27)), the total energy gain during the gas traveling to the height of $\sim R$ is primarily covered by the initially injected energy. In this case, we can drop the second term on the RHS of Eq.(43) to obtain a zeroth-order root as

$$c_{\text{ch}}^{\text{II}} \approx c_1 = \varepsilon^{1/2} c_{\text{eq}}. \quad (51)$$

Substituting this root back into Eq.(50), we get

$$\varphi \ll \varepsilon^{\beta+2} q^{-1} x, \quad (52)$$

a sufficient condition where Eq.(51) is available.

On the other hand, when recombination is fast enough so that the additionally deposited energy dominates over the initially deposited energy, i.e.,

$$\left(\frac{c_{\text{ch}}^{\text{II}}}{c_{\text{eq}}} \right)^{\beta+1} \ll \left(\frac{\varphi q}{x\varepsilon} \right)^{1/2}, \quad (53)$$

we can neglect the first term of the RHS in Eq.(44). Then, the zeroth order $c_{\text{ch}}^{\text{II}}$ is derived as

$$\left(\frac{c_{\text{ch}}^{\text{II}}}{c_{\text{eq}}} \right) \approx \left(\frac{\varphi_{\text{II}}}{x} \right)^{1/2(\beta+3)},$$

where

$$\varphi_{\text{II}} \equiv \frac{\Phi_{\text{EUV}}}{\Phi_{c,\text{rec}}^{\text{II}}} \\ \Phi_{c,\text{rec}}^{\text{II}} \equiv \frac{\Phi_c}{\varepsilon q}.$$

The normalization factor $\Phi_{c,\text{rec}}^{\text{II}}$ is the secondary critical EUV emission rate for recombination-dominated Type II winds. Here we have retrieved the Type II characteristic sound speed (Eq.(19))

$$c_2 \equiv c_{\text{eq}} \left(\frac{\varphi_{\text{II}}}{x} \right)^{1/2(\beta+3)}.$$

Substituting c_2 into Eq.(53), we obtain a sufficient condition under which the above approximate root is available:

$$\varphi \gg \varepsilon^{\beta+2} q^{-1} x, \quad (54)$$

which is opposite to Eq.(52).

In the following subsections, we will evaluate the sound speeds and corresponding parameter spaces in the Type II regime for each class using $c_{\text{ch}}^{\text{II}}$.

4.5. Type II Winds

As mentioned in §4.4, the remaining parameter space uncovered by the Type I regime (the area covered by gray vertical lines in Figure 7) is the Type II regime. The condition of the Type II regime is expressed by the fast ionization condition (Eq.(14)),

$$t_{\text{ioni}} < \min \left(t_{\text{rec}}, \frac{R}{\mathcal{M} c_s} \right).$$

Similarly to the Type I regime, it can equivalently be broken down into the following three conditions:

Condition II-1: $c_{\text{ch}}^{\text{II}} > c_{\text{eq}} \cap t_{\text{ioni}} < \min [t_{\text{rec}}(c_s = c_{\text{eq}}), R/c_{\text{eq}}]$

Condition II-2: $c_{\text{ch}}^{\text{II}} < v_g \cap t_{\text{ioni}} < \min [t_{\text{rec}}(c_s = v_g), R/\mathcal{M}_g^{\text{II}} v_g]$

Condition II-3: $v_g < c_{\text{ch}}^{\text{II}} < c_{\text{eq}} \cap t_{\text{ioni}} < \min [t_{\text{rec}}(c_s = c_{\text{ch}}^{\text{II}}), R/c_{\text{ch}}^{\text{II}}]$

Here, $\mathcal{M}_g^{\text{II}}$ is the typical Mach number for gravity-inhibited Type II winds, which we will derive the specific form later in this section.

In this section, we analyze the fast ionization condition for each class to derive the sound speed and typical flow speed for Type II winds and corresponding parameter spaces on the x - φ plane.

4.5.1. Type II winds in H-class

For the H class, it is trivial that $c_{\text{ch}}^{\text{II}}$ always exceeds c_{eq} from a physical point of view as follows. The Type I condition $t_{\text{ioni}} > \min(t_{\text{rec}}, R/\mathcal{M}c_s)$ indicates that on average, the launched gas reaches $s = R$ with a hydrogen atom being photoionized less than once. Such gas can still have a characteristic sound speed c_{ch}^{I} exceeding c_{eq} in this class. In the case where a launched hydrogen experiences photoionization at least once (Type II), the gas acquires more energy than the Type I case through recombination followed by reionization. Thus, the corresponding Type II characteristic sound speed must exceed c_{eq} . Hence, the sound speed and the typical flow speed in the ionized region of Type II flows are given by $c_s = c_{\text{eq}}$. One can also directly prove $c_{\text{ch}}^{\text{II}} > c_{\text{eq}}$ mathematically from Eq.(43) for $\varepsilon > 1$ or $\varepsilon q > 1$ (see Appendix B).

Since $c_{\text{ch}}^{\text{II}} > c_{\text{eq}}$, the parameter spaces satisfied by Conditions II-2 and II-3 are null, and thus the fast ionization condition is equivalent with $\varphi > \max(1, q)\varepsilon x$ for the H-class. It indicates that the Type II regime is always in Regime A (isothermal winds) for the H-class.

The fact of $c_{\text{ch}}^{\text{II}} > c_{\text{eq}}$ indicates that heating is always rapid enough to form isothermal winds in the Type II regime. As discussed in Sections 3.3 and 4.1, this parameter range has a shorter heating timescale than the gravitational timescale, and thus winds can escape without being influenced by gravity. The typical flow speed is thus given by $\sim c_{\text{eq}}$.

4.5.2. Type II winds in Sa-class

The Type II regime in the Sa-class is expressed by

$$\begin{cases} \varphi > \varepsilon q x^{1+\beta} & \text{for } 1 \leq x < \varepsilon^{-1} \\ \varphi > \varepsilon^{3/2} x & \text{for } x > \varepsilon^{-1} \end{cases} \quad (55)$$

(cf. Eq.(37)).

First, we consider Condition II-1. The fast ionization condition $t_{\text{ioni}} < \min[t_{\text{rec}}(c_s = c_{\text{eq}}), R/c_{\text{eq}}]$ is rewritten to $\varphi > \max(1, q)\varepsilon x = \varepsilon x$ in this class. One can confirm that the parameter space of $c_{\text{ch}}^{\text{II}} > c_{\text{eq}}$, or equivalently $\varphi > f_{\text{eq}}x$, is covered by the Type II regime, $\varphi > \varepsilon x$, in this class ($\varepsilon < 1$). Consequently, Condition II-1 reduces to $\varphi > f_{\text{eq}}x$.

Next, we consider Condition II-2. We first evaluate $\mathcal{M}_{\text{g}}^{\text{II}}$. To form escape winds in this gravity-inhibited regime, the gas must obtain energy to reach $c_s \sim v_{\text{g}}$ until traveling to a height of $\sim R$. Thus, the self-consistent condition is

$$\begin{aligned} c_p v_{\text{g}}^2 &\approx c_p c_1^2 + \frac{\bar{\sigma}_0 \bar{E}_0 \Phi_{\text{EUV}}}{4\pi m r^2} \frac{t_{\text{ioni}}}{t_{\text{rec}}} \frac{R - \mathcal{M}_{\text{g}}^{\text{II}} v_{\text{g}} t_{\text{ioni}}}{\mathcal{M}_{\text{g}}^{\text{II}} v_{\text{g}}} \\ &= c_p \varepsilon c_{\text{eq}}^2 \left(1 - \frac{t_{\text{ioni}}}{t_{\text{rec}}}\right) + c_p \varepsilon c_{\text{eq}}^2 \frac{R}{\mathcal{M}_{\text{g}}^{\text{II}} v_{\text{g}} t_{\text{rec}}} \end{aligned} \quad (56)$$

which reduces to

$$\frac{R}{\mathcal{M}_{\text{g}}^{\text{II}} v_{\text{g}} t_{\text{rec}}} \approx x^{-1} \varepsilon^{-1} - \left(1 - \frac{t_{\text{ioni}}}{t_{\text{rec}}}\right) = x^{-1} \varepsilon^{-1} - 1 + \left(\frac{\varepsilon q x^{1+\beta}}{\varphi}\right)^{1/2}$$

This ratio is larger than unity in the parameter space,

$$\left\{ (x, \varphi) \mid x < \frac{\varepsilon^{-1}}{2} \cup \left(\varphi < \frac{\varepsilon q x^{1+\beta}}{(2-x^{-1}\varepsilon^{-1})^2} \cap x > \frac{\varepsilon^{-1}}{2} \right) \right\}$$

and in this case, the rapid ionization condition in the gravity-inhibited regime, $t_{\text{ioni}} < \min[t_{\text{rec}}(c_s = v_{\text{g}}), R/\mathcal{M}_{\text{g}}^{\text{II}} v_{\text{g}}]$, is $t_{\text{ioni}} < t_{\text{rec}}$, i.e., $\varphi > \varepsilon q x^{\beta+1}$. This is always satisfied in the Type II gravity-inhibited regime. On the other hand, the above ratio is less than unity in

$$\left\{ (x, \varphi) \mid x > \frac{\varepsilon^{-1}}{2}, \varphi > \frac{\varepsilon q x^{1+\beta}}{(2-x^{-1}\varepsilon^{-1})^2} \right\}$$

and in this regime, the rapid ionization condition becomes

$$\frac{t_{\text{ioni}}}{t_{\text{rec}}} < x^{-1} \varepsilon^{-1} - \left(1 - \frac{t_{\text{ioni}}}{t_{\text{rec}}}\right),$$

or equivalently $x < \varepsilon^{-1}$. After all, the rapid ionization condition in the gravity-inhibited regime, $t_{\text{ioni}} < \min[t_{\text{rec}}(c_s = v_{\text{g}}), R/\mathcal{M}_{\text{g}}^{\text{II}} v_{\text{g}}]$, reduces to $x < \varepsilon^{-1}$.

The other condition in Condition II-2, $c_{\text{ch}}^{\text{II}} < v_{\text{g}}$, is equivalent with $\varphi < \varphi_{\text{g}}$ (see Eq.(48)). To summarize Condition II-2, the gravity-inhibited regime for Type II winds is defined by

$$\left\{ (x, \varphi) \mid x < \varepsilon^{-1}, \varphi > \varepsilon q x^{\beta+1}, \varphi < \varphi_{\text{g}} \right\}.$$

In this regime, winds have a sound speed of $\sim v_{\text{g}}$ and a Mach number of

$$\mathcal{M}_{\text{g}}^{\text{II}} \approx \left(\frac{\varphi q x^{\beta}}{\varepsilon}\right)^{1/2} \left[x^{-1} \varepsilon^{-1} - 1 + \left(\frac{\varepsilon q x^{\beta+1}}{\varphi}\right)^{1/2} \right]^{-1} \quad (57)$$

Mach number increases with φ at individual distance owing to increasing heating with φ and approaches unity at the $c_{\text{ch}}^{\text{II}} = v_{\text{g}}$ boundary (see Eq.(47)).

Finally, we evaluate Condition II-3. This condition clearly corresponds to the remaining parameter space that is not covered by Conditions II-1 and II-2, that is,

$$\left\{ (x, \varphi) \mid \varphi < f_{\text{eq}}x, \varphi > \varphi_{\text{g}}, \varphi > \varepsilon^{3/2}x \right\}.$$

In this space, the heating timescale is shorter than the gravitational timescale for Type II winds but is not short enough to heat the gas to the equilibrium temperature until traveling to the height of $\sim R$. Therefore, $c_s \sim c_{\text{ch}}^{\text{II}}$ and $\mathcal{M} \sim 1$ in this regime.

The sound speed in this regime is obtained by solving the implicit equation Eq.(43) with respect to $c_{\text{ch}}^{\text{II}}/c_{\text{eq}}$. The expression of the root would have a complex functional form with arguments of ε , $\varphi \varepsilon q/x$, and $\varphi/\varepsilon x$, which might be unpractical to be presented. Instead, it would be convenient to

show approximate forms of the root here. In the Sa-class, the parameter space where $c_s = c_{\text{ch}}^{\text{II}}$ always contains the slow recombination regime Eq.(52). This is because in this class, the second term on the RHS of Eq.(43) is exactly zero at the Type I and Type II boundary ($\varphi = \varepsilon^{3/2}x$), and Eq.(52) always exists within the Type II regime. The approximated $c_{\text{ch}}^{\text{II}}$ is

$$c_{\text{ch}}^{\text{II}} \approx c_1 = \varepsilon^{1/2} c_{\text{eq}}.$$

This approximation holds in the parameter space of

$$\{(x, \varphi) \mid x > \varepsilon^{-1}, \varphi \ll \varepsilon^{\beta+2} q^{-1} x, \varphi > \varepsilon^{3/2} x\}.$$

Here, the condition $x > \varepsilon^{-1}$ originates from a requirement for winds to be escaping, $c_{\text{ch}}^{\text{II}} > v_g$. The corresponding area is illustrated by the orange-shading bounded by the red and blue dashed lines in the top right panel in Figure 7, as an example. Having this area where the additionally deposited energy through reionizations is negligible is a unique characteristic of the Sa-class. Note that in $x < \varepsilon^{-1}$, gravity is so strong that the additional energy deposition through reionizations is always needed to form steadily escaping winds.

In this class, the fast recombination regime (Eq.(54)) is not necessarily contained in the free wind regime where $c_s = c_{\text{ch}}^{\text{II}}$. This is physically understood as follows. Suppose the case where ε has a value slightly smaller than unity, $c_{\text{ch}}^{\text{II}}$ needs only a small contribution from the additionally supplied energy through reionizations (the second term on the RHS of (43)) to reach $c_{\text{ch}}^{\text{II}} > c_{\text{eq}}$. Hence, in this class, it is possible that the fast recombination regime is not present in Regime B-II (the free Type II winds), and the slow recombination regime (Eq.(52)) directly connects to the boundary between Regime A (isothermal winds) and Regime B-II (free winds), at which $c_{\text{ch}}^{\text{II}} = c_{\text{eq}}$.

The resulting parameter space for the Sa-class is summarized by the top right panel of Figure 7.

4.5.3. Type II winds in Sr-class

The Type II regime of the Sr-class is expressed by

$$\begin{cases} \varphi > \varepsilon q x^{1+\beta} & \text{for } 1 \leq x < (\varepsilon q)^{-2/(3+2\beta)} \\ \varphi > (\varepsilon q)^{3/(3+2\beta)} x & \text{for } x > (\varepsilon q)^{-2/(3+2\beta)} \end{cases} \quad (58)$$

(cf. Eq.(38)). The fast ionization condition for Condition II-1 is $\varphi > \max(1, q)\varepsilon x$ in this class. Since $f_{\text{eq}} > 1$ for the soft-spectrum classes, the Type II regime meets the fast-heating condition, $\varphi > f_{\text{eq}} x$. Therefore, Condition II-1 is equivalent with $\varphi > f_{\text{eq}} x$ for the same reason as in the Sa-class.

Regarding Condition II-2, we do a similar analysis to that we have done for Type II winds in the Sa-class. The condition $c_{\text{ch}}^{\text{II}} < v_g$ is again $\varphi < \varphi_g$ (Eq.(48)), and φ_g connects to the intersection between $\varphi = \varepsilon q x^{1+\beta}$ and $\varphi = (\varepsilon q)^{3/(3+2\beta)} x$ at $x = (\varepsilon q)^{-2/(3+2\beta)}$ (see Eq.(58)). Therefore, the gravity-inhibited

regime for Type II winds is defined by

$$\{(x, \varphi) \mid x < (\varepsilon q)^{-2/(3+2\beta)}, \varphi < \varphi_g, \varphi > \varepsilon q x^{1+\beta}\}.$$

In this regime, $c_s \sim v_g$ and $\mathcal{M} = \mathcal{M}_g$ (Eq.(57)).

The other parameter space corresponds to the regime of free Type II winds, and Condition II-3 reduces to

$$\{(x, \varphi) \mid \varphi > (\varepsilon q)^{3/(3+2\beta)} x, \varphi > \varphi_g, \varphi < f_{\text{eq}} x\}.$$

The typical sound speed and Mach number are $c_s \sim c_{\text{ch}}^{\text{II}}$ and $\mathcal{M} \sim 1$, respectively.

We can derive an approximate form of $c_{\text{ch}}^{\text{II}}$ for this class instead of deriving the exact root from the implicit equation (43). In contrast to the Sa-class, the Sr-class does not cover the slow recombination regime, as Eq.(52) is outside of the Type II regime (Eq.(58)). This means additional deposited energy always contributes to the heating for Type II winds in this class. Hence, $c_{\text{ch}}^{\text{II}}$ can be approximated to Eq.(19),

$$c_{\text{ch}}^{\text{II}} \sim c_2 = c_{\text{eq}} \left(\frac{\varphi_{\text{II}}}{x} \right)^{1/2(\beta+3)}$$

in the parameter space,

$$\{(x, \varphi) \mid \varphi_{\text{II}} < x, \varphi > (\varepsilon q)^{3/(3+2\beta)} x, \varphi_{\text{II}} > x^{-(\beta+2)}\}$$

This parameter space is represented by the area bounded by the gray solid and green dashed lines in Figure 7. One can observe that the gray line gives approximate boundaries with the gravity-inhibited and isothermal wind regimes. For reference, we also plot this boundary in the Sa-class map of Figure 7. The gray line does not necessarily give approximate boundaries with the gravity-inhibited and isothermal wind regimes, since neglecting the contribution of the initially injected energy to heating is not always justified in the Sa-class.

5. COMPARISON WITH HYDRODYNAMICS SIMULATIONS

To assess the predictability of our phenomenological model and the validity of the adopted assumptions, we briefly compare the analytic model with hydrodynamics simulations, where ray-tracing EUV radiative transfer and nonequilibrium thermochemistry are self-consistently treated. We stress that self-consistent coupling between hydrodynamics and thermochemistry is required to make meaningful comparisons. We provide the computational methods of the simulations in §5.1 and compare the resulting disk structures with the analytical predictions of the model in §5.2.

5.1. Computational Methods

For the methodology, we largely follow Nakatani et al. (2018a,b). Here, we provide a brief overview of the methods

employed, referring interested readers to the original papers for more comprehensive details on the computational techniques.

In our simulations, we start with an initially hydrostatic disk (in the poloidal directions) that is exposed to EUV radiation from a central source. The disk is assumed to be both axisymmetric and midplane symmetric, with an initially isothermal temperature profile in the vertical direction.

The initial density distribution of the hydrostatic disk is

$$n_{\text{H}} = n_{\text{m}}(R) \exp \left[-\frac{z^2}{2h^2} \right],$$

where $n_{\text{m}}(R)$ represents the number density at the midplane ($z = 0$), and h denotes the pressure scale height defined as the ratio of c_s to the orbital frequency $\Omega \equiv \sqrt{GM_*/R^3}$.

The midplane density is determined by specifying the initial surface density profile Σ , given by

$$\Sigma = \Sigma_0 \left(\frac{R}{R_0} \right)^{-1} \quad (59)$$

with R_0 and Σ_0 being a reference radius and surface density at R_0 , respectively. The product of Σ_0 and R_0 is determined by the total disk mass

$$M_{\text{disk}} = \int_{R_{\text{min}}}^{R_{\text{max}}} 2\pi R \Sigma dR = 2\pi(R_{\text{max}} - R_{\text{min}})R_0 \Sigma_0, \quad (60)$$

where R_{min} and R_{max} are the inner and outer truncated radii, respectively, set to the same values as the inner and outer computational boundaries, which will be described below.

The initial temperature profile is given by

$$T = 100 \text{ K} \left(\frac{R}{1 \text{ au}} \right)^{-1/2}.$$

This profile is selected based on our previous simulations. While the choice of this profile may alter the base's geometry, it does not notably influence the comparisons conducted in this section. The initial value is immediately adjusted to account for the local thermochemical processes within the wind region and remains nearly constant in the stable disk region.

The simulations are performed in 2D spherical polar coordinates (r, θ) . We solve the time evolution of gas density ρ , velocities $\vec{v} = (v_r, v_\theta, v_\phi)$, total gas energy density, and chemical abundances, using a modified version of PLUTO

(Mignone et al. 2007):

$$\frac{\partial \rho}{\partial t} + \nabla \cdot (\rho \vec{v}) = 0, \quad (61)$$

$$\frac{\partial \rho v_r}{\partial t} + \nabla \cdot (\rho v_r \vec{v}) = -\frac{\partial p}{\partial r} - \rho \frac{GM_*}{r^2} + \rho \frac{v_\theta^2 + v_\phi^2}{r}, \quad (62)$$

$$\frac{\partial \rho v_\theta}{\partial t} + \nabla \cdot (\rho v_\theta \vec{v}) = -\frac{1}{r} \frac{\partial p}{\partial \theta} - \rho \frac{v_\theta v_r}{r} + \frac{\rho v_\phi^2}{r} \cot \theta, \quad (63)$$

$$\frac{\partial \rho v_\phi}{\partial t} + \nabla^l \cdot (\rho v_\phi \vec{v}) = 0, \quad (64)$$

$$\frac{\partial E}{\partial t} + \nabla \cdot (H \vec{v}) = -\rho v_r \frac{GM_*}{r^2} + \rho (\Gamma_{\text{EUV}} - \Lambda), \quad (65)$$

$$\frac{\partial n_{\text{H}} y_{\text{HI}}}{\partial t} + \nabla \cdot (n_{\text{H}} y_{\text{HI}} \vec{v}) = -n_{\text{H}} y_{\text{HI}} k_{\text{ioni}} + \alpha n_{\text{H}}^2 y_{\text{e}} y_{\text{HI}}, \quad (66)$$

$$\frac{\partial n_{\text{H}} y_{\text{HII}}}{\partial t} + \nabla \cdot (n_{\text{H}} y_{\text{HII}} \vec{v}) = n_{\text{H}} y_{\text{HI}} k_{\text{ioni}} - \alpha n_{\text{H}}^2 y_{\text{e}} y_{\text{HII}} \quad (67)$$

$$\text{and } \frac{\partial n_{\text{H}} y_{\text{e}}}{\partial t} + \nabla \cdot (n_{\text{H}} y_{\text{e}} \vec{v}) = n_{\text{H}} y_{\text{HI}} k_{\text{ioni}} - \alpha n_{\text{H}}^2 y_{\text{e}} y_{\text{HII}}. \quad (68)$$

Eq.(64) is written in the angular momentum conserving form. Here p denotes the gas pressure; and y_{HI} and y_{e} are the chemical abundances of H^+ and e^- , respectively; and Λ is the total cooling rate per unit mass (specific cooling rate). We incorporate radiative recombination cooling and $\text{Ly}\alpha$ cooling in the present study. The total gas energy density and enthalpy density are defined as

$$E = \frac{1}{2} \rho v^2 + \frac{p}{\gamma - 1}$$

$$H = E + p,$$

respectively, with γ being the specific heat ratio ($\gamma = 5/3$) and the ideal equation of state. We use $M_{\text{disk}} = 0.01 M_\odot$ and $M_* = 1.0 M_\odot$ throughout our simulations.

We run four models varying the EUV spectral hardness and Φ_{EUV} , covering high- and low- Φ_{EUV} ranges for both soft and hard spectra. We employ δ -function spectra of the form $\delta(h\nu - h\nu_0)$, where $h\nu_0$ is the EUV photon energy. In the soft-spectrum runs, $h\nu_0 = 14.6 \text{ eV}$, while in the hard-spectrum runs, $h\nu_0 = 72.9 \text{ eV}$. For the soft-spectrum runs, $h\nu_0 = 14.6 \text{ eV}$, which corresponds to the average energy of a blackbody spectrum with $T_{\text{eff}} = 10^4 \text{ K}$ above the Lyman limit. For the hard-spectrum runs, we chose $h\nu_0 = 72.9 \text{ eV}$ arbitrarily for experimental purposes, corresponding to the average energy of a blackbody spectrum with $T_{\text{eff}} = 3 \times 10^5 \text{ K}$. We explore two orders of magnitude in the dimension of the EUV luminosity: $L_{\text{EUV}} = 10^{28} \text{ erg s}^{-1}$ and $10^{30} \text{ erg s}^{-1}$ for the low- and high-luminosity cases, respectively. The corresponding Φ_{EUV} is determined by $L_{\text{EUV}} = h\nu_0 \Phi_{\text{EUV}}$. A summary of the input EUV parameters is provided in Table 5. The Model labels reflect both the magnitude of L_{EUV} (high: H, low:L) and spectral hardness (soft: S, hard: H). The EUV emission rate Φ_{EUV} of Model HS is the closest to the supposedly typical value for pre-main-sequence low-mass stars

| Model | Emission Rate Φ_{40} | Photon Energy (eV) | Luminosity L_{30} |
|-------|---------------------------|--------------------|---------------------|
| HS | 4.3 | 14.6 | 1.0 |
| HH | 0.86 | 72.9 | 1.0 |
| LS | 4.3×10^{-2} | 14.6 | 0.01 |
| LH | 0.86×10^{-2} | 72.9 | 0.01 |

Table 5. EUV parameters for each run. Here, $\Phi_{40} \equiv \Phi_{\text{EUV}}/10^{40} \text{ s}^{-1}$ and $L_{30} \equiv L_{\text{EUV}}/10^{30} \text{ erg s}^{-1}$. In the model labels, the first letter indicates either high (H) or low (L) luminosity, while the second letter signifies either soft (S) or hard (H) spectrum.

($\Phi_{\text{EUV}} \approx 10^{40}\text{--}10^{41} \text{ s}^{-1}$; e.g., Alexander et al. 2014), a value commonly adopted in the literature. We have also performed runs with luminosities ten times higher than Models HS and HH. However, these models produced qualitatively similar structures to those in Models HS and HH, as we will discuss in §5.2.

Our computational domain spans $r = [0.1, 20] \times R_g (= [R_{\min}, R_{\max}])$ and $\theta = [0, \pi/2] \text{ rad}$ with a resolution of $N_r \times N_\theta = 256 \times 160$ cells. The grid is spaced logarithmically in the radial direction, whereas in the polar direction, two different resolutions are employed. The domain is divided into two regions at $\theta = 1 \text{ rad}$, with each region having 80 cells uniformly spaced. We have arrived at this grid resolution after conducting a convergence check for Models HS and LH. Changing $N_r \times N_\theta$ to 128×160 and 512×320 , respectively, have yielded overall similar structures.

5.2. Comparisons with the Phenomenological Model

Figures 8, 9, 10, and 11 show snapshots of the simulations (panels a–d) along with comparisons with analytical predictions by our phenomenological model (panels e–k) for Models HS, HH, LS, and LH, respectively. In these figures, we use the data from the gas structure when it has reached a nearly quasi-steady state. However, in Model HS, we employ time-averaged data to smooth out small fluctuations observed in the vicinity of the ionization front. In the phase diagram located at the lower-right corner of each figure, a black horizontal bar represents the spatial range displayed by panels (a)–(k) for each model.

These figures directly illustrate the wide variety in the structures of n_{H} , T , and y_{HI} , depending on Φ_{EUV} and the spectral hardness, even when they share a common total input energy L_{EUV} . Temperatures and isothermal sound speeds (panels b and c) reach the equilibrium values ($T \approx 10^4 \text{ K}$ and $c_s \approx 10 \text{ km s}^{-1}$) only at relatively small R , indicating where the canonical picture of EUV photoevaporation applies. Temperatures overall decrease at larger distances due to relatively long heating timescales.

Comparing Models HS and HH, one can observe that H-class spectra tend to result in a larger volume of the high-temperature region, even though φ decreases with spectral

hardness. This reflects the fact that a larger fraction of the photon energy is consumed for photoionization with soft spectra. To heat the gas to high temperatures, soft spectra require multiple energy depositions through reionizations. However, this process is inefficient compared to energy deposition to an atomic gas.

Panels (e) and (f) demonstrate that our analytic model effectively captures the radial-dependent trend of c_s (and consequently T) over a wide range of distances. In fact, the whitish region in panel (g), where c_s^2 in the simulation is within the factor of two difference from c_s^2 predicted by the analytic model, covers a much broader region than the whitish region of panel (h), which shows the ratio of c_s^2 in the simulation to the equilibrium value c_{eq}^2 . This indicates that our model significantly improves the analytical prediction of c_s compared to simply assuming $c_s = c_{\text{eq}}$ as in the canonical picture. This improvement holds true for a broad range of Φ_{EUV} and the spectral hardness, as observed when comparing panels (e) and (f) of Figures 8, 9, 10, and 11. The enhancement is more noticeable as the wind temperature decreases with lower L_{EUV} .

Our phenomenological model also adeptly captures the ionization structures. In panels (d), (i), and (j), the greenish region represents the H II region for each run, with its size varying significantly depending on Φ_{EUV} and the spectral hardness (as evident by comparing the four models), as well as the radial distance to the source (as seen in panels (i) and (j) in Figure 10). As indicated by the analytical model, a harder spectrum tends to result in atomic winds even when Φ_{EUV} is at the same levels. This is implied by comparing, for instance, Figures 9 and 10; the soft-spectrum run (Model LS) shows a much more extended H II region despite having ~ 20 times smaller Φ_{EUV} .

Panels (i) and (j) show that our analytic model predicts the radial extension of the H II region and wind types across a broad range of Φ_{EUV} and the spectral hardness with reasonable accuracy. Contrary to the canonical model, where the EUV-heated gas is typically assumed to be completely photoionized ($y_{\text{HI}} \ll 1$) regardless of the distance to the radiation source and Φ_{EUV} , our numerical and analytic models highlight the necessity of incorporating the finite timescale of photoionization to discuss the ionization structure, especially for low-mass stars.

In panel (k), we also compare the Mach number in the simulation, \mathcal{M}^{sim} , with the prediction from our phenomenological model, \mathcal{M}^{ana} . Despite some deviations, there is generally a close agreement between the simulation and the analytic estimate, even in the gravity-inhibited subsonic regions (Regime C) of Model LH (see Figure 11), capturing an overall radial-dependent trend in \mathcal{M} . This suggests that our model provides a better estimate for \mathcal{M} across a wider

$L_{30} = 1$, $\Phi_{40} = 4.3$, δ -function spectrum $\delta(h\nu - 15 \text{ eV})$; Sa-class, $\varepsilon = 0.27$, $q = 0.018$, $\varphi = 177$

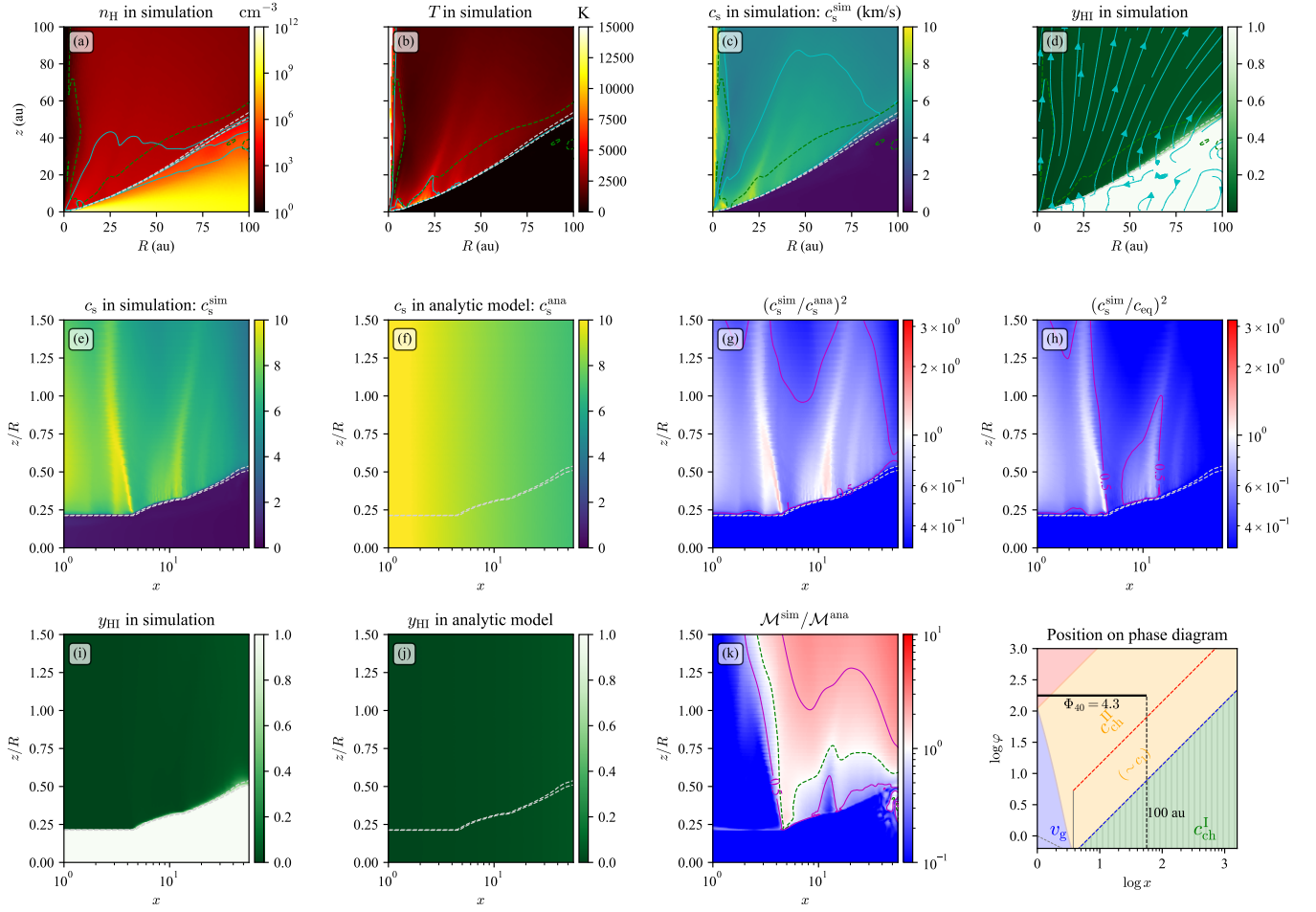


Figure 8. Snapshots of Model HS, showcasing various physical quantities: (a–d) number density, gas temperature, isothermal sound speed, and H I abundance from left to right, respectively. The green dashed contour represents the isothermal sonic surface, while the light-gray dashed contours indicate where EUV flux is absorption-attenuated by half and 90% from the original value, i.e., $\chi_e = \chi_i = 0.5$ and 0.1 , respectively. These contours roughly demarcate the wind region from the steady disk region. In panel (a), cyan contours represent $n_{\text{H}} = 10^3, 10^4, 10^5, 10^6 \text{ cm}^{-3}$; in panel (b), $T = 1000, 5000 \text{ K}$; and in panel (c), $c_s = 5 \text{ km s}^{-1}$. Streamlines are depicted in panel (d). Panels (e) and (i) offer the same snapshots for c_s and y_{HI} , respectively, but in the x - z/R coordinates for comparison with the analytically estimated values through the phenomenological model, presented in panels (f) and (j). Panel (g) illustrates the difference between c_s in the simulation and that predicted by the model, with the magenta contours representing where the analytic estimate falls within a factor of two from c_s in the simulation. The whitish region indicates where the analytic model accurately predicts c_s (and thereby T) of the simulation. For comparison with the canonical picture, where $c_s = c_{\text{eq}}$ is assumed, panel (h) similarly displays the difference between c_s in the simulation and c_{eq} . A comparison between panels (g) and (h) reveals that our phenomenological model improves the analytical predictions of temperature structures. The light-gray dashed contours in panels (e)–(j) also show where $\chi_e = 0.1$ and 0.5 , consistent with panels (a)–(d). Panel (k) presents the difference between the Mach number in the simulation to that predicted through the phenomenological model, with the green dashed contour again representing the isothermal sonic surface. Lastly, the phase diagram for the spectrum of Model HS is shown by the lower-right corner panel, with a black horizontal bar indicates the location of this model on the phase diagram within the range displayed by panels (a)–(k), i.e., 100 au.

parameter space, compared to the classical assumption of $\mathcal{M} \sim 1$ everywhere beyond the critical radius.

Nonetheless, there is still room for improvement in estimating \mathcal{M} . Our model’s treatment of a constant \mathcal{M} fails to fully predict the accelerating nature of photoevaporative winds. Additionally, discrepancies arise where the ionization front becomes parallel to the radial direction (see, e.g., the

$x \lesssim 5$ region in panel (i) of Figure 8).² This parallel feature may be artificial, possibly influenced by the computational boundaries; however, it is also observed across convergence-check runs with higher- ($N_r \times N_\theta = 512 \times 320$) and lower-

² The radiation flux needs to have a perpendicular component to the base to launch winds (Nakatani & Takasao 2022).

$L_{30}=1$, $\Phi_{40}=0.86$, δ -function spectrum $\delta(h\nu - 73 \text{ eV})$; H-class, $\varepsilon=16$, $q=1.7$, $\varphi=23.8$

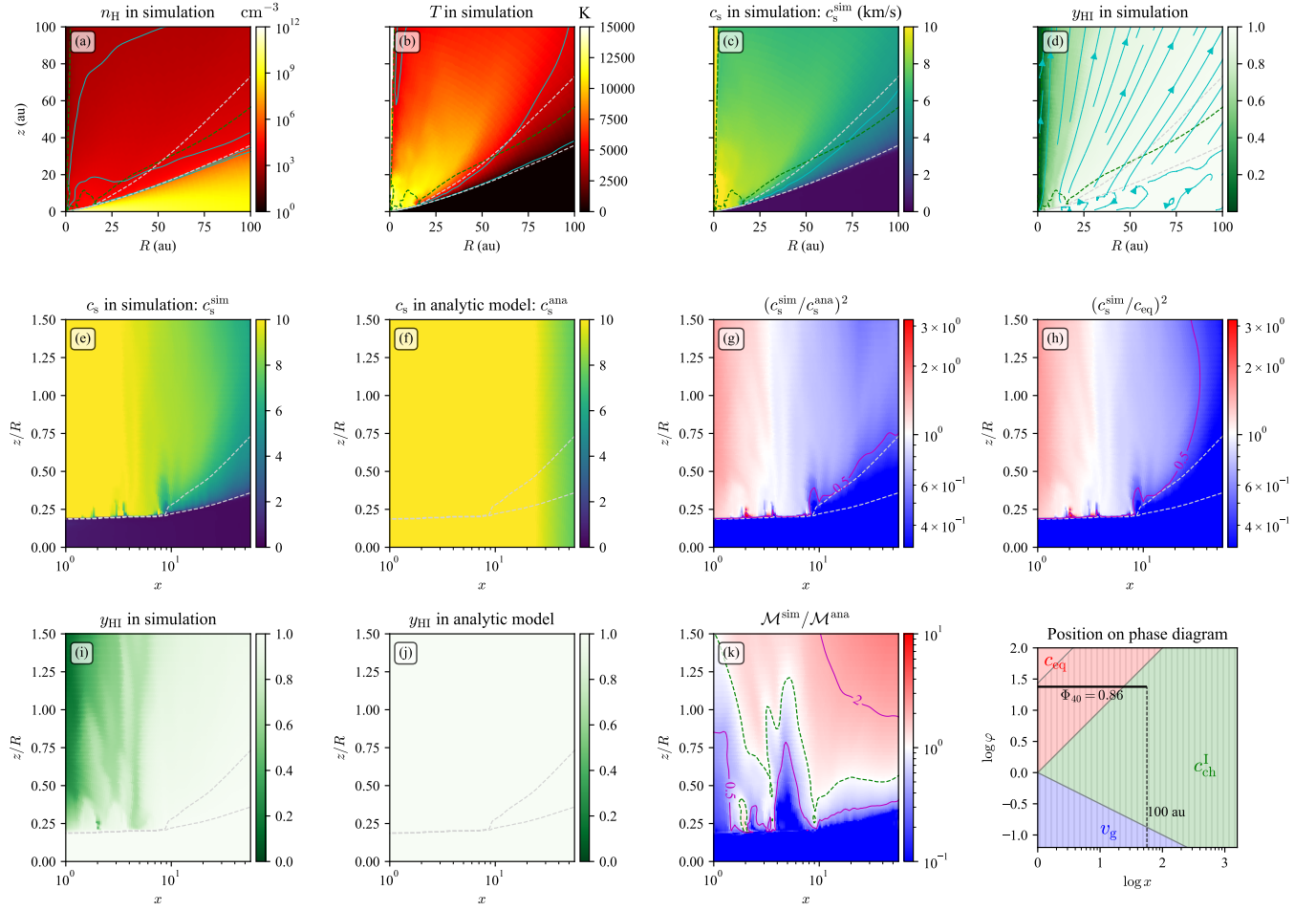


Figure 9. Same as Figure 8 but for Model HH.

resolutions ($N_r \times N_\theta = 128 \times 160$) for Model HS. Should the parallel structure persist consistently across various numerical grid configurations, it would suggest that the structure has physically developed by radiation-hydrodynamical effects, at least within the adopted problem setup. If this is the case, the parallel feature implies that diffuse EUV might dominate over direct EUV in heating the H I layer here, in contrast to the results of hydrostatic radiative transfer models (e.g., Tanaka et al. 2013). Further comparisons with carefully handled simulations are needed to examine numerical effects and explore the analytical predictability of \mathcal{M} in such regions, which we plan to address in future studies.

We have also conducted simulations with luminosities ten times higher ($L_{\text{EUV}} = 10^{31} \text{ erg s}^{-1}$) than Models HS and HH (corresponding Φ_{EUV} of $4.3 \times 10^{41} \text{ s}^{-1}$ and $0.86 \times 10^{41} \text{ s}^{-1}$, respectively). The resulting structures are qualitatively the same as those of Models HS and HH other than forming larger isothermal regions (Regime A winds). This outcome is expected based on the phase diagrams of Figures 8 and 9 (see the lower-bottom panels). The disks of Models HS and

HH extend across Regimes A and B, and increasing the luminosities does not alter this characteristic.

The mass-loss rates (within $R < 100 \text{ au}$) obtained from the simulations exhibit a wide variation: $2 \times 10^{-10} M_\odot \text{ yr}^{-1}$ for Model HS, $2 \times 10^{-9} M_\odot \text{ yr}^{-1}$ for Model HH, $1 \times 10^{-11} M_\odot \text{ yr}^{-1}$ for Model LS, and $2 \times 10^{-10} M_\odot \text{ yr}^{-1}$ for Model LH. These rates can vary significantly even when the same energy input rate L_{EUV} is applied. In general, models with soft spectra yield mass-loss rates approximately an order of magnitude smaller than those with hard spectra. This reflects the greater energy consumption by photoionization with soft spectra. While our current model is not specifically tailored for predicting mass-loss rates, it can be extended to cover this aspect. To that end, determining the appropriate base density for a wide range of Φ_{EUV} and spectral hardness is essential, a task we aim to tackle in future studies.

In summary, our comparisons here highlight a significant enhancement in analytical predictions for the physical structures across a wide range of Φ_{EUV} and spectral hardness. This signifies a broadened understanding of EUV-driven photoe-

$L_{30} = 0.01$, $\Phi_{40} = 0.043$, δ -function spectrum $\delta(h\nu - 15 \text{ eV})$; Sa-class, $\varepsilon = 0.27$, $q = 0.018$, $\varphi = 1.77$

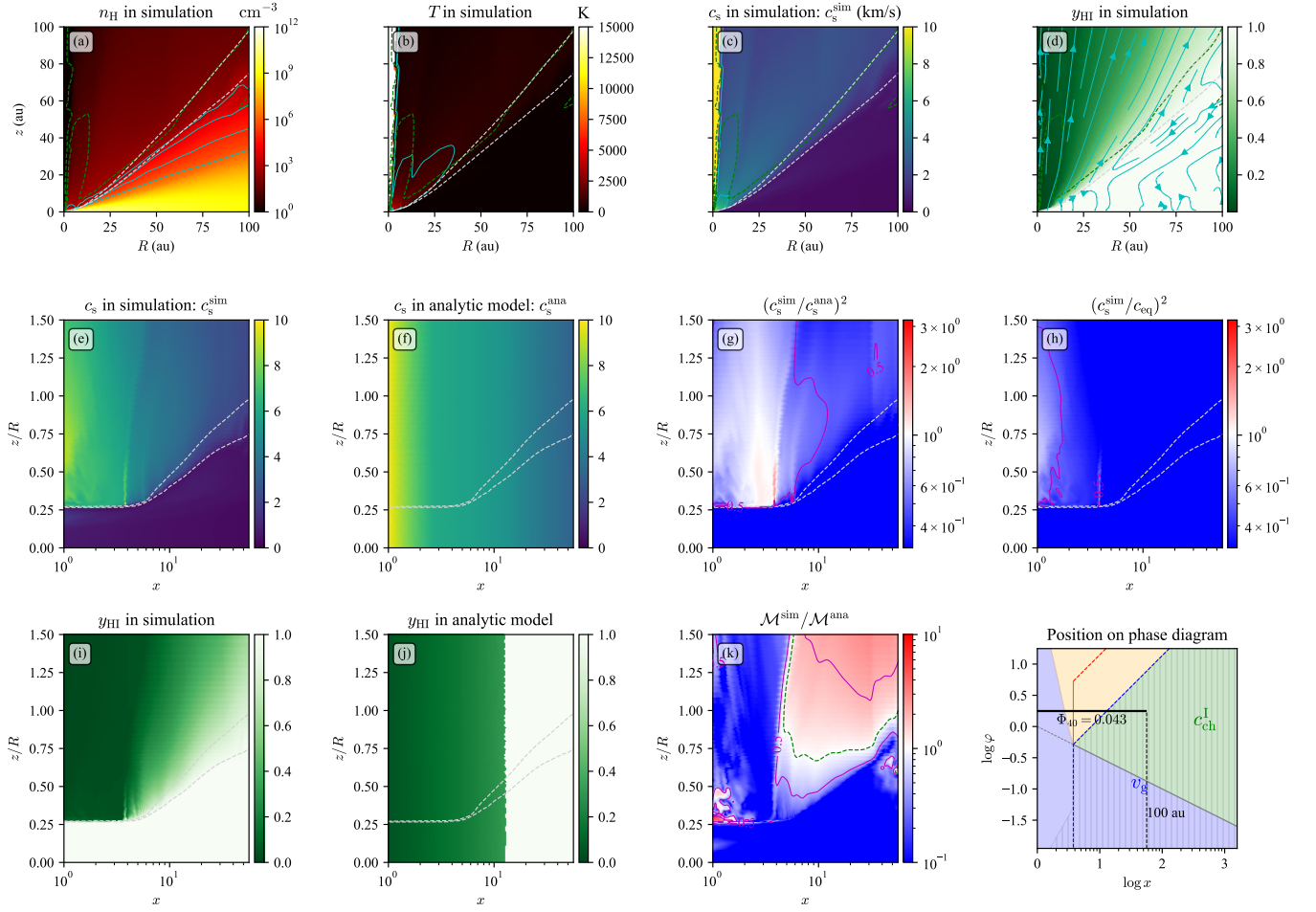


Figure 10. Same as Figure 10 but for Model LS.

vaporation for accretion disks through our phenomenological model. However, for robustness, similar comparisons over an even broader range of L_{EUV} , spectral hardness, and spectral shape are warranted, considering uncertainties in recombination timescales and assumptions regarding attenuation factors (χ_e and χ_i) in our model (see discussions in §8.4). These analyses would facilitate further model improvements and enhance its practical applications to general EUV spectra. While such more comprehensive comparisons are deferred to future studies, the brief comparisons provided here suffice to illustrate the remarkable generality of our model.

6. ON THE RADIAL EXTENSION OF THE H II REGION

Our model has shown that the canonical picture of EUV photoevaporation, where EUV photoheating drives isothermal ionized winds with temperature and velocity of $\sim 10^4 \text{ K}$ and $\sim 10 \text{ km s}^{-1}$, respectively, holds only in Regime A-II. The corresponding parameter space is formulated as $\varphi > \max(1, q)\varepsilon x$ for the hard-spectrum class and $\varphi > f_{\text{eq}}x$ for the soft-spectrum classes. For soft-spectrum classes, ion-

ized escaping winds are also feasible with lower temperatures (Regime B-II). These findings suggest the presence of a maximum radial distance up to which launched winds can be photoionized before reaching heights of $\sim R$. Beyond this distance, the photoionization timescale is longer than the recombination timescale or advection timescale. Consequently, hydrogen atoms remain only partially photoionized until they ascend to heights of $\sim R$ (cf. panels (d), (i), and (j) in Figure 10). On the scale beyond the maximum distance, the H II region appears vertically extended rather than radially. In this section, we quantify this distance limit in physical units and briefly discuss under which conditions the canonical picture of isothermal ionized winds remains valid.

We first consider the H-class. The boundary between Type I and Type II regimes is exclusively present within Regime A, meaning that the canonical picture is always applicable to ionized winds in this class. The distance limit to which the H II region extends is calculated from the Type II

$L_{30} = 0.01$, $\Phi_{40} = 0.0086$, δ -function spectrum $\delta(h\nu - 73 \text{ eV})$; H-class, $\varepsilon = 16$, $q = 1.7$, $\varphi = 0.238$

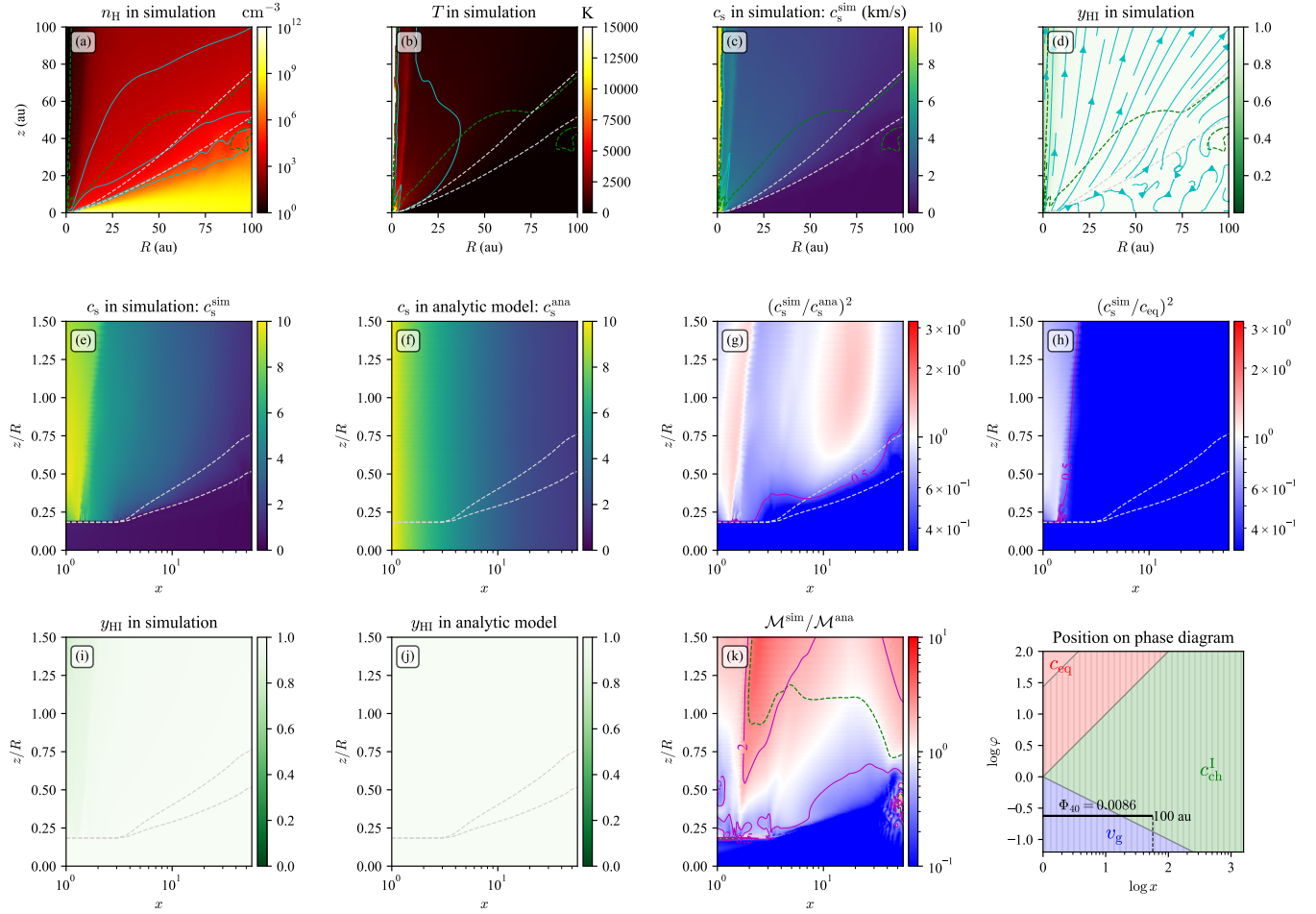


Figure 11. Same as Figure 11 but for Model LH.

condition (Eq.(21)) as

$$R_{\text{lim}} = R_c \frac{\varphi}{\max(1, q)\varepsilon} = \frac{\Phi_{\text{EUV}}}{\max(1, q)} \frac{\bar{\sigma}_0}{4\pi c_{\text{eq}}} \\ \approx 53 \text{ au} \left(\frac{\Phi_{\text{EUV}}}{10^{40} \text{ s}^{-1}} \right) \left(\frac{\bar{\sigma}_0}{10^{-18} \text{ cm}^2} \right) \\ \left(\frac{c_{\text{eq}}}{10 \text{ km s}^{-1}} \right)^{-1} \times \min(1, q^{-1}).$$

The nominal values for the parameters are chosen to be typical for T Tauri stars. This suggests that the canonical picture does not necessarily apply to disks around low-mass stars, but there are also atomic winds at the equilibrium temperature (Regime A-I) or lower (Regime B-I) for $R > R_{\text{lim}}$. For massive stars, whose Φ_{EUV} is several orders of magnitude higher than 10^{40} s^{-1} , assuming the canonical picture of an EUV-irradiated disk is justified. Since R_{lim} is essentially set by the ionization timescale, it is independent of the stellar gravity and is essentially set by Φ_{EUV} and the spectral hardness.

The distance limit for the Sa-class is derived similarly as

$$R_{\text{lim}} = R_c \frac{\varphi}{f_{\text{eq}}} = \frac{\left(\sqrt{(\varepsilon^{-1} - 1)^2 + 4q} - (\varepsilon^{-1} - 1) \right)^2}{4q} \frac{\Phi_{\text{EUV}} \bar{\sigma}_0}{4\pi c_{\text{eq}}}$$

When $(\varepsilon^{-1} - 1)^2 \gg 4q$, which is often the case for this class, R_{lim} is approximated to

$$R_{\text{lim}} \approx \frac{q}{(\varepsilon^{-1} - 1)^2} \frac{\Phi_{\text{EUV}} \bar{\sigma}_0}{4\pi c_{\text{eq}}} = \frac{1}{(\varepsilon^{-1} - 1)^2} \frac{3C^2 \Phi_{\text{EUV}} \alpha_{\text{eq}}}{4\pi c_{\text{eq}}^2}$$

In contrast to the H-class, this class has a regime where freely escaping ionized winds have temperatures lower than the equilibrium value (Regime B-II). This motivates us to define the distance limit for the extension of lower-temperature ionized escaping winds (cf. Eqs.(22), (37), or (55)),

$$R_{\text{lim}}^{\text{B}} = R_c \frac{\varphi}{\varepsilon^{3/2}} = \frac{1}{\varepsilon^{1/2}} \frac{\Phi_{\text{EUV}} \bar{\sigma}_0}{4\pi c_{\text{eq}}}.$$

Note that these distance limits are available when Φ_{EUV} exceeds the secondary critical EUV emission rate, i.e., $\varphi > f_{\text{eq}}$.

Hence, for Sa-class spectra, the canonical picture of EUV photoevaporation applies up to $R = R_{\text{lim}}$, and beyond that, ionized nonisothermal winds extend up to $R \leq R_{\text{lim}}^{\text{B}}$ (cf. panels (d), (i), and (j) in Figure 10).

The radius limit of isothermal ionized winds for the Sr-class is the same as that for the Sa-class. The secondary radius limit is derived as

$$R_{\text{lim}}^{\text{B}} = R_{\text{c}} \frac{\varphi}{(\varepsilon q)^{3/(3+2\beta)}} = \frac{\varepsilon}{(\varepsilon q)^{3/(3+2\beta)}} \frac{\Phi_{\text{EUV}} \bar{\sigma}_0}{4\pi c_{\text{eq}}}.$$

However, Sr-class might not be achieved with realistic EUV spectra, as mentioned in §3.7.

The presence of the two limiting distances for the soft-spectrum classes suggests the potential to constrain $\bar{\sigma}_0$ and \bar{E}_0 by spatially resolving the radial extensions of the isothermal (Regime A-II) and nonisothermal (Regime B-II) ionized winds:

$$\frac{\varepsilon^{1/2} q}{(\varepsilon^{-1} - 1)^2} \approx \frac{R_{\text{lim,obs}}}{R_{\text{lim,obs}}^{\text{B}}}.$$

This comparison allows for the potential constraint of Φ_{EUV} using the constrained spectrum parameters and observed radial extensions. Analyzing ionized wind tracers with different excitation temperatures could facilitate such analysis. We further discuss this point in §8.5.

7. WORK EFFICIENCY

In photoevaporating systems, photoheating is responsible for supplying energy to increase the mechanical and thermal energies of the gas while partly being lost through cooling. The efficiency of this energy conversion process largely depends on the irradiating energy flux. By employing our model, we can make an order-of-magnitude estimation for this work efficiency and observe its variation with Φ_{EUV} by comparing the magnitudes of the photoheating with the work required to liberate the gas from gravitational binding. This efficiency provides a physical reference for understanding the basic energy flow operating within photoevaporative winds in different regimes.

We define work efficiency η as the ratio between the integration of the gravitational power per gas mass,

$$\mathcal{P}_{\text{g}} \equiv \frac{GM_*}{2r^2} \mathcal{M} c_s$$

and the integrated specific heating rate Γ_{EUV} (Eq.(5)):

$$\eta \equiv \left(\int \frac{GM_*}{2r^2} \mathcal{M} c_s \frac{ds}{\mathcal{M} c_s} \right) \left(\int \Gamma_{\text{EUV}} \frac{ds}{\mathcal{M} c_s} \right)^{-1}. \quad (69)$$

Again, the integration is taken along a streamline to the height of $\sim R$. The factor of $1/2$ in \mathcal{P}_{g} effectively accounts for the contribution of centrifugal force to the net gravity.

By the definition of the characteristic sound speed for Type I winds (Eq.(15)), η is approximated to

$$\eta \approx \eta^{\text{I}} \equiv \left(\frac{v_{\text{g}}}{c_{\text{ch}}^{\text{I}}} \right)^2 \frac{\mathcal{M} c_s}{c_{\text{ch}}^{\text{I}}} = \varphi^{-1} \mathcal{M} \frac{c_s}{c_{\text{eq}}} \quad (70)$$

The specific value of η differs by the wind regimes (see Table 3) and is summarized in Table 6. The efficiency generally

| Regime | State of winds | η |
|--------|-------------------------------|---|
| A-I | Isothermal, atomic | φ^{-1} |
| B-I | Steadily-heated, free; atomic | $\varphi^{-2/3} x^{-1/3}$ |
| C-I | Gravity-inhibited, atomic | 1 |
| A-II | Isothermal, ionized | $\eta_{\text{A}}^{\text{II}}$ |
| B-II | Free, ionized | $x^{-1} (c_{\text{ch}}^{\text{II}}/c_{\text{eq}})^{-2}$ |
| C-II | Gravity-inhibited, ionized | 1 |

Table 6. Order-of-magnitude estimation for work efficiency in each wind regime.

decreases as the EUV emission rate increases. Note that for Type I winds, η is set by the local variables, namely \mathcal{P}_{g} and Γ_{EUV} , as we assume all the relevant quantities remain constant along the streamline, thus giving $\eta^{\text{I}} = \mathcal{P}_{\text{g}}/\Gamma_{\text{EUV}}$.

For Type II winds, the work efficiency is approximated to

$$\eta \approx \eta^{\text{II}} \equiv x^{-1} \left(\varepsilon \left[1 - \left(\frac{x\varepsilon q}{\varphi} \right)^{1/2} \left(\frac{c_s}{c_{\text{eq}}} \right)^{-\beta} \right] + \left(\frac{\varphi\varepsilon q}{x} \right)^{1/2} \left(\frac{c_s}{c_{\text{eq}}} \right)^{-(\beta+1)} \mathcal{M}^{-1} \right)^{-1}$$

(cf. Eq.(44)). In Regime C-II (gravity-inhibited ionized winds), where $c_s \approx v_{\text{g}}$ and $\mathcal{M} \approx \mathcal{M}_{\text{g}}^{\text{II}}$, the work efficiency is again calculated to be unity, as in Regime C-I. In Regime B-II, using Eq.(43), η^{II} is expressed as

$$\eta^{\text{II}} = x^{-1} \left(\frac{c_{\text{ch}}^{\text{II}}}{c_{\text{eq}}} \right)^{-2}.$$

Given that $c_{\text{ch}}^{\text{II}}$ increases with the EUV emission rate, η^{II} monotonically decreases with increasing φ . For Regime A-II, substituting $c_s \approx c_{\text{eq}}$ and $\mathcal{M} \approx 1$ into η^{II} , the work efficiency reduces to

$$\eta^{\text{II}} = \eta_{\text{A}}^{\text{II}} \equiv x^{-1} \left(\varepsilon \left[1 - \left(\frac{x\varepsilon q}{\varphi} \right)^{1/2} \right] + \left(\frac{\varphi\varepsilon q}{x} \right)^{1/2} \right)^{-1}.$$

In the high flux limit of $\varphi/x \gg 1$, the work efficiency approximately scales as $\eta^{\text{II}} \approx x^{-1/2} \varphi_{\text{II}}^{-1/2}$. In comparison to Type I

winds, the decrease in η with respect to φ is slower. This reflects that in this limit, energy is supplied in terms of reionizations, which is limited by recombination timescale proportional to $\varphi^{-1/2}$ (cf. Eq.(10)).

In summary, the work efficiency generally declines as the EUV emission rate increases, indicating that more photo-energy is directed toward the gas's kinetic energy and is also drained through cooling as the temperature rises sufficiently to activate coolants. In the high flux limit of $\varphi/x \gg 1$, where winds attain an isothermal and ionized state (Regime A-II), the efficiency approximately scales as $\propto \varphi^{-1/2}$ approaching zero. This indicates that a significant portion of the energy is lost by cooling, with only a small fraction contributing to the gas's mechanical and thermal energy. In the opposite limit, where the gas is gravity-inhibited, the efficiency becomes $\eta \approx 1$, meaning efficient conversion of supplied energy into the gas's mechanical and thermal energy. The highest efficiency is achieved when the gas is heated quasi-statically, keeping a practically hydrostatic structure.

We stress that the derived η here is an order-of-magnitude estimation of energy conversion efficiency. The actual work efficiency defined in the form of Eq.(69) should not reach unity even in the gravity-inhibited regime, as the deposited energy must partly be consumed to increase the enthalpy of the gas at least. Nevertheless, the order of η and its φ -dependent trend would remain consistent in more strict estimations. The overall qualitative behaviors of the work efficiency would be applicable to other astrophysical photo-evaporating objects in various scales, such as planetary atmosphere (Murray-Clay et al. 2009; Owen & Alvarez 2016), molecular clouds, blackhole's accretion disk on the Bondi scale, and galactic minihalos.

8. DISCUSSIONS

We have constructed a model primarily tailored for EUV photoevaporation. However, given that the underlying physics are essentially the same, with suitable modifications, the model can in principle be extended to account for other phenomena such as FUV- and X-ray-driven photoevaporation, as well as the photoevaporation of gas composed purely of metal species. As an initial demonstration of this versatility, in §8.1, we approximately estimate the critical FUV and X-ray luminosities, and based on these estimates, we discuss the parameter spaces corresponding to Regimes A, B, and C of FUV- and X-ray-driven winds. In §8.2, We explore how this discussion sheds light on a long-standing issue in the field of protoplanetary disk photoevaporation: the contradictory conclusions on the effectiveness of X-ray photoevaporation. We also examine the potential time-dependent variations of EUV photoevaporation classes arising from stellar and disk evolution in §8.3. Finally, we address the model limitations and caveats of our model in §8.4.

8.1. FUV and X-ray Critical Luminosities

In protoplanetary disk dispersal, FUV and X-ray can also play important roles in driving photoevaporative winds as well as EUV. These other channels of photoevaporation also have wind regimes corresponding to Regimes A, B, and C. The parameter spaces could be analytically derived by constructing a similar phenomenological model to the ones in BMS83 and the present study. Suitable modifications are, however, needed in such models, as the heating rates and equilibrium temperatures in FUV and X-ray photoevaporation differ from those in EUV photoevaporation, and the equilibrium temperatures should depend on the distance and, likely, the stellar luminosities. Nevertheless, we can roughly discuss the parameter spaces of FUV- and X-ray-driven photoevaporative winds by deriving the critical FUV and X-ray luminosities. In this section, we present such discussions, in particular for low-mass stars ($M_* \approx 1 M_\odot$). It will show that hydrodynamical effects can significantly influence temperature determination and, thereby, mass-loss rates of FUV and X-ray photoevaporation in low-mass stars' systems.

FUV heats the gas through photoelectric effects on very small dust grains and polycyclic aromatic hydrocarbons (PAHs). For the heating rate, we adopt the specific photoelectric heating rate of Bakes & Tielens (1994):

$$\Gamma_{\text{FUV}} = 10^{-24} \text{ erg s}^{-1} \frac{G_{\text{FUV}}}{m} \epsilon_{\text{pe}}$$

where G_{FUV} is the stellar FUV flux normalized by the Habing flux ($G_0 \approx 1.6 \times 10^{-3} \text{ erg cm}^{-2} \text{ s}^{-1}$ Habing 1968), and ϵ_{pe} is photoelectric heating efficiency. To make our discussion simple, we assume that the PAH contribution dominates the heating and approximate ϵ_{eq} to a constant with $\epsilon_{\text{eq}} \approx 0.05$. This approximation would suffice for the purpose of this section, although strictly, the photoelectric heating efficiency depends on the ionization and recombination rates (e.g., Bakes & Tielens 1994).

Using Γ_{FUV} , the characteristic sound speed for grain photoelectric heating is derived as

$$\begin{aligned} c_{\text{ch}}^{\text{FUV}} &= \left(\frac{\Gamma_{\text{FUV}} R}{c_p} \right)^{1/3} \approx \left(\frac{10^{-24} \text{ erg s}^{-1} L_{\text{FUV}} \epsilon_{\text{pe}}}{4\pi c_p m G_0 R} \right)^{1/3} \\ &\sim 2.7 \text{ km s}^{-1} \left(\frac{\epsilon}{0.05} \right)^{1/3} \left(\frac{R}{1 \text{ au}} \right)^{-1/3} \left(\frac{c_p}{7/2} \right)^{-1/3} \\ &\quad \times \left(\frac{m}{1.4 m_{\text{H}}} \right)^{-1/3} \left(\frac{L_{\text{FUV}}}{10^{30} \text{ erg s}^{-1}} \right)^{1/3}. \end{aligned}$$

where L_{FUV} is the FUV luminosity of the source. We obtain the critical FUV luminosity from comparisons of $c_{\text{ch}}^{\text{FUV}}$ with

v_g as

$$L_{F,c} \equiv \frac{4\pi c_p G_0 m R_{c,F} v_{c,F}^3}{10^{-24} \text{ erg s}^{-1} \epsilon_{pe}} = \frac{2\pi G_0 m G M_* c_{eq}^F}{10^{-24} \text{ erg s}^{-1} \epsilon_{pe}} \quad (71)$$

$$\approx 1.9 \times 10^{31} \text{ erg s}^{-1} \left(\frac{m}{1.4 m_H} \right) \left(\frac{M_*}{1 M_\odot} \right)$$

$$\times \left(\frac{c_{eq}^F}{3 \text{ km s}^{-1}} \right) \left(\frac{\epsilon_{pe}}{0.05} \right)$$

where $R_{c,F}$ is the critical radius for FUV-heated gas, $v_{c,F}$ is the gravitational velocity at $R_{c,F}$ (Eq.(2)), and c_{eq}^F is the isothermal sound speed of the FUV-heated gas at the equilibrium temperature at $R_{c,F}$. FUV heating mainly works in the atomic and molecular layers of the disk, where strong coolants are abundantly present. It leads to a lower equilibrium temperature, ~ 3000 – 8000 K in atomic gas and ~ 2500 K in fully molecular gas, and correspondingly increasing the critical radius, compared to those of the EUV-heated gas; for low-mass stars, $R_{c,F} \sim 3$ – 12 au (Pascucci et al. 2023). The nominal value of c_{eq}^F in Eq.(71) corresponds to molecular gas with an equilibrium temperature of ~ 2500 K.

The nominal value of $L_{F,c}$ is comparable to or slightly higher than typically adopted FUV luminosities for accreting low-mass stars, $L_{FUV} \approx 10^{30}$ – $10^{31} \text{ erg s}^{-1}$ (e.g., Gorti et al. 2009). The fact that $L_{FUV} > L_{F,c}$ is a necessary condition for an FUV-heated gas to meet the fast-heating condition $c_{ch}^{FUV} > c_{eq}^F$ (Regime A), implies that FUV-irradiated disks of typical low-mass systems are mostly in Regime B. There, the deposited energy by FUV heating efficiently goes into the mechanical energy of the winds without being lost through cooling significantly. The temperatures of winds in Regime B are thus influenced by hydrodynamical effects and are approximately set by the characteristic sound speed, which is less than the equilibrium temperature. The winds can typically form escaping winds without being inhibited by gravity, especially for outer radii, since $L_{FUV} < L_{F,c}$ is required for winds to be in Regime C. We note, however, that $L_{F,c}$ is inversely proportional to the ratio of the PAH abundance in the disk to the interstellar value. FUV-irradiated disks with lower PAH abundances, as often inferred for protoplanetary disks (e.g., Geers et al. 2007; Vicente et al. 2013), are likely composed of the free-wind regime (Regime B) and gravity-inhibited regime (Regime C).

As for X-ray photoevaporation, the heating is caused by the excess energy remaining after the photoionization of various elemental species. In contrast to the EUV heating, not all primary nonthermal electron's energy goes to gas heating; the heating efficiency f_h is $\sim 10\%$ in atomic gas and $\sim 40\%$ in a molecular gas (Maloney et al. 1996). Hence, we estimate the specific heating rate due to (unattenuated) X-rays as

$$\Gamma_X = \frac{f_h}{m} \int \sigma_X(E) \frac{L(E)}{4\pi r^2} dE,$$

where σ_X is the X-ray absorption cross-section, $L(E)$ is the specific X-ray luminosity, and N_H is the column density of hydrogen nuclei. For σ_X , we adopt the cross-section of Wilms et al. (2000),

$$\sigma_X = 2.27 \times 10^{-22} \left(\frac{E}{1 \text{ keV}} \right)^{-2.5},$$

(the fit is adopted from Gorti & Hollenbach (2004)). We rewrite the heating rate to

$$\Gamma_X = \frac{f_h}{m} \frac{L_X}{4\pi r^2} \bar{\sigma}_{x0}$$

using the total X-ray luminosity L_X and the energy-averaged, unattenuated cross-section

$$\bar{\sigma}_{x0} \equiv \frac{\int \sigma_X L dE}{\int L dE}.$$

Then, the characteristic sound speed for the X-ray heating is computed as

$$c_{ch}^X = \left(\frac{\Gamma_X R}{c_p} \right)^{1/3} \approx \left(\frac{f_h L_X \bar{\sigma}_{x0}}{4\pi c_p m R} \right)^{1/3}$$

$$\sim 3.7 \text{ km s}^{-1} \left(\frac{f_h}{0.4} \right)^{1/3} \left(\frac{L_X}{10^{30} \text{ erg s}^{-1}} \right)^{1/3} \left(\frac{c_p}{7/2} \right)^{-1/3}$$

$$\times \left(\frac{m}{1.4 m_H} \right)^{-1/3} \left(\frac{R}{1 \text{ au}} \right)^{-1/3} \left(\frac{\bar{\sigma}_{x0}}{2 \times 10^{-22} \text{ cm}^2} \right)^{1/3}$$

Then, the critical X-ray luminosity is computed as

$$L_{X,c} \equiv \frac{2\pi m G M_* c_{eq}^X}{f_h \bar{\sigma}_{x0}}$$

$$\approx 0.73 \times 10^{31} \text{ erg s}^{-1} \left(\frac{m}{1.4 m_H} \right) \left(\frac{M_*}{1 M_\odot} \right) \quad (72)$$

$$\times \left(\frac{c_{eq}^X}{3 \text{ km s}^{-1}} \right) \left(\frac{f_h}{0.4} \right)^{-1} \left(\frac{\bar{\sigma}_{x0}}{2 \times 10^{-22} \text{ cm}^2} \right)^{-1}$$

where c_{eq}^X is the isothermal sound speed of X-ray-heated gas at the equilibrium temperature at the critical radius for the X-ray-heated gas where c_{eq}^X equals the gravitational velocity (Eq.(2)).

The nominal values of the variables in Eq.(72) have been chosen for molecular gas in a similar manner to Eq.(71), assuming that relatively hard X-rays with $E \approx 1 \text{ keV}$ would reach molecular layers. It means that Eq.(72) gives a criterion for the excitation of molecular winds by X-ray heating when the average energy of the given X-ray spectrum is $\approx 1 \text{ keV}$. For atomic gas, softer X-rays contribute to the heating, but the nominal critical luminosity is likely almost the same at $L_{X,c} \sim 1.4 \times 10^{31} \text{ erg s}^{-1}$, where we set $f_h = 0.1$, $c_{eq}^X = 7 \text{ km s}^{-1}$, and $\bar{\sigma}_{x0} = 1 \times 10^{-21} \text{ cm}^2$ assuming average X-ray energy of $\sim 0.5 \text{ keV}$ and an equilibrium temperature at the critical radius of $\sim 8000 \text{ K}$.

The estimated critical X-ray luminosity is comparable to a high-end X-ray luminosity observed towards T Tauri stars (e.g., Güdel et al. 2007). If the intrinsic X-ray spectra of young low-mass stars had an average energy of observed X-rays of ~ 1 keV, most of the X-ray-irradiated disks would have a significant fraction of gravity-inhibited-wind regions beyond the critical radius (~ 2 – 12 au), depending on the radial profile of the equilibrium temperature. This fact may give implications to a cause for the divergent conclusions on the effectiveness of X-rays for driving photoevaporative winds in the literature (§8.2).

To summarize, low-mass stars need to have FUV and X-ray stellar luminosities comparable to or higher than the typical values in order to drive freely, escaping supersonic winds that are hardly inhibited by gravity. This is because the cross-sections for FUV and X-ray are generally small, and thus the heating rate, which is essentially set by the product of cross-section and local flux, also tends to get relatively small. It means that cross-sections are a fundamentally important quantity to set the rapidness of heating. While a lower cross-section lets photons reach a deeper interior of the disk and has the potential to drive dense winds, the photoheated gas is more susceptible to gravity due to the resulting long heating timescale, leading to weak subsonic winds. Hence, in contrast to often-adopted intuitive assumptions, lower cross-sections do not necessarily result in higher mass-loss rates, especially when the stellar luminosities are below the critical values.

From our discussions here, we can conclude hydrodynamical effects can overall influence temperature determination and, thereby, mass-loss rates of FUV- and X-ray-driven photoevaporative winds for low-mass stars. It highlights the importance of performing hydrodynamics simulations coupled with radiative transfer and chemistry for investigating FUV and X-ray photoevaporation around low-mass stars in general.

8.2. Implications to a Cause for Divergent Conclusions on X-ray Photoevaporation

In the field of protoplanetary disk photoevaporation around low-mass stars, the debate over the effectiveness of X-ray heating in driving strong winds has been ongoing. Some suggest that X-rays can induce a substantial mass-loss rate of $\approx 10^{-8} M_{\odot} \text{ yr}^{-1}$, whereas others have obtained significantly lower mass-loss rates, differing by more than an order of magnitude. The exact reasons for this divergence remain unclear, but it is presumed that the discrepancies stem from the different numerical methods and codes employed, specifically, whether the soft X-ray component is included and whether major coolants and adiabatic cooling are incorporated. Here, we will illustrate how our model, along with the critical X-ray luminosity (Eq.(72)), could provide a plau-

sible and physically coherent explanation for the observed discrepancies across the previous models. Additionally, we will clarify why the diverse numerical methods contributed to the variations in mass-loss rates.

The inquiry regarding the effectiveness of X-ray heating on disk dispersal began with Alexander et al. (2004), who used a 2D model to calculate the self-consistent hydrostatic density structure of an X-ray-irradiated disk with a simplified radiative transfer. Their findings suggested a negligible X-ray photoevaporation rate compared to EUV, indicating that X-ray-driven winds likely play a minor role in disk dispersal.

Subsequently, Gorti et al. (2009) examined the X-ray heating's effectiveness on driving winds through a self-consistent hydrostatic model with radiative transfer and chemistry. The authors obtained a similar conclusion to that of Alexander et al. (2004). Conversely, Ercolano et al. (2009) reached a contradictory conclusion, positing that X-ray heating yields a larger mass-loss rate of $\gtrsim 10^{-9} M_{\odot} \text{ yr}^{-1}$ than typical EUV photoevaporation rates ($\sim 10^{-10} M_{\odot} \text{ yr}^{-1}$). They achieved this through a full 3D Monte Carlo radiative transfer (Ercolano et al. 2008), attributing the discrepancies in the conclusions between the models to the interpretation of the calculation data and the hardness of the adopted X-ray spectra (see Section 5 of Ercolano et al. (2009)). Notably, all models consistently indicated low mass-loss rates when adopting hard X-ray spectra, e.g., those that peak at > 1 keV.

Owen et al. (2010) conducted 2D hydrodynamics simulations of X-ray-driven photoevaporation with a simplified temperature treatment based on the radiative transfer calculations of Ercolano et al. (2009). The gas temperature is given by the equilibrium value, which is parametrized uniquely by the ionization parameter $\xi \equiv L_X / n_H r^2$, and the temperature is given by referencing the ξ – T table in the hydrodynamics simulations. They derived a large mass-loss rate of $\sim 10^{-8} M_{\odot} \text{ yr}^{-1}$, which has been reproduced by follow-up studies using the same table-lookup technique (e.g., Picogna et al. 2019).

Advancing these efforts, Wang & Goodman (2017) and Nakatani et al. (2018b) introduced updated hydrodynamical models, incorporating ray-tracing radiative transfer and mutually consistent thermochemistry and hydrodynamics. However, both studies also concluded that X-ray-driven winds make minor contributions to the mass-loss rate compared to UV-driven winds, though adopted UV and X-ray luminosities and spectra are diverse. It is noteworthy that both Wang & Goodman (2017) and Nakatani et al. (2018b) used a harder X-ray spectrum than that of Ercolano et al. (2009) (see also Section 4.2 of Nakatani et al. (2018b)).

Further analysis by Sellek et al. (2022) explored the impact of the X-ray spectrum hardness on the conclusions regarding the capability of driving winds through X-ray heating using a hydrostatic density grid while performing a full radiative

transfer. Their work revealed that X-rays in the range of a few 100 eV were most effective, with more energetic ones (~ 1 keV) providing insufficient heating to drive winds. This emphasizes the role of adopted irradiation X-ray spectra in the diverse conclusions on the effectiveness of X-ray heating among photoevaporation models.

While our phenomenological model for EUV photoevaporation does not directly address X-ray photoevaporation unless the equilibrium temperature is suitably modified as discussed in §8.1, our model has fruitful insights into the factors contributing to the diverse conclusions on X-ray photoevaporation. Supporting the findings of [Sellek et al. \(2022\)](#), our model and discussions in §8.1 suggest that strong X-ray-driven winds tend to occur when the X-ray spectrum is relatively soft. This can be understood by the fact that the critical luminosity is generally smaller for larger average cross-sections (cf. Eq.(72)), i.e., softer X-ray spectra, which are advantageous in yielding a relatively short heating timescale.

Another important criterion that our model introduces for interpreting the results of photoevaporation models is the estimated representative value of the critical X-ray luminosity (Eq.(72)). Typical X-ray luminosities of low-mass stars fall below this value, indicating that X-ray-driven winds are most likely in the regimes of steadily heated, free winds (Regime B) and gravity-inhibited winds (Regime C). This implies that the winds hardly reach the equilibrium temperature due to the excessively long heating timescale. Hence, hydrodynamical effects, namely internal energy loss by expansion and advection, are not negligible for X-ray-driven photoevaporation. Determining the wind temperature based solely on the equilibrium value, as adopted in hydrostatic models and the ξ - T table-lookup approach of the hydrodynamical models, effectively treats all regions as if they were in Regime A. Consequently, this would lead to an overestimation of temperatures. This, in turn, can underestimate the gravity's effect on winds and subsequent pressure drop, ultimately resulting in an overestimation of mass-loss rates.

Considering the points raised above, it is not surprising that the coupled thermochemical-hydrodynamical models of [Wang & Goodman \(2017\)](#) and [Nakatani et al. \(2018b\)](#) uniformly found a minor contribution of X-ray-driven winds to photoevaporation. In [Wang & Goodman \(2017\)](#), it was assumed that all irradiating X-ray photons have the single energy of 1 keV with $L_X \approx 2.5 \times 10^{30} \text{ erg s}^{-1}$, which is well below the estimated critical X-ray luminosity (Eq.(72)). On the other hand, [Nakatani et al. \(2018b\)](#) (and a follow-up study by [Komaki et al. \(2021\)](#)) used an observed X-ray spectrum towards TW Hya ([Nomura et al. 2007](#)), which is softer than that of [Wang & Goodman \(2017\)](#) but harder than those of [Ercolano et al. \(2009\)](#). This X-ray spectrum yields $\sigma_{X0} \approx 1 \times 10^{-21} \text{ cm}^2$, and X-ray heating primarily occurs mostly in a low column-density layer, where the gas is

practically atomic. The corresponding critical X-ray luminosity is $L_{X,c} \approx 0.56\text{--}1.3 \times 10^{31} \text{ erg s}^{-1}$ with f_h set to 0.1, with uncertainties arising from the uncertain equilibrium sound speed c_{eq}^X . In any case, this critical luminosity is higher than the adopted X-ray luminosity $L_X = 10^{30} \text{ erg s}^{-1}$ in their model, and this would explain why strong X-ray-driven winds are not observed.

Our discussions here suggest a gravitationally influenced nature for (hard) X-ray-driven winds around low-mass stars. However, this does not mean that X-rays are incapable of driving winds; rather, they are easily inhibited by gravity with typical luminosities and tend to be subsonic at lower temperatures than the equilibrium values due to long heating timescales. To obtain physically meaningful X-ray photoevaporation rates, it is imperative to conduct hydrodynamical simulations coupled with radiative transfer and chemistry, employing either a sufficiently large computational boundary or an appropriate outer boundary condition to prevent spurious reflection of subsonic flows at the outer computational boundary and avoid neglecting nonzero mass-loss rates. This aspect remains open to date, leaving X-ray photoevaporation rates still uncertain.

8.3. Possible Time-Dependent Class Variation by Stellar and Disk Evolution

The classification and dynamics of disk photoevaporation are subject to variations contingent upon the evolutionary stages of both the star and the disk. Various factors stemming from the evolution of both stellar and disk components wield influence over the classification and dynamics of disk photoevaporation. This section provides a qualitative exploration of representative factors that contribute to such variations.

The accretion of disk material onto the star can generate strong UV and X-ray emissions by liberating the gravitational energy of the accreting gas. As for FUV, the accretion-generated component can dominate the stellar component at early stages (~ 1 Myr) where the accretion rate is relatively high ([Gorti et al. 2009](#)). The FUV luminosities likely exceed the critical value (Eq.(71)) at this stage if the disk still retains sufficiently abundant PAHs/very small grains. This leads to driving a vigorous FUV photoevaporation. However, as the system evolves and the accretion rate diminishes, stellar emissions become more dominant. The luminosities are relatively small compared to the early stages, correspondingly resulting in weaker photoevaporation. Additionally, if small grains are depleted in later stages, FUV photoevaporation can further attenuate.

On the other hand, strong accretion implies strong inner MHD winds capable of shielding UV and X-ray photons that could otherwise reach the wind region $x > 1$ (e.g., [Turner et al. 2010](#); [Takasao et al. 2018, 2022](#); [Fang et al. 2018, 2023](#)). The column density of the inner wind is higher when

the system is younger and has a stronger wind. Only hard photons manage to penetrate the inner region with an attenuated total flux, leading to a hard spectral class and weakened photoevaporation. However, as the system evolves, the surface density reduces relatively quickly at inner radii since MHD winds are more efficient in removing mass there (Bai 2016; Suzuki et al. 2016). Then, inner winds and disks become more transparent to UV and X-ray radiation, the spectrum transitions to softer. This transition facilitates photons reaching the outer region without significant attenuation in the inner region, potentially exciting vigorous winds. This interaction between radiation and inner winds is supported by observational evidence (Pascucci et al. 2020). Hence, as well as the time-variation of accretion-powered UV and X-ray, accounting for spectral class and wind regime variations is crucial for understanding disk dispersal.

Moreover, stellar evolution, particularly for stars exhibiting time-varying surface magnetic activity, significantly influences the classification and dynamics of disk photoevaporation (Kunitomo et al. 2021; Nakatani et al. 2023). For instance, intermediate-mass stars may possess a surface convective zone at ages below ~ 1 Myr, resulting in strong EUV and X-ray emissions from magnetic activity. During this phase, the spectral class is likely H, and strong photoevaporation may ensue due to potentially high UV and X-ray luminosities. However, as these stars lose their surface convective zones around ages ~ 1 –10 Myr, EUV and X-ray emissions can significantly weaken. It results in softer EUV emissions from moderately hot photospheres, and photoevaporation is weakened due to a low EUV emission rate.

In conclusion, the long-term variability of stellar luminosity, stellar activity, disk accretion rate, and grain abundance significantly shape the classification and dynamics of photoevaporation at different stages of disk dispersal. This indicates that the wind velocity, temperature, and ionization state significantly vary according to the system’s evolutionary state, underscoring the importance of considering temporal variations in photoevaporation for understanding overall disk evolution and interpreting observational data on winds.

8.4. Model Limitation and Caveats

Our model is inherently subject to uncertainties originating from the assumptions we have adopted for simplicity and therefore has caveats to interpret the results. Here, we will address these points in this section. We emphasize that, regardless of these model limitations and caveats, our model offers valuable insights into the fundamental physics underlying EUV-driven photoevaporative winds and systematic variations of wind characteristics across a broad parameter space.

Incorporation of Helium photoionization—Our model focuses solely on EUV heating associated with hydrogen photoion-

ization, neglecting potential contributions from helium photoionization. While the ionization potentials of He I and He II are relatively high (approximately 24.6 eV and 54.4 eV, respectively), their overall impact on the photoheating rate and ionization state of hydrogen in photoevaporative winds is expected to be modest. Despite the about an order of magnitude higher absorption cross-section per He I/He II than the cross-section per H I in the EUV range, the elemental helium abundance of $\approx 10\%$, limits the total photoheating rate increment to only a few-fold at most when compared to the heating rate used in our model (Γ_{EUV} ; Eq.(4)). Similarly, the electron consumption resulting from the recombination of ionic helium species is projected to have a perturbing impact on the ionization state of hydrogen within photoevaporative winds. Consequently, the order estimation in the present study is expected to remain largely unaltered even with the incorporation of helium contributions.

Self-attenuation effects in photoevaporative winds—We have approximated the absorption attenuation factors, χ_e and χ_i (see Eqs.(4) and (6)), as near unity, thereby assuming optically thin photoevaporative winds. However, especially in cases involving atomic flows, the photoevaporative winds in the inner region can shield to prevent EUV from reaching the outer region. This self-attenuation effect can reduce the attenuation factors significantly. In this case, the actual flux reaching the disk is smaller than the value used in our model for a given Φ_{EUV} , and thus the actual heating timescale can correspondingly become longer if we incorporate corrections due to self-attenuation. This would lead to an increase in the critical EUV emission rate Φ_c by several times and corresponding adjustments in the boundaries of wind regimes on the phase diagram. Hence, the derived critical EUV emission rate should be interpreted as a lower limit, suggesting that the derived radius limits presented in §6 should be considered upper limits.

Since the self-attenuation is expected to be increasingly pronounced at outer radii, the actual boundary between Regimes A and B may not adhere to a simple linear relation as depicted in our model but rather may be described by a convex downward function. A similar is true for the boundary between Regimes B and C; the gravity-inhibited regime can be somewhat radially extended than the predictions of our model.

Additionally, in the 2D cross-sectional view of a photoevaporating disk, the wind region would exhibit a vertically stratified structure with Regimes A, B, and C present in distinct layers. This stratification arises due to the irradiating spectrum becoming harder as it is attenuated. In the most attenuated layer, both the photon number flux and the average cross-section are small, resulting in the layer being in a gravity-inhibited regime. In a moderately attenuated layer, the photoheated layer can exhibit characteristics of

Regimes A and B if Φ_{EUV} is sufficiently high. We will explore this aspect in more detail in §5.

Inclusion of neutral coolants—Our model primarily relies on coolants effective in H II regions, such as forbidden lines of ionic metals, $\text{Ly}\alpha$, and radiative recombination, which results in an equilibrium temperature of $\approx 10^4$ K for both atomic and ionized gas. However, as also discussed in §8.1, atomic and molecular cooling, such as infrared emission from O I and H_2 , can be significant in the neutral layer of a disk. This can lead to a substantially lower equilibrium temperature on the order of $\sim 10^2$ – 10^3 K. Thus, the equilibrium temperature would, in principle, depend on whether the gas is in a neutral or ionized state, which is determined by the luminosity of the ionizing radiation.

This realization suggests the existence of a new Type I wind regime characterized by winds exhibiting equilibrium temperatures typical of neutral gas. This regime would fall within the Type I regime and bridge connections to the Type II regime at the high-flux parameter space. The prevalence of this regime is expected, particularly for H-class EUV spectra, which yield a low $\bar{\sigma}_0$, creating the base within the deep interior of the neutral layer. Therefore, an important next step for the phenomenological model is to incorporate the effects of neutral coolants to formulate the new Type I regime and determine the corresponding parameter space within the phase diagram.

Investigation of the inner region—While our study primarily focuses on the outer radius $x > 1$, where vigorous winds are anticipated due to weak gravity, investigating the inner region $x < 1$ is also necessary. This disk corona, i.e., nearly hydrostatic gas in $x < 1$, has the potential to produce weak winds whose escaping rate exponentially decays inward, potentially serving as a source for time variation. Investigating this region could give valuable insights into achievable velocities and temperatures therein, which could provide surface mass-loss rates available for population synthesis studies and be used to discuss the observability of infrared wind tracers.

Uncertainty in recombination timescale—There remains uncertainty in the recombination timescale used in this study (Eq.(10)), particularly regarding the applicability of the base density formulation (Eq.(9)) across different EUV emission rates and spectra. If the base density has another formulation within certain parameter spaces, it could impact the boundary of Types I and II regimes. Although our key findings — e.g., the presence of two wind types with Type II being achieved at a relatively high Φ_{EUV} — qualitatively remain unchanged by such modifications, it is necessary to examine the general applicability of Eq.(9) by comparing the base density with numerical calculations.

Additionally, our model has not accounted for the density reduction due to the expansion of evaporating gas, leading to

an overestimation of additional energy supply through reionizations within the ionized winds. Addressing this is another crucial aspect that needs to be incorporated into an updated model.

Integration with MHD winds—Magnetohydrodynamics (MHD) winds are another important disk-dispersal process, especially during the early stage of protoplanetary disk evolution when the disk is relatively massive (e.g., Turner et al. 2014; Pascucci et al. 2023, see also §8.3). Our model could be applied to the determination of MHD winds’ thermochemical states if the winds have sufficiently low densities, allowing photochemical processes to dominate other heating sources (e.g., ambipolar diffusion Garcia et al. 2001a,b). The velocity achieved by MHD winds would set whether the gas can reach the equilibrium temperature. In high-velocity winds, the gas may not have enough time to be heated, resulting in relatively low temperatures. Thus, corresponding modifications are necessary to the definition of c_{ch} (Eq.(15)) for the temperature estimation with accounting for this effect.

Similarly, since the base density of MHD winds is not related to the photoionization and recombination rates in general, the estimation of the recombination timescale also needs to be modified. With the updated recombination timescale, the same criteria (Eqs.(13) and (14)) would still be applicable to infer the ionization state of the winds. Overall, while our model is not directly applicable to MHD winds, it could be adapted by treating other heating processes, MHD winds’ velocities, and base densities.

8.5. Prospects for Potential Applications to Photoevaporative Wind Observations

Since the main scope of this paper is to broaden our understanding of EUV-driven photoevaporation in a physically consistent manner, we will leave a detailed discussion on the observational applications and tests of our model for future studies. Nevertheless, we describe here the potential utility of our model in investigating photoevaporative winds and stellar parameters and outline the steps that need to be addressed to that end.

We have demonstrated that EUV-driven winds have a temperature gradient in the radial direction, even within the H II region. When the spectrum is soft, such as those softer than a blackbody spectrum with an effective temperature of $T_{\text{eff}} \lesssim 5 \times 10^4$ K, the H II region extends across the isothermal and non-isothermal wind regimes (Regimes A-II and B-II). On the other hand, with hard spectra, the thermal balance dictates the temperature of the H II region, resulting in isothermal winds. In both cases, there is a maximum radius beyond which the H II region cannot extend (§6), and the winds transition to being atomic with lower temperatures.

These findings suggest that the observed size of the ionized region size can vary depending on the ionized gas tracers

used, which have different excitation temperatures. By comparing the sizes of the ionized region using different tracers, we can estimate the average EUV energy of the source and then determine the source's EUV emission rate Φ_{EUV} , following a similar procedure as outlined in §6.

The expected structure of emissions from various tracers can be outlined as follows. When the EUV spectrum is relatively hard, high-temperature ($\approx 10^4$ K) ionized gas tracers (e.g., [Ne II] 12.81 μm , [O II] and [O III] optical lines) exhibit a compact emission (Regime A-II). This region is surrounded by a more extended emission of neutral gas tracers (e.g., [O I] 6300 Å, [O I] 63 μm , and [C II] 158 μm) with a decrease in temperature towards the radial direction (Regimes A-I and B-I). In contrast, when the spectrum is soft, the high-temperature ionized region is encircled by more extended emissions from intermediate-temperature (≈ 5000 – 10^4 K) ionized gas tracers (e.g., [S II] and [N II] optical lines; Regime B-II), followed by lower-temperature neutral gas tracers extending further outward (Regime B-I). Note that Φ_{EUV} must exceed the critical EUV emission rates (cf. Eqs.(17) and (49)) to yield the high-temperature ionized region.

Recent JWST observations have revealed relatively compact [Ar II] emissions compared to [Ne II] and [Ne III] emissions for T Cha (Bajaj et al. 2024; Sellek et al. 2024). These differences in emission sizes, however, are concluded to be likely due to distinct photoionization processes for each tracer, specifically EUV ionization versus X-ray ionization. Considering that low-mass stars commonly exhibit X-rays, generalizing our model to the X-ray wavelengths appears to be a crucial step to making it available for inferring spectra and luminosities of low-mass stars based on the different emission extensions of wind tracers.

Nevertheless, our model can further be expanded to develop an analytic model for X-ray photoevaporation, as discussed in §8.1. By integrating our EUV model with such an X-ray photoevaporation model, an analytical approach can be formulated to estimate the line intensities of ionized gas tracers, similar to the approach by Hollenbach & Gorti (2009). Such a model provides analytical predictions generalized by incorporating hydrodynamical effects on temperature and ionization state determination, thereby updating the currently existing models that assume the equilibrium temperatures determined by thermochemical balance.

Additionally, those models are of great use for investigating free-free emissions observed towards young sources and estimating Φ_{EUV} based on the observed free-free flux density (Pascucci et al. 2012; Ricci et al. 2021). The resulting spatial distribution of free-free emissions is valuable for interpreting the spatially resolved data of future ngVLA observations and exploring the origins of these emissions.

9. SUMMARY AND PROSPECTS

In the canonical picture of EUV photoevaporation, the photoevaporative winds consist of ionized gas at equilibrium temperatures $\approx 10^4$ K, corresponding to wind speeds $\approx 10 \text{ km s}^{-1}$ beyond the gravitational radius (Hollenbach et al. 1994) or critical radius (Liffman 2003). We have delved into the conditions under which this canonical picture holds true, constructing a phenomenological model based on the analytic approach of Begelman et al. (1983). The resulting generalized picture applies across the whole range of conditions where photoevaporation is possible, and yields estimates for the temperature, speed, and ionization state that EUV-driven disk winds exhibit as functions of four parameters: EUV luminosity, spectral hardness, distance from the radiation source, and the source's mass. These are the main findings:

1. As in the model of Begelman et al. (1983), photoevaporative winds occur in three hydrodynamical regimes: isothermal (Regime A); free-flowing (Regime B), and gravity-inhibited (Regime C). Isothermal winds occur when the heating timescale is shorter than both the wind crossing and gravitational timescales, whereas gravity-inhibited winds result when the heating timescale is longer than the gravitational timescale. In all other cases, the winds transition into free winds.
2. The canonical picture applies only in a region of the parameter space characterized by high EUV fluxes. This parameter region is denoted Regime A-II and is represented by red shading without vertical gray stripes in the phase diagrams of Figures 4, 5, 6, and 7, as summarized in Table 3.
3. To form isothermal winds, the EUV emission rate must at least exceed the critical value (Eq.(17)), which is defined by the stellar mass, equilibrium temperature, and spectral hardness.
4. For lower EUV fluxes, the winds are cooler than the equilibrium temperature due to a longer heating timescale. This results in two distinct regimes:
 - At larger disk radii where gravity is weak, the low-temperature winds escape freely without significant gravitational influence (Regime B; green and orange regions in the figures).
 - Close-in, gravity is strong and inhibits the winds, leading to a substantial pressure drop (Regime C; blue regions in the figures).
5. The phase diagrams divide into three classes depending on the hardness of the EUV spectrum, as parameterized by ε and q (Eqs. (18) and (12)).

- *H-class*: Characterized by hard spectra, depositing a relatively large energy per photoionization. Ionized winds in this class are always characterized by isothermal flows at the equilibrium temperature (Regime A-II), with the possibility of isothermal atomic winds in a limited parameter space (Regime A-I). Spectra from young low-mass stars with strong surface magnetic activity are expected to fall into this class.
- *Sa-class*: One of the two soft-spectrum classes, where advection is more effective in maintaining atomic hydrogen in the winds than recombination. With little energy deposited per photoionization, multiple reionizations are necessary before the gas heats to the equilibrium temperature. This results in cooler ionized winds that either escape freely (Regime B-II) or are gravity-inhibited (Regime C-II). Spectra in this class may be rarer than the H-class spectra, with main-sequence intermediate-mass stars potentially falling in the Sa class.
- *Sr-class*: Same as Sa-class, but with recombination more effective than advection in maintaining atomic hydrogen in the winds. The key distinction is that Sa-class has a parameter region where energy deposition through reionizations is negligible in ionized winds (see §3.6). Sr-class appears to occur rarely if ever in the context of protoplanetary disk dispersal.

We have evaluated the model’s predictions by comparing them against hydrodynamics simulations treating the radiative transfer and disequilibrium thermochemistry (§5). There is broad concurrence between the analytic model and the numerical results across orders of magnitude in the EUV emission rate and a wide range in spectral hardness. Refining the model and ensuring its applicability across various EUV environments will nevertheless require more exhaustive assessments with diverse EUV spectra and flow geometries.

To demonstrate the practical utility of the derived typical temperature and speed of the winds, we have estimated the limiting radius of the H II region to which ionized winds can extend (§6). We have shown that this limiting radius is determined by the EUV emission rate, average absorption cross-section, isothermal sound speed at the equilibrium temperature, and spectral hardness. Our analysis suggests that the EUV emission rate can potentially be constrained by comparing the radial sizes of the H II regions observed in ionized gas tracers with different excitation temperatures — an avenue we intend to explore in future investigations. Furthermore, our analysis has revealed that while applying the canonical picture of EUV photoevaporation to disks around massive

stars is well justified, the same does not hold for disks around young low-mass stars. Therefore, when interpreting observations of ionized wind tracers or conducting numerical simulations of photoevaporation for low-mass stars, it is crucial to take into account the finite timescales of photoheating and photoionization.

We have also estimated the work efficiency, or ratio of the work necessary to move the gas against gravity to the energy deposited in that gas through photoheating (§7). We find that the efficiency is of order unity for gravity-inhibited winds and is highest when the gas is quasi-statically heated. Conversely, the efficiency drops as the EUV emission rate increases and more energy is directed towards gas kinetic and thermal energy or is lost to radiative cooling. At the highest fluxes, the efficiency scales as $\Phi_{\text{EUV}}^{-1/2}$, where Φ_{EUV} represents the rate at which the source emits EUV photons. The scaling in the efficiency aligns with that found by numerical simulations in the context of planetary atmospheric escape (Murray-Clay et al. 2009; Owen & Alvarez 2016), suggesting that our results could be applied to understanding EUV photoevaporation across various classes of astrophysical objects (Mitani et al. in prep).

The analytic model has the potential to be extended to FUV and X-ray photoevaporation with suitable modifications, providing a tool to explore the effectiveness of these energy bands in disk dispersal over an even wider parameter space (§8.1). Additionally, the model has potential to explain divergent conclusions in the literature regarding X-ray photoevaporation (§8.2). We acknowledge that uncertainties persist in the analysis, leaving room for further refinements, including those discussed in §8.4. Specifically, it is crucial to validate the predictions by comparing them against numerical simulations that treat the radiative transfer and time-dependent photochemistry. Additionally, it will be essential to update the model to accommodate cases where the spectrum covers wider ranges in photon energy. With these caveats in mind, we have discussed prospected applications of our model to observations §8.5.

Since the model is analytic, it can be extended to enable exploring the detectability of photoevaporative winds and deriving mass-loss rates across a wide parameter space, which we hope will yield fresh insights into disk dispersal from both observational and theoretical perspectives. Moreover, the model provides a solid foundation for understanding photoevaporation in astrophysical objects including planets, molecular clouds, and galactic mini-halos.

ACKNOWLEDGMENTS

We thank the reviewer for the practical comments. R.N. is supported by the Japan Society for the Promotion of Science (JSPS), Overseas Research Fellowship. S.T. was supported by the JSPS KAKENHI grant Nos. JP21H04487, JP22K14074, and JP22KK0043. This research was performed in part at the Jet Propulsion Laboratory, California Institute of Technology, under contract 80NM0018D0004 with the National Aeronautics and Space Administration and with the support of the NASA Exoplanets Research Program through grant 17-XRP17_2-0081 to N.J.T. Numerical computations were carried out on the Cray XC50 at the Center for Computational Astrophysics, National Astronomical Observatory of Japan. ©2024. All rights reserved.

Software: Numpy (Harris et al. 2020), Matplotlib (Hunter 2007), Astropy (Astropy Collaboration et al. 2013, 2018, 2022), SciPy (Virtanen et al. 2020)

REFERENCES

- Alexander, R., Pascucci, I., Andrews, S., Armitage, P., & Cieza, L. 2014, in *Protostars and Planets VI*, ed. H. Beuther, R. S. Klessen, C. P. Dullemond, & T. Henning, 475, doi: [10.2458/azu_uapress_9780816531240-ch021](https://doi.org/10.2458/azu_uapress_9780816531240-ch021)
- Alexander, R. D., Clarke, C. J., & Pringle, J. E. 2004, *MNRAS*, 354, 71, doi: [10.1111/j.1365-2966.2004.08161.x](https://doi.org/10.1111/j.1365-2966.2004.08161.x)
- . 2005, *MNRAS*, 358, 283, doi: [10.1111/j.1365-2966.2005.08786.x](https://doi.org/10.1111/j.1365-2966.2005.08786.x)
- Astropy Collaboration, Robitaille, T. P., Tollerud, E. J., et al. 2013, *A&A*, 558, A33, doi: [10.1051/0004-6361/201322068](https://doi.org/10.1051/0004-6361/201322068)
- Astropy Collaboration, Price-Whelan, A. M., Sipőcz, B. M., et al. 2018, *AJ*, 156, 123, doi: [10.3847/1538-3881/aabc4f](https://doi.org/10.3847/1538-3881/aabc4f)
- Astropy Collaboration, Price-Whelan, A. M., Lim, P. L., et al. 2022, *apj*, 935, 167, doi: [10.3847/1538-4357/ac7c74](https://doi.org/10.3847/1538-4357/ac7c74)
- Bai, X.-N. 2016, *ApJ*, 821, 80, doi: [10.3847/0004-637X/821/2/80](https://doi.org/10.3847/0004-637X/821/2/80)
- Bajaj, N. S., Pascucci, I., Gorti, U., et al. 2024, *AJ*, 167, 127, doi: [10.3847/1538-3881/ad22e1](https://doi.org/10.3847/1538-3881/ad22e1)
- Bakes, E. L. O., & Tielens, A. G. G. M. 1994, *ApJ*, 427, 822, doi: [10.1086/174188](https://doi.org/10.1086/174188)
- Begelman, M. C., McKee, C. F., & Shields, G. A. 1983, *ApJ*, 271, 70, doi: [10.1086/161178](https://doi.org/10.1086/161178)
- Bertoldi, F. 1989, *ApJ*, 346, 735, doi: [10.1086/168055](https://doi.org/10.1086/168055)
- Bertoldi, F., & McKee, C. F. 1990, *ApJ*, 354, 529, doi: [10.1086/168713](https://doi.org/10.1086/168713)
- Ercolano, B., Clarke, C. J., & Drake, J. J. 2009, *ApJ*, 699, 1639, doi: [10.1088/0004-637X/699/2/1639](https://doi.org/10.1088/0004-637X/699/2/1639)
- Ercolano, B., Drake, J. J., Raymond, J. C., & Clarke, C. C. 2008, *ApJ*, 688, 398, doi: [10.1086/590490](https://doi.org/10.1086/590490)
- Fang, M., Pascucci, I., Edwards, S., et al. 2023, *ApJ*, 945, 112, doi: [10.3847/1538-4357/acb2c9](https://doi.org/10.3847/1538-4357/acb2c9)
- . 2018, *ApJ*, 868, 28, doi: [10.3847/1538-4357/aae780](https://doi.org/10.3847/1538-4357/aae780)
- Font, A. S., McCarthy, I. G., Johnstone, D., & Ballantyne, D. R. 2004, *ApJ*, 607, 890, doi: [10.1086/383518](https://doi.org/10.1086/383518)
- Garcia, P. J. V., Cabrit, S., Ferreira, J., & Binette, L. 2001a, *A&A*, 377, 609, doi: [10.1051/0004-6361:20011146](https://doi.org/10.1051/0004-6361:20011146)
- Garcia, P. J. V., Ferreira, J., Cabrit, S., & Binette, L. 2001b, *A&A*, 377, 589, doi: [10.1051/0004-6361:20011145](https://doi.org/10.1051/0004-6361:20011145)
- Geers, V. C., van Dishoeck, E. F., Visser, R., et al. 2007, *A&A*, 476, 279, doi: [10.1051/0004-6361:20078466](https://doi.org/10.1051/0004-6361:20078466)
- Gorti, U., Dullemond, C. P., & Hollenbach, D. 2009, *ApJ*, 705, 1237, doi: [10.1088/0004-637X/705/2/1237](https://doi.org/10.1088/0004-637X/705/2/1237)
- Gorti, U., & Hollenbach, D. 2004, *ApJ*, 613, 424, doi: [10.1086/422406](https://doi.org/10.1086/422406)
- Güdel, M., Briggs, K. R., Arzner, K., et al. 2007, *A&A*, 468, 353, doi: [10.1051/0004-6361:20065724](https://doi.org/10.1051/0004-6361:20065724)
- Habing, H. J. 1968, *BAN*, 19, 421
- Harris, C. R., Millman, K. J., van der Walt, S. J., et al. 2020, *Nature*, 585, 357, doi: [10.1038/s41586-020-2649-2](https://doi.org/10.1038/s41586-020-2649-2)
- Hollenbach, D., & Gorti, U. 2009, *ApJ*, 703, 1203, doi: [10.1088/0004-637X/703/2/1203](https://doi.org/10.1088/0004-637X/703/2/1203)
- Hollenbach, D., Johnstone, D., Lizano, S., & Shu, F. 1994, *ApJ*, 428, 654, doi: [10.1086/174276](https://doi.org/10.1086/174276)
- Hollenbach, D., Johnstone, D., & Shu, F. 1993, in *Astronomical Society of the Pacific Conference Series*, Vol. 35, *Massive Stars: Their Lives in the Interstellar Medium*, ed. J. P. Cassinelli & E. B. Churchwell, 26
- Hunter, J. D. 2007, *Computing in Science & Engineering*, 9, 90, doi: [10.1109/MCSE.2007.55](https://doi.org/10.1109/MCSE.2007.55)
- Iliev, I. T., Shapiro, P. R., & Raga, A. C. 2005, *MNRAS*, 361, 405, doi: [10.1111/j.1365-2966.2005.09155.x](https://doi.org/10.1111/j.1365-2966.2005.09155.x)

- Kahn, F. D. 1954, *BAN*, 12, 187
- Komaki, A., Nakatani, R., & Yoshida, N. 2021, *ApJ*, 910, 51, doi: [10.3847/1538-4357/abe2af](https://doi.org/10.3847/1538-4357/abe2af)
- Kunitomo, M., Ida, S., Takeuchi, T., et al. 2021, *ApJ*, 909, 109, doi: [10.3847/1538-4357/abdb2a](https://doi.org/10.3847/1538-4357/abdb2a)
- Liffman, K. 2003, *PASA*, 20, 337, doi: [10.1071/AS03019](https://doi.org/10.1071/AS03019)
- Maeder, A., & Meynet, G. 1987, *A&A*, 182, 243
- Maloney, P. R., Hollenbach, D. J., & Tielens, A. G. G. M. 1996, *ApJ*, 466, 561, doi: [10.1086/177532](https://doi.org/10.1086/177532)
- McElroy, D., Walsh, C., Markwick, A. J., et al. 2013, *A&A*, 550, A36, doi: [10.1051/0004-6361/201220465](https://doi.org/10.1051/0004-6361/201220465)
- Mignone, A., Bodo, G., Massaglia, S., et al. 2007, *ApJS*, 170, 228, doi: [10.1086/513316](https://doi.org/10.1086/513316)
- Murray-Clay, R. A., Chiang, E. I., & Murray, N. 2009, *ApJ*, 693, 23, doi: [10.1088/0004-637X/693/1/23](https://doi.org/10.1088/0004-637X/693/1/23)
- Nakatani, R., Fialkov, A., & Yoshida, N. 2020, *ApJ*, 905, 151, doi: [10.3847/1538-4357/abc5b4](https://doi.org/10.3847/1538-4357/abc5b4)
- Nakatani, R., Hosokawa, T., Yoshida, N., Nomura, H., & Kuiper, R. 2018a, *ApJ*, 857, 57, doi: [10.3847/1538-4357/aab70b](https://doi.org/10.3847/1538-4357/aab70b)
- . 2018b, *ApJ*, 865, 75, doi: [10.3847/1538-4357/aad9fd](https://doi.org/10.3847/1538-4357/aad9fd)
- Nakatani, R., & Takasao, S. 2022, *ApJ*, 930, 124, doi: [10.3847/1538-4357/ac63a0](https://doi.org/10.3847/1538-4357/ac63a0)
- Nakatani, R., Turner, N. J., Hasegawa, Y., et al. 2023, *ApJL*, 959, L28, doi: [10.3847/2041-8213/ad0ed8](https://doi.org/10.3847/2041-8213/ad0ed8)
- Nakatani, R., & Yoshida, N. 2019, *ApJ*, 883, 127, doi: [10.3847/1538-4357/ab380a](https://doi.org/10.3847/1538-4357/ab380a)
- Nomura, H., Aikawa, Y., Tsujimoto, M., Nakagawa, Y., & Millar, T. J. 2007, *ApJ*, 661, 334, doi: [10.1086/513419](https://doi.org/10.1086/513419)
- Owen, J. E., & Alvarez, M. A. 2016, *ApJ*, 816, 34, doi: [10.3847/0004-637X/816/1/34](https://doi.org/10.3847/0004-637X/816/1/34)
- Owen, J. E., Ercolano, B., Clarke, C. J., & Alexander, R. D. 2010, *MNRAS*, 401, 1415, doi: [10.1111/j.1365-2966.2009.15771.x](https://doi.org/10.1111/j.1365-2966.2009.15771.x)
- Pascucci, I., Cabrit, S., Edwards, S., et al. 2023, in *Astronomical Society of the Pacific Conference Series*, Vol. 534, *Protostars and Planets VII*, ed. S. Inutsuka, Y. Aikawa, T. Muto, K. Tomida, & M. Tamura, 567, doi: [10.48550/arXiv.2203.10068](https://doi.org/10.48550/arXiv.2203.10068)
- Pascucci, I., Gorti, U., & Hollenbach, D. 2012, *ApJL*, 751, L42, doi: [10.1088/2041-8205/751/2/L42](https://doi.org/10.1088/2041-8205/751/2/L42)
- Pascucci, I., Ricci, L., Gorti, U., et al. 2014, *ApJ*, 795, 1, doi: [10.1088/0004-637X/795/1/1](https://doi.org/10.1088/0004-637X/795/1/1)
- Pascucci, I., Banzatti, A., Gorti, U., et al. 2020, *ApJ*, 903, 78, doi: [10.3847/1538-4357/abba3c](https://doi.org/10.3847/1538-4357/abba3c)
- Picogna, G., Ercolano, B., Owen, J. E., & Weber, M. L. 2019, *MNRAS*, 487, 691, doi: [10.1093/mnras/stz1166](https://doi.org/10.1093/mnras/stz1166)
- Ricci, L., Harter, S. K., Ercolano, B., & Weber, M. 2021, *ApJ*, 913, 122, doi: [10.3847/1538-4357/abf5d8](https://doi.org/10.3847/1538-4357/abf5d8)
- Sellek, A. D., Clarke, C. J., & Ercolano, B. 2022, *MNRAS*, 514, 535, doi: [10.1093/mnras/stac1148](https://doi.org/10.1093/mnras/stac1148)
- Sellek, A. D., Bajaj, N. S., Pascucci, I., et al. 2024, *AJ*, 167, 223, doi: [10.3847/1538-3881/ad34ae](https://doi.org/10.3847/1538-3881/ad34ae)
- Shapiro, P. R., Iliev, I. T., & Raga, A. C. 2004, *MNRAS*, 348, 753, doi: [10.1111/j.1365-2966.2004.07364.x](https://doi.org/10.1111/j.1365-2966.2004.07364.x)
- Shoda, M., & Takasao, S. 2021, *A&A*, 656, A111, doi: [10.1051/0004-6361/202141563](https://doi.org/10.1051/0004-6361/202141563)
- Shu, F. H., Johnstone, D., & Hollenbach, D. 1993, *Icarus*, 106, 92, doi: [10.1006/icar.1993.1160](https://doi.org/10.1006/icar.1993.1160)
- Suzuki, T. K., Ogihara, M., Morbidelli, A., Crida, A., & Guillot, T. 2016, *A&A*, 596, A74, doi: [10.1051/0004-6361/201628955](https://doi.org/10.1051/0004-6361/201628955)
- Takasao, S., Tomida, K., Iwasaki, K., & Suzuki, T. K. 2018, *ApJ*, 857, 4, doi: [10.3847/1538-4357/aab5b3](https://doi.org/10.3847/1538-4357/aab5b3)
- . 2022, *ApJ*, 941, 73, doi: [10.3847/1538-4357/ac9eb1](https://doi.org/10.3847/1538-4357/ac9eb1)
- Tanaka, K. E. I., Nakamoto, T., & Omukai, K. 2013, *ApJ*, 773, 155, doi: [10.1088/0004-637X/773/2/155](https://doi.org/10.1088/0004-637X/773/2/155)
- Turner, N. J., Carballido, A., & Sano, T. 2010, *ApJ*, 708, 188, doi: [10.1088/0004-637X/708/1/188](https://doi.org/10.1088/0004-637X/708/1/188)
- Turner, N. J., Fromang, S., Gammie, C., et al. 2014, in *Protostars and Planets VI*, ed. H. Beuther, R. S. Klessen, C. P. Dullemond, & T. Henning, 411–432, doi: [10.2458/azu_uapress_9780816531240-ch018](https://doi.org/10.2458/azu_uapress_9780816531240-ch018)
- Vicente, S., Berné, O., Tielens, A. G. G. M., et al. 2013, *ApJL*, 765, L38, doi: [10.1088/2041-8205/765/2/L38](https://doi.org/10.1088/2041-8205/765/2/L38)
- Virtanen, P., Gommers, R., Oliphant, T. E., et al. 2020, *Nature Methods*, 17, 261, doi: [10.1038/s41592-019-0686-2](https://doi.org/10.1038/s41592-019-0686-2)
- Wang, L., & Goodman, J. 2017, *ApJ*, 847, 11, doi: [10.3847/1538-4357/aa8726](https://doi.org/10.3847/1538-4357/aa8726)
- Wilms, J., Allen, A., & McCray, R. 2000, *ApJ*, 542, 914, doi: [10.1086/317016](https://doi.org/10.1086/317016)
- Woods, D. T., Klein, R. I., Castor, J. I., McKee, C. F., & Bell, J. B. 1996, *ApJ*, 461, 767, doi: [10.1086/177101](https://doi.org/10.1086/177101)

APPENDIX

A. BASIC NOTES FOR THE ANALYTICAL MODEL

We list symbols used in our phenomenological model in Table 7.

Throughout this paper, we use “region” to denote spatial extents, such as the H II region, region of $x > 1$, or region where $s < R$. The word “phase diagram” refers to the x - φ map. In contrast, the ϵ - q plane is referred to as the “spectral-hardness diagram.” We use “parameter space” to indicate a certain area of the phase diagrams and the spectral-hardness diagram. The term “regime” is employed to describe the parameter spaces where the same qualitative properties are shared, such as Regime A, Type I regime, among others. Therefore, “parameter space” and “regime” are utilized in a different context from “region” consistently.

B. MATHEMATICAL PROOF FOR TYPE II
CHARACTERISTIC SOUND SPEED EXCEEDING
THE EQUILIBRIUM SOUND SPEED IN H-CLASS

In §4.5.1, we mention that $c_{\text{ch}}^{\text{II}} > c_{\text{eq}}$ generally holds for the H-class ($\{(\epsilon, q) | \epsilon > 1 \cup \epsilon q > 1\}$), and it can be mathematically proven from Eq.(41). We demonstrate this proof in this Appendix.

When $\epsilon > 1$, it is straightforward to see that $c_{\text{ch}}^{\text{II}} > c_{\text{eq}}$, as it necessitates

$$\left(\frac{c_{\text{ch}}^{\text{II}}}{c_{\text{eq}}}\right)^2 > \epsilon$$

according to Eq.(41). On the other hand, when $\epsilon < 1$ and $\epsilon q > 1$, the parameter space of interest is $\varphi > \max(1, q)\epsilon x = \epsilon qx$. In this range,

$$\begin{aligned} \left(\frac{c_{\text{ch}}^{\text{II}}}{c_{\text{eq}}}\right)^2 &= \epsilon + \left(\frac{\varphi \epsilon q}{x}\right)^{1/2} \left(\frac{c_{\text{ch}}^{\text{II}}}{c_{\text{eq}}}\right)^{-(\beta+1)} \left(1 - \varphi^{-1} \epsilon x \frac{c_{\text{ch}}^{\text{II}}}{c_{\text{eq}}}\right) \\ &> \epsilon + \epsilon q \left(\frac{c_{\text{ch}}^{\text{II}}}{c_{\text{eq}}}\right)^{-(\beta+1)} \left(1 - \frac{1}{q} \frac{c_{\text{ch}}^{\text{II}}}{c_{\text{eq}}}\right) \end{aligned}$$

is required from Eq.(41). The RHS of this inequity is a monotonically decreasing function of $c_{\text{ch}}^{\text{II}}$ that takes a value of ϵq at $c_{\text{ch}}^{\text{II}}/c_{\text{eq}} = 1$, while the left-hand side (LHS) takes unity at the same $c_{\text{ch}}^{\text{II}}$. This indicates that the intersection between the functions of the LHS and RHS is present at $c_{\text{ch}}^{\text{II}}/c_{\text{eq}} > 1$. Denoting c' as the coordinate of the intersection, the above inequity is rewritten as

$$\frac{c_{\text{ch}}^{\text{II}}}{c_{\text{eq}}} > \frac{c'}{c_{\text{eq}}} > 1.$$

Thus, $c_{\text{ch}}^{\text{II}} > c_{\text{eq}}$ is proven for Type II winds in the H-class.

| Expression | Description | Definition |
|-----------------------------------|---|-------------------|
| α | Case B recombination rate coefficient | Eq.(8) |
| α_{eq} | α at the equilibrium temperature ($\approx 2 \times 10^{-13} \text{ cm}^3 \text{ s}^{-1}$) | Eq.(8) |
| β | Power index for the temperature profile of α | Eq.(8) |
| C | Empirical dimensionless factor for base density | Eq.(9) |
| c_s | Typical isothermal sound speed of a wind | |
| c_{eq} | Isothermal sound speed at the equilibrium temperature ($\approx 10 \text{ km s}^{-1}$) | Beginning of §2.1 |
| c_{ch} | Characteristic sound speed | Eq.(15) |
| c_{ch}^{I} | Characteristic sound speed for Type I winds | Eq.(16) |
| $c_{\text{ch}}^{\text{II}}$ | Characteristic sound speed for Type II winds | Eq.(41) |
| c_p | Specific heat at constant pressure | Eq.(1) |
| c_1 | Approximated $c_{\text{ch}}^{\text{II}}$ in the slow-recombination limit | Eq.(51) |
| c_2 | Approximated $c_{\text{ch}}^{\text{II}}$ in the rapid-recombination limit | Eq.(19) |
| Γ_{EUV} | Specific EUV photoheating rate | Eq.(4) and Eq.(5) |
| δ | Ratio of attenuated flux to the unattenuated flux | Eq.(4) |
| $\langle \Delta E \rangle_i$ | Frequency-average deposited energy per photoionization | Eq.(4) |
| \bar{E}_0 | $\langle \Delta E \rangle_i$ at $N_{\text{H}} = 0$ | Eq.(5) |
| ε | Normalized \bar{E}_0 by $mc_p c_{\text{eq}}^2$ | Eq.(18) |
| F_ν | Specific photon number flux | §2.2 |
| F_0 | Unattenuated total photon number flux | §2.2 |
| f_{eq} | Ratio of the secondary critical EUV emission rate to Φ_c | Eq.(49) |
| k_{ioni} | Photoionization rate coefficient | Eq.(7) |
| M_* | Mass of the radiation source | §2.1 |
| m | Gas mass per hydrogen nucleus | Eq.(4) |
| \mathcal{M} | Typical Mach number of a wind | Eq.(50) |
| n_{H} | Hydrogen nuclei number density | §2.2 |
| N_{HI} | H I column density | §2.2 |
| Φ_{EUV} | EUV emission rate of the source | §2.2 |
| Φ_c | Critical EUV emission rate | Eq.(17) |
| Φ_c^{II} | Secondary critical EUV emission rate, $f_{\text{eq}} \Phi_c$ | Eq.(49) |
| $\Phi_{c,\text{rec}}^{\text{II}}$ | Secondary critical EUV emission rate for recombination-dominated Type II winds | Eq.(19) |
| φ | Normalized EUV emission rate, Φ_{EUV}/Φ_c | Eq.(16) |
| φ_{II} | EUV emission rate normalized by $\Phi_{c,\text{rec}}^{\text{II}}$ | Eq.(19) |
| φ_{g} | Boundary of Regions B-II and C at which $c_{\text{ch}}^{\text{II}} = v_{\text{g}}$ | Eq.(48) |
| ψ | Photoevaporation parameter in Bertoldi (1989) | Eq.(27) |
| q | Spectrum hardness parameter for recombination | Eq.(12) |
| r | Spherical radius from the source | §2.2 |
| R | Cylindrical distance from the source | §2.1 |
| R_c | Critical radius | Eq.(1) |
| $\langle \sigma \rangle$ | Frequency-average cross-section | Eq.(4) |
| $\bar{\sigma}_0$ | $\langle \sigma \rangle$ at $N_{\text{H}} = 0$ | Eq.(5) |
| t_{g} | Gravitational timescale | Eq.(3) |
| t_{ioni} | Photoionization timescale | Eq.(7) |
| t_{rec} | Recombination timescale | Eq.(10) |
| v_{g} | Gravitational velocity | Eq.(2) |
| x | Normalized distance, R/R_c | §2.1 |
| χ_e | Attenuation factor due to absorption for photoheating | Eq.(5) |
| χ_i | Attenuation factor due to absorption for photoionization | Eq.(7) |
| y_{HI} | Atomic hydrogen abundance | Eq.(4) |

Table 7. Symbols for the fundamental variables used in our phenomenological model (Sections 2–4). We omit those that appear in later sections.